UNIVERSITAT DE BARCELONA

Electrohydrodynamic jet printing: stability and reproducibility

Alberto Ramón Ferrer

Aquesta tesi doctoral està subjecta a la llicència ***Reconeixement- NoComercial – SenseObraDerivada 4.0. Espanya de Creative Commons.***

Esta tesis doctoral está sujeta a la licencia ***Reconocimiento - NoComercial – SinObraDerivada 4.0. España de Creative Commons.***

This doctoral thesis is licensed under the ***Creative Commons Attribution-NonCommercial-NoDerivs 4.0. Spain License.***

Doctoral thesis

Electrohydrodynamic jet printing: stability and reproducibility

Author:

Alberto Ramón Ferrer

Directors:

Andreu Cabot Codina and Joan Rosell Llompart

UNIVERSITAT DE BARCELONA

Electrohydrodynamic jet printing: stability and reproducibility

Memoria presentada para optar al grado de doctor por la
Universidad de Barcelona

Programa de doctorado en Nanociencias

Autor:
Alberto Ramón Ferrer

Directores:
Dr. Andreu Cabot Codina y Dr. Joan Rosell Llompart

Tutor:
Dr. Arnald Grabulosa Rodríguez

UNIVERSITAT DE
BARCELONA

Contents

Chapter 1. Introduction and scope of the thesis 1

- 1.1. Additive manufacturing 2
- 1.2. Electrohydrodynamic jet printing 4
- 1.3. Full control of patterning with ultrafast nanofibers 11
- 1.4. Control of the jet speed 12
- 1.5. Printing in steady state 19
- 1.6. EHD jet printing using molten polymers 21
- 1.7. Objectives of the thesis 26

Chapter 2. Materials and methods 29

- 2.1. Materials and inks preparation 30
- 2.2. Printer setup and printing protocol used for solvent-based inks 31
- 2.3. Printer setup and printing protocol used for molten polymers 35
- 2.4. Drop size and volume computation 37
- 2.5. Jet speed and flow rate determinations 37
- 2.6. Fiber characterization 38
- 2.7. Electrical current measurement 39

Chapter 3. Patterning with aligned electrospun nanofibers 41

- 3.1. Fiber tracks with controlled width and fiber orientation 42
- 3.2. Effect of solvent evaporation on the morphology of the depositing fiber 45
- 3.3. Fiber patterns 46
- 3.4. Towards applications: accurate fiber patterning with anisotropic properties 51

Chapter 4. Matching the jet speed with the printing speed 55

- 4.1. Determining the jet speed from 2D patterns 56

4.2. Jet deflection strategy based on 3D structures 60
4.3. Influence of the jet deflection parameters on the printing speed 61
4.4. Case study: Jet speed determination in the presence of jet instabilities 64
4.5. Practical application 66
4.6. Implementation of an in situ inspection system 69
Chapter 5. Parametric study on the jet speed and fiber diameter 73
5.1. Effect of the jet dynamics on the printing quality 74
5.2. Ink properties 76
5.3. Processing parameters 79
5.4. Setup design 80
5.5. Ambient conditions 81
5.6. Energy balance for viscoelastic EHD jets 82
Chapter 6. Stability and reproducibility of EHD jet printing 87
6.1. Parameters that affect the jet dynamics 88
6.2. Influence of the polymer molecular weight on the jet stability 89
6.3. Stability of the drop size 92
6.4. Irregular jet ejection regime 95
6.5. Unstable default jet trajectory 97
Chapter 7. Translation of jet deflection to melt electrowriting 103
7.1. Producing thin and fast jets 104
7.2. Jet deflection in melt electrowriting 106
7.3. Jet deflection paired with complex stage movements 110
General conclusions 113
References 119
Future work and outlook 131

List of figures

Figure 1.1. Regimes on EHD jet printing as influenced by the ink viscosity 5

Figure 1.2. Schematics of electrostatic jet deflection with just two electrodes 6

Figure 1.3. Fundamentals of electrostatic jet deflection printing 8

Figure 1.4. LabVIEW interface for EHD jet deflection 10

Figure 1.5. Fiber patterning using electrostatic jet deflection 12

Figure 1.6. Effect of the jet speed on the printed pattern 13

Figure 1.7. Analysis of the drop size effect on the electrical field 20

Figure 1.8. Heterogeneous fiber tracks resulting from different jet instabilities 21

Figure 1.9. Conventional MEW vs jet deflection printing of molten polymers 23

Figure 2.1. Schematics of the EHD jet deflection printing and complete travel of the jet 33

Figure 2.2. EHD jet-deflection printing setup using solvent-based inks 34

Figure 2.3. EHD jet deflection printer setup using molten polymers 36

Figure 3.1. EHD printing of submicrometer fibers into tracks while translating the substrate 43

Figure 3.2. Fiber track width and density 44

Figure 3.3. Effect of the substrate translation speed on the fiber density 45

Figure 3.4. Dependence of the fiber patterning on the mechanical properties of the jet 46

Figure 3.5. Controlling the track width and fiber density by changing the deflection angle 47

Figure 3.6. Fiber tracks printed by deflecting the jet to follow various motifs 48

Figure 3.7. Modifying the jet deflection parameters along the track 50

Figure 3.8. Toward applications 52

Figure 4.1. Determining fiber speed on conventional and jet-deflection printing 59

Figure 4.2. Jet speed determination from the size of printed structures 61

Figure 4.3. Effect of the jet-deflecting signal amplitude on the printing of 2D patterns 62

Figure 4.4. Effect of the jet-deflecting signal frequency on the printing of 2D patterns............. 64
Figure 4.5. Detection of the jet speed instabilities.. 65
Figure 4.6. Interdigitated electrodes printed by mechanical stages paired with jet deflection..... 67
Figure 4.7. In-situ monitoring of the jet speed via the width of a printed fiber track.................. 70
Figure 5.1. Effect of the jet speed on the quality of the printed patterns.................................... 74
Figure 5.2. Effect of ink properties on the jet speed and the fiber diameter................................ 76
Figure 5.3. Effect of the PEO concentration on the ink’s zero-shear viscosity........................... 78
Figure 5.4. Effect of processing parameters on the jet speed and the fiber diameter.................. 79
Figure 5.5. Effect of the printer setup on the jet speed and the fiber diameter............................ 80
Figure 5.6. Effect of the ambient conditions on the jet speed and the fiber diameter 81
Figure 5.7. Electric energy invested in ejecting thin and fast jets 84
Figure 6.1. Principle of the EHD jet printing process with jet deflection 88
Figure 6.2. Influence of the PEO MW on the printed pattern... 90
Figure 6.3. Influence of the polymer MW on the jet speed stability 91
Figure 6.4. Evolution of the drop and jet parameters over time 93
Figure 6.5. Effect of the nozzle voltage on the jet-ejection mode 96
Figure 6.6. Influence of nozzle voltage and infusion pump rate on the jet ejection point........... 97
Figure 6.7. Analysis of the default jet trajectory 99
Figure 6.8. Effect of the jet deviation on the printing process... 100
Figure 7.1. From conventional MEW printing to upgraded MEW printing............................. 105
Figure 7.2. Micron-scale fibers printed using molten polymers... 105
Figure 7.3. Proof of concept for deflecting the MEW jet 106
Figure 7.4. Excellent stability of the jet deflection in MEW 107
Figure 7.5. Rare interruptions of the jet.. 108
Figure 7.6. Anisotropic properties of the nanofibers result in optical effects............................ 109
Figure 7.7. Complex patterning of fibers by jet deflection... 111

List of tables

Table 1.1. Classification of Additive manufacturing approaches. 3

Table 5.1. Operational parameters that affect the jet speed 75

Table 5.2. Composition and properties of the inks used in this work 77

Table 6.1. Ink compositions and their properties 89

List of acronyms

1D	One-dimensional
2D	Two-dimensional
3D	Three-dimensional
AM	Additive manufacturing
Ag	Silver
CAD	Computer-aided design
CMOS	Complementary metal oxide semiconductor
DAQ	Data acquisition
DEW	Droplet, interfaces and flows
DMF	Dimethylformamide
EG	Ethylene glycol
EHD	Electrohydrodynamic
EtOH	Ethanol
H	Nozzle to collector distance
H_2O	Water
HV	High voltage

ID	Inner diameter
IREC	Institut de recerca en energia de Catalunya
LED	Light emitting diode
MEW	Melt electrowriting
MW	Molecular weight
NaCl	Sodium chloride
NP	Nanoparticle
OD	Outer diameter
PCL	Poly(ε-caprolactone)
PEO	Polyethylene oxide
PVP	Polyvinylpyrrolidone
RH	Relative humidity
SE2	Secondary electrons
SEM	Scanning electron microscope
STL	Stereolithography (format)
URV	Universitat Rovira i Virgili

Acknowledgements

People who are not familiar with the process of attaining a PhD may think that it involves isolating yourself in a lab during many years and carrying out experiments repeatedly until you get some results. However, this is not the case. After spending the last four years of my life at IREC, I can confirm that it has been a massive learning experience for me, and I could not have gotten where I am nowadays without the support of a large number of people, to whom I am extremely grateful.

First and foremost, I would like to express my deepest appreciation to my thesis supervisors Andreu Cabot, who has accepted me into his lab and supplied me equipment to carry out my studies, and Joan Rosell, for sharing his invaluable insight about electrohydrodynamic phenomena. They allowed me to pursue my work in an independent yet guided manner, influencing me to grow as a scientist and providing me an incredible support to go further in my research. Additionally, they assisted me with their constructive advices and instructions on analyzing my results with critical eye. Even when I became frustrated at the process of publishing my results, their never-ending assistance helped me to overcome this and grow both personally and professionally.

I would like to extend my sincere thanks to Ievgenii Liashenko, my main colleague here at IREC, for his vast amount of intellectual contributions not only in the field of additive manufacturing technologies and electrohydrodynamic phenomena, but also for his knowledge about how real life works. He always nurtured, guided and motivated me over the last four years, and he has become one of my dearest friends. This thesis would be poorer without him.

Many thanks also need to be extended to my other colleagues from IREC, who have provided me with valuable insight and suggestions throughout my PhD: Peter, Anthea, Xiang, Chaoqi, Pablo, Guillem, Jesus, Maria, Ke Xiao, Ruifeng, Gavin, Linlin, Lu, Canhuang, Mengyao, Karol, Paulina, Lili, Xingqi… I must confess that the entire list of people who has coincided with me during these four years at IREC is endless, sorry if I forgot to mention someone. I also had the great pleasure of working with Antonio, Elena, Reyda, Eszter, Deepak, Laura and Prof. Jordi Grifoll, from DEW group at Universitat Rovira i Virgili. They built an excellent research group and an amazing environment in their lab, allowing the easy discussion of the results we got during these years of PhD. Thanks to all of your suggestions, which permitted me to perform my studies.

I am going to continue with my appreciation to Prof. Paul Dalton, from University of Oregon, who has accepted me into his research group for doing my international research stay and has given me the opportunity to implement electrostatic jet deflection in MEW. Thanks to him and the people who work with him, I learned how to print using molten polymers and how to assemble 3D printers. These 5 months were very exciting, and I could work again with Ievgenii and other people immensely qualified, as Simon, Biranche, Ander, Paula, Kelly, Taavet, Amanda, Andrew, Sonke, Patrick, Naomi, Sofia and Srikar. All of them helped me while I was struggling with the building of my Voron, and gave me their point of view of my results when I was carrying out my first experiments to get thin and fast fibers. Simon, sorry for bothering you so many times asking infinite questions. I promise you that I have learned a lot with your explanations. Kseniia, thank you for supplying unlimited number of cakes every week. All of them were very tasty.

I appreciate very much my family and friends, who have been a source of great joy and support for me over the past few years. Particularly helpful to me during this time has been Andrea, who listened to me almost every day complaining about how hard was doing a PhD, or how frustrated I was after doing experiments wrongly. She provided me encouragement and perseverance throughout the duration of this thesis. Her patience cannot be underestimated. Thanks also to Vueling and Ryanair for the cheap flights that I used every month to see my family and Andrea.

I also must thank the people from FQPIMA group, at Complutense University of Madrid, with whom I started my research journey seven years ago. Specifically, I would like to thank Miguel, who taught me how to execute experiments while I was embarking on my master thesis, and showed me how to organize my daily work routine. I also must thank the useful recommendations that Isa, Mateo, Alberto, Susana, Cris, Pablo, Victor… gave me about how to perform my experiments. They instructed me for being a good scientist and suggested me many advices that I always considered, except the ones about "please, do not do a PhD". I am eternally grateful to have met them in Madrid.

Finally, I thank all funding sources that made all this possible. Principally, this thesis was supported by BES-2017-081681 grant, from Spanish Ministry of Economy, Industry and Competitiveness, but other funding sources came from SEHTOP ENE2016-77798-C4-3-R, 2018-LLAV-00044, COMBENERGY PID2019-105490RB-C32, 2019 INNOV 00054, 2017SGR1516, PGC2018-099687-B-I00 and PID2021-129064NB-I00.

…to my beloved parents…

Summary

Additive manufacturing (AM), also known as three-dimensional (3D) printing, is a layer-by-layer technique that allows producing 3D objects directly from a digital model. It enables the fabrication of innovative products such as personalized implants, lightweight and cost-saving components for the aviation and automotive industry, integration of electronics and sensors and so on.

Among the different AM approaches, we based our technology on (1) using solvent-based inks, which provides a true material versatility and makes possible the fabrication of structures with virtually any material and composition; (2) electrohydrodynamic (EHD) phenomenon, which permits the ejection, from an ink drop, of fast and thin polymeric fibers, also known as jets; and (3) electrostatic deflection of the jet during the printing, which enables the control of the positioning of the added material during its travel from the drop towards the collector. This printing approach not only allows the precise deposition of the polymeric nanofiber and defines accurately the patterning of fibers in the printing area, but also it gives the ability to print 3D structures by stacking different layers, one on top of each other, following the pattern geometry.

The quality of the printed structures strongly depends on matching jet speed with the printing speed (which is determined by the jet deflection speed), and this approach not only allows easily defining the printing speed by modifying the jet deflection signal, but also it permits computing the jet speed by analyzing the printed structure dimensions.

Additionally, a parametric study has been carried out to understand how operational parameters affect the jet dynamics, and how they can be tuned according to our needs. Ink properties, processing parameters, setup design and ambient conditions are analyzed to understand their effect on the jet speed and on the diameter of the printed fibers.

However, as this technique uses solvent-based inks, the evaporation of the solvent from the drop has a huge impact on the reproducibility and stability of the printing. As the solvent evaporates, the drop properties change, and thus the speed at which the jet is ejected from the drop is also altered, preventing the printing of homogeneous patterns. For this reason, this thesis also deals with different methods to improve the stability and reproducibility of the printing process over time, analyzing the effect of the drop size and the dryness of its surface on the deposited patterns.

Finally, this thesis shows the implementation of the electrostatic jet deflection in melt electrowriting (MEW) technology, which is a different printing approach that uses molten polymers instead of solvent-based inks. As MEW ejects much thicker and slower jets than the ones produced by using solvent-based inks, the experimental conditions were optimized to get thin and fast jets before the implementation of the electrostatic jet deflection. This regime allowed deflecting the jet by controlling the electrical field on its surrounding to accurately position submicron fibers on the collector.

Resumen de los resultados

Los sistemas de fabricación aditiva, también conocidos como sistemas de impresión 3D, son un conjunto de técnicas que construyen estructuras añadiendo capa a capa el material a utilizar, permitiendo elaborar objetos 3D a partir de un modelo digital.

Entre los diferentes métodos de fabricación aditiva, nosotros hemos establecido nuestra tecnología de impresión 3D a partir de los siguientes enfoques: utilizar tintas en donde el polímero se disuelve en un solvente; basarse en los fenómenos electrohidrodinámicos, que permiten la eyección de fibras poliméricas (jets) rápidas y delgadas; implementar la desviación electrostática del jet, que permite controlar el sitio exacto en donde se depositará la fibra sobre el colector mediante la modificación del campo eléctrico.

La calidad con la que se imprimen las estructuras depende básicamente de igualar la velocidad del jet con la velocidad de impresión, que en nuestro caso está definida por la velocidad en que se desvía el jet. Nuestra tecnología de fabricación aditiva no solo permite determinar fácilmente la velocidad de impresión a través de definir la señal de desviación del jet, sino también permite conocer la velocidad del jet a partir de medir sus dimensiones.

Adicionalmente, se ha realizado un estudio paramétrico para entender cómo los parámetros operacionales afectan a la dinámica del jet, y cómo se puede variar la velocidad del jet según nuestros intereses. Sin embargo, esta técnica utiliza tintas en donde el polímero se disuelve en un solvente, por lo que la evaporación de dicho solvente tendrá un impacto importante en la estabilidad y la reproducibilidad de la impresión. Cuando el solvente se evapora, las propiedades de la gota cambian, y por lo tanto la velocidad en que el jet es propulsado desde la gota también cambiará, impidiendo la impresión de objetos homogéneos como consecuencia. Por este motivo, en esta tesis se analizan varios métodos para mejorar la estabilidad y reproducibilidad de la impresión durante el tiempo, examinando el efecto del tamaño de la gota y del secado de su superficie en los objetos impresos.

Finalmente, en esta tesis se muestran los primeros resultados obtenidos al implementar la tecnología de desviación del jet utilizando polímeros fundidos en vez de disueltos en un solvente.

List of publications

1. Liashenko, I., **Ramon, A.**, Cabot, A. & Rosell-Llompart, J. Ultrafast electrohydrodynamic 3D printing with in situ jet speed monitoring. Mater. Des. 206, 109791 (2021). https://doi.org/10.1016/j.matdes.2021.109791. Impact factor: 8.0

2. Liashenko, I.*, **Ramon, A.***, Rosell-Llompart, J. and Cabot, A. (2022), Patterning with Aligned Electrospun Nanofibers by Electrostatic Deflection of Fast Jets. Adv. Eng. Mater. 2101804. https://doi.org/10.1002/adem.202101804. Impact factor 4.122
   * Equal contribution

3. **Ramon, A.**, Liashenko, I., Cabot, A. and Rosell-Llompart, J. Tuning jet speed and fiber diameter in near-field electrospinning.
   To be submitted

4. **Ramon, A.**, Liashenko, I., Rosell-Llompart, J. and Cabot, A. On the Stability and Reproducibility of Electrohydrodynamic Jet Printing using Solvent-Based Inks.
   To be submitted

List of conferences

1. **Authors:** Alberto Ramón, Ievgenii Liashenko, Andreu Cabot, Joan Rosell Llompart.

   Work title: EHD for 3D printing: Reproducibility on the electrostatic jet deflection in near-field electrospinning.

   Contribution type: Poster presentation.

   Conference name: European Workshop on Electrohydrodynamic Atomization 2020.

   Organizing entity: Universitat Rovira I Virgili.

   Place and date of the event: Tarragona (Spain), February 12 – 14, 2020.
2. **Authors:** Alberto Ramón, Ievgenii Liashenko, Joan Rosell Llompart, Andreu Cabot.

   Work title: Rapid EHD 3D printing of scaffolds with submicrometer size features.

   Contribution type: Oral presentation.

   Conference name: V Congreso de Jóvenes Investigadores en Coloides e Interfases.

   Organizing entity: Real Sociedad Española de Química.

   Place and date of the event: Zaragoza (Spain), March 2 – 4, 2020.
3. **Authors:** Alberto Ramón, Ievgenii Liashenko, Joan Rosell Llompart, Andreu Cabot.

   Work title: Study of the jet dynamics for electrohydrodynamic 3D printing using electrostatic jet deflection.

   Contribution type: Oral presentation.

   Conference name: European Workshop on Electrohydrodynamic Atomization and Electrospinning.

   Organizing entity: University of Naples.

   Place and date of the event: Online format, June 9 – 10, 2021.
4. **Authors:** Alberto Ramón, Ievgenii Liashenko, Joan Rosell Llompart, Andreu Cabot.

   Work title: A novel method for 3D printing at submicron scale and fast speed using electrostatic jet deflection.

   Contribution type: Oral presentation.

   Conference name: International Conferences & Exhibition on Nanotechnologies, Organic Electronics & Nanomedicine.

   Organizing entity: University of Thessaloniki.

   Place and date of the event: Thessaloniki (Greece), July 3 – 10, 2021.

Chapter 1

Introduction and scope of the thesis

1.1. Additive manufacturing

Nanotechnology has gained huge attention in both industrial production and research field owing to its novel properties and unpredictable potential on chemical, physical and biological systems at scales ranging from a single atom to sub-millimeter dimensions[1]. Previous nanotechnology research has achieved breakthroughs in a myriad of fields, including catalysis[2], energy conversion, energy storage[3–5], soft robotics[6] and tissue engineering[7].

Techniques for fabricating patterns on surfaces at micrometer and nanometer length scales are critically important to many existing and emerging technologies[8], as they provide structures and devices with improved performances. For this reason, a wide variety of industries and research centers offer huge incentives to improve the existing fabrication processes and develop new ones.

Additive manufacturing (AM), commonly known as 3D printing, has emerged as a disruptive technology that is capable of fabricating products with complex geometries through accumulating materials in a layer-by-layer manner[9–11]. Initially, to print the desired part, the geometry of the structure must be either designed using a computer-aided design (CAD) or scanned using an existing part that would be replicated[9,12]. Then, the CAD model is typically converted into stereo-lithography (STL) format, where the shape is transformed and stored as triangulated surface. After that, depending on the AM technique and printing parameters, such STL model is “sliced”, thus generating printing trajectories for each layer. Finally, the 3D object is built by stacking several layers one on top of each other.

Since its emergence 35 years ago, AM has found applications in many industries[9,11,13]. One reason for the success of AM is its ability to print almost any desired geometry. It enables not only positioning the material of interest directly on substrates, but also printing by means of different methodologies that involve repetitive depositions, patterning and removal of materials to build complex shapes[8,14]. Over time, AM industry has transformed significantly from its early days due to the need for getting more intricate and miniature designs. The available technologies allowed improving the efficiency and quality of the manufacturing processes and enabled emerging different AM approaches, which can be classified in several ways depending on their operating principles and materials used. For example, one possibility is to distinguish AM methods between *light*-based, *nozzle*-based and *particle*-based[11,12].

Another classification is possible regarding the material form used, which can be classified as *resin*-based, *powder*-based and *droplet*-based systems[9,11]. Therefore, some printing approach may be classified in more than one category, depending on the statements chosen to classify them. However, following the report from the ISO/ASTM52900:2015, additive manufacturing techniques can be classified in seven families[10,12], as Table 1.1 describes:

Table 1.1. Classification of Additive manufacturing approaches.

AM family	Operating principle	Material used	Technologies
Vat Photopolymerization	Photopolymeric liquids are deposited in a vat and are selectively cured via light-activated polymerization, using lasers or projectors, which converts the exposed areas to solid materials.	Photopolymers	SLA™ - Stereolithography apparatus; DLP™ - Digital Light Processing; 3SP™ - Scan, Spin, and Selectively Photocure.
Material Jetting	Droplets or continuous fibers of the printing material build layer-by-layer the 3D object	Polymers, waxes, composites	Polyjet™; SCP™ - Smooth Curvatures Printing.
Binder Jetting	A liquid bonding agent is carefully deposited to join powder materials and build layer-by-layer objects.	Polymers, metals, foundry sand	3DP™ - 3D Printing; ExOne; Voxeljet.
Material Extrusion	Materials are carefully dispensed through a nozzle or orifice in tracks or beads, which are combined then into multi-layer models.	Polymers	FFF - Fused Filament Fabrication; FDM™ - Fused Deposition Modeling.
Powder Bed Fusion	A powder bed region is selectively fused using thermal energy to build the structure. The powder around the merged parts acts as support material for overhanging features.	Polymers, metals, ceramics	SLS™ - Selective Laser Sintering; EBD™ - Electron Beam Melting; MJF™ - Multi-jet Fusion.
Sheet Lamination	Sheets of material are bonded chemically (for polymers and papers) or via ultrasonic welding (for metals) to form an object.	Polymers, paper, metals	SDL - Selective Deposition Lamination; UAM - Ultrasonic Additive Manufacturing.
Directed Energy Deposition	Focused thermal energy (provided by lasers, electron beam…) is used to fuse materials by melting as they are being deposited.	Metals	LENS™ - Laser Engineering Net Shaping; DMD™ - Direct Metal Deposition.

Each of the processes has associated strengths and weaknesses related to the following characteristics[11]:

- The materials they can use (typically different polymers or metals, but also waxes and paper). It is important to note that the list of materials that each AM approach can use is currently growing.
- The speed at which they can build structures (*i.e.*, the printing speed).
- The dimensional accuracy and quality of the surface finish of the produced structures.
- The material properties of the produced structures.
- Machine and material costs.

1.2. Electrohydrodynamic jet printing

AM techniques comprise different procedures to build 3D structures of a wide range of sizes. In our case, as we are motivated by the unpredictable benefits that nanotechnology provides to innumerable fields of application in our society, we are interested in printing at submicrometer scale, so we based our printing technology on existing approaches that allow printing at such small sizes. However, the current printing methods do not satisfy all the requirements needed for being considered as a competitive technology, which are (1) being endowed with high material versatility; (2) being a low-cost technology; (3) being able to print at submicron resolution; and (4) being capable to print at high speed. For this reason, we use a 3D printing technology based on the following approaches to ensure previous specifications:

- **Solvent-based inks**

We use solvent-based inks to allow the manufacture of items made of virtually any substance, ranging from polymers[15–17] to metals[14,18–20], ceramics[21–23], wood[24–26], biological tissues[27–30], etc. Besides the low cost and simplicity, the main advantage of the technologies that use solvent-based inks is that they enable the use of inks formulated to contain any component in the form of ions, molecules, nanoparticles (NPs) or living cells.

- **Electrohydrodynamic phenomena**

Electrohydrodynamic (EHD) phenomena enable submicron printing resolution by using electrostatic forces to pull a very thin filament of ink, commonly known as jet[8,31]. The basic operation of these technologies involves creating an electric field between a conductive nozzle and a grounded collector to generate electrostatic forces on the ink surface. With the gradual increase of the electric field strength, the charges on the drop surface repeal each other, thus deforming the meniscus and ejecting a thin jet when the electrical stresses overcome the drop surface tension[1,31].

The properties of the ink determine which regime is going to prevail during the EHD jetting, as Figure 1.1 shows. When using low-viscosity inks, the EHD jet experiences periodic varicose instabilities that will cause its breaking into droplets. Those droplets repel each other due to their electrical charges, and consequently their trajectory deviates and a large track of droplets covers the collector (Figure 1.1a). Increasing the viscosity of the ink allows inhibiting the varicose instabilities that cause the jet breakup, depositing beaded or smooth fibers when intermediate or high viscous inks are used (Figure 1.1b and 1.1c, respectively). To ensure printing with continuous fibers, the ink should be viscoelastic enough to prevent the breaking of the jet intro droplets, and the airborne jet should dry fast enough during its flight from the drop towards the collector, as big droplets or beaded fibers may form if the jet reaches the printing area and it is still wet.

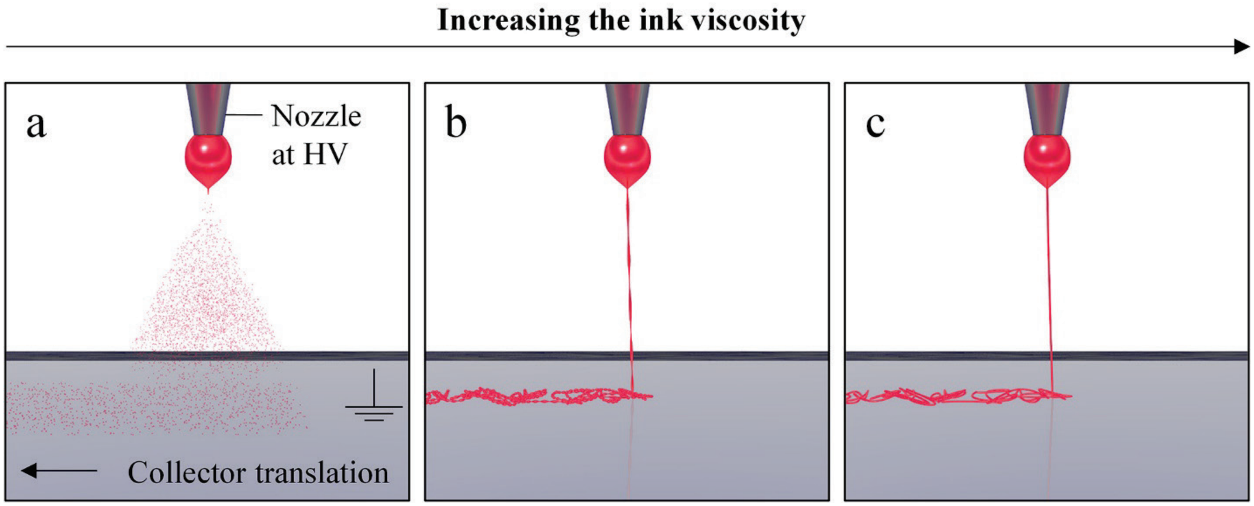

Figure 1.1. Regimes on EHD jet printing as influenced by the ink viscosity. Ink viscosity determines the stability of the jet during its travel toward the printing area. Low viscosity inks lead to the breaking of the jet, which results in the deposition of droplets on the collector (a), while intermediate and high viscous inks entail printing beaded (b) and smooth fibers (c) on the collector.

- **Electrostatic jet deflection**

Conventional EHD jet printing relies on moving the stage to follow a path that reproduces the pattern geometry while a very thin and fast jet is deposited on the collector. Such jets can reach speeds above 1 $m \cdot s^{-1}$ but cannot be precisely collected by too slow mechanical stages[12], so the fiber typically buckles when it reaches the collector, and the quality of the printed pattern is compromised. For this reason, electrostatic jet deflection was recently developed by URV and IREC to print with submicron fibers at fast speed[32,33]. The electrostatic jet deflection technique consists in placing two or more auxiliary electrodes around the nozzle that modify the electric field in the vicinity of the jet to deflect it from its default trajectory and control its arrival point at the collector (Figure 1.2)[34]. The electric field is modified by producing and amplifying computer-generated signals and applying them to the jet-deflecting electrodes. In addition, synchronizing those signals allows adjusting the jet trajectory and controlling its deposition to print two-dimensional (2D) and 3D patterns. Using this approach, the stage is only used either to move the collector between structures printed at sub-millimeter scale or to move the collector continuously to print patterns at millimeter scale while the jet is deflected continuously.

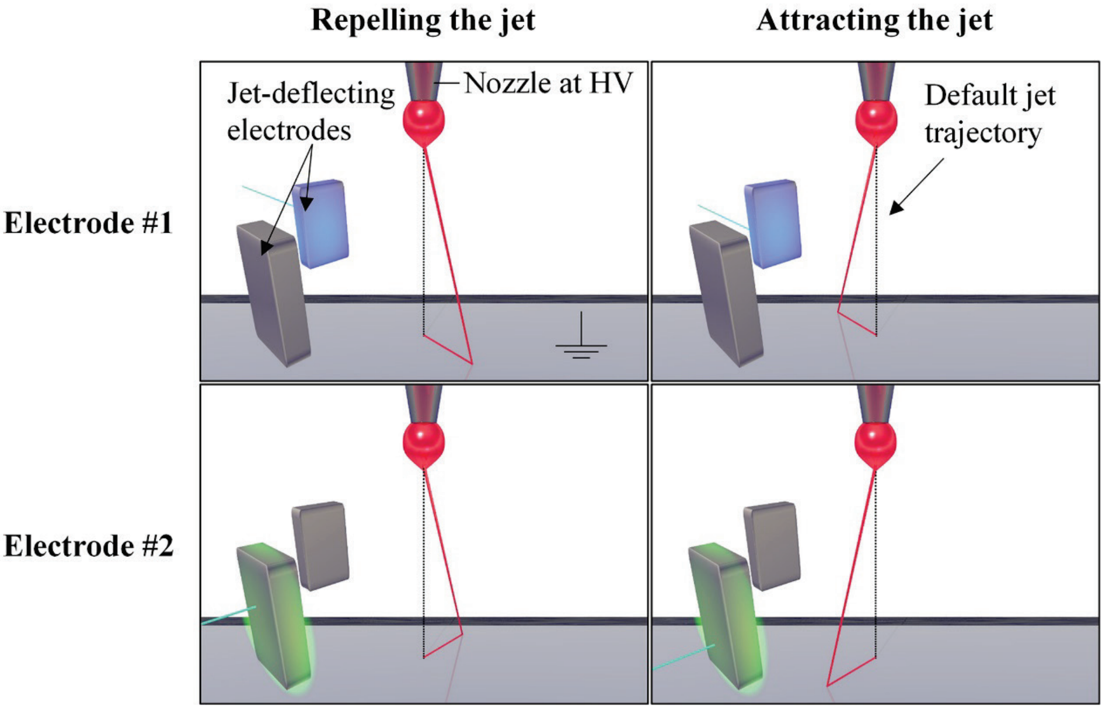

Figure 1.2. Schematics of electrostatic jet deflection with just two electrodes. The two auxiliary electrodes modify the electric field around the jet to control its deposition on the collector.

The experimental setup that characterizes this novel EHD jet printing approach is composed of different devices that enable us to control the printing variables and monitor the jet. First, a syringe pump is required to supply the ink to the nozzle. Then, an XY stage is indispensable to either move the collector continuously and deposit tracks of fibers, or move the collector making short stops to build 3D structures. In our printing setup, the nozzle is connected to high voltage (HV) and the collector is connected to ground to create the electrical field that allows ejecting EHD jets. Thus, a power supply is also necessary to apply HV on the nozzle. Additionally, a data acquisition card (DAQ card, which generates the jet-deflecting signal) and amplifiers (with enough power and speed to control the deposition of the airborne jet) are also needed in this printing approach. All of these devices can be operated using a computer with its corresponding software. Finally, an optical camera with proper magnifying lenses is essential to supervise the ejection of the jet from the drop.

One of the greatest challenges of material jetting technologies is to deposit materials controllably as very small 2D and 3D structures at high speed, and electrostatic jet deflection enables the accurate printing of fast EHD jets with submicrometer resolution. In this printing methodology, obtaining pattern fidelity relies on matching the printing speed (given by the amplitude and frequency of the deflection signal that reproduces a specified path) with the jet arrival speed (attained by the jet right before it reaches the collector). If the intended printing speed is larger than the jet speed, the jet will not be able to reproduce accurately the pattern geometry due to it will cut the corners, since it cannot follow the printing speed. If the intended printing speed is lower than the jet speed, then undesired fiber accumulation or buckling takes place.

A LabVIEW software was specifically developed to define the deflection signals that describe the pattern geometry. This software allows us to set the printing speed by specifying the amplitude and frequency of the deflection signal[12,34]: the amplitude defines the size at which the pattern is going to be printed, while the frequency defines how many layers of the pattern geometry are going to be printed per second (Figure 1.3). Additionally, this software enables us to estimate the jet speed by analyzing the printed pattern obtained when the collector moves, as the width of a printed track can readily be converted to the jet speed from the knowledge of the printed pattern geometry and the frequency of the jet deflection signal. This determination does not require a fast stage, as even slow stage movements are enough because the fast fiber is swiftly positioned by the jet deflection. If the jet speed is faster or slower than the printing speed, the working conditions can be modified until both speeds match, thus attaining the best printing quality.

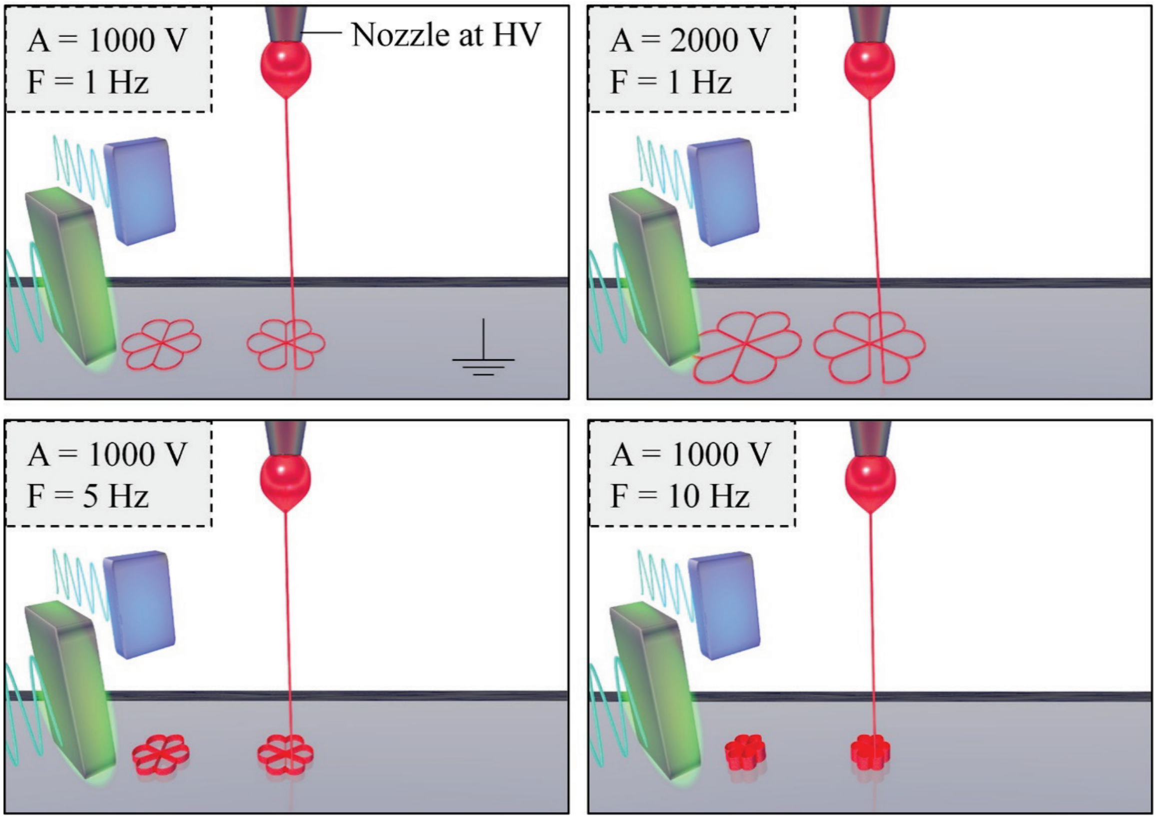

Figure 1.3. Fundamentals of electrostatic jet deflection printing. The amplitude and frequency control the size of the printed pattern and how many layers are going to be printed each second. The resulting printing speed is a product of the deflection signal amplitude and frequency and the pattern geometry.

The strategy that allows simple conversion between a preset pattern geometry and jet-deflection parameters into jet-deflection signals is detailed below[12]. First, a pattern geometry (or motif) is described as a multitude of points with coordinates in the XY plane, where the first and last points have the same coordinates. In terms of jet-deflection signals, one motif describes one period of jet-deflection signals both in the X and in the Y directions, and the period duration is the inverse of the frequency of the signal, which is controlled independently from the motif geometry. Later, the frequency and amplitude of the jet-deflection signals are defined to create a digital signal for X and Y. Then, those digital signals are computed by the software and are applied to an input to the DAQ card (which is the signal generator). Synchronized digital signals encode the pattern geometry and other parameters (signal amplitude, frequency…) and are represented as X and Y waveforms (defined as a series of waypoints, which are specific voltage targets occurring at specific times along the waveform).

Afterwards, the signal generator converts those digital signals into analog signals, which are then amplified and applied to the deflecting electrodes. It must be noted that digital input signals should have a high temporal resolution to generate the analog signal needed for jet deflection along the desired motif. For example, given a printing frequency of 100 Hz, the waveform should have a high enough sampling rate to appropriately represent the desired printing motif within a single period of 0.01 seconds. Such temporal resolution of jet-deflection signal sets the minimum requirements on the signal generator and amplifiers, in terms of the sample rate (samples per second) and the slew rate (volts per second), which is the rate of the voltage change.

On the other hand, the current arrangement of our jet-deflecting electrodes (with just two electrodes) produces an asymmetry in the electrical field, as only two electrodes are positioned orthogonally to each other around the nozzle. Consequently, the geometry of the pattern would be deformed while it is being printed. To correct this deformation, the LabVIEW software integrates a mathematical algorithm that modifies the generated signal, which is then amplified and applied to the deflecting electrodes. This algorithm allows us to preventively eliminate the deformation caused by the asymmetric electrical field. Figure 1.4 illustrates the user interface of the LabVIEW software used to deflect electrostatically the jet.

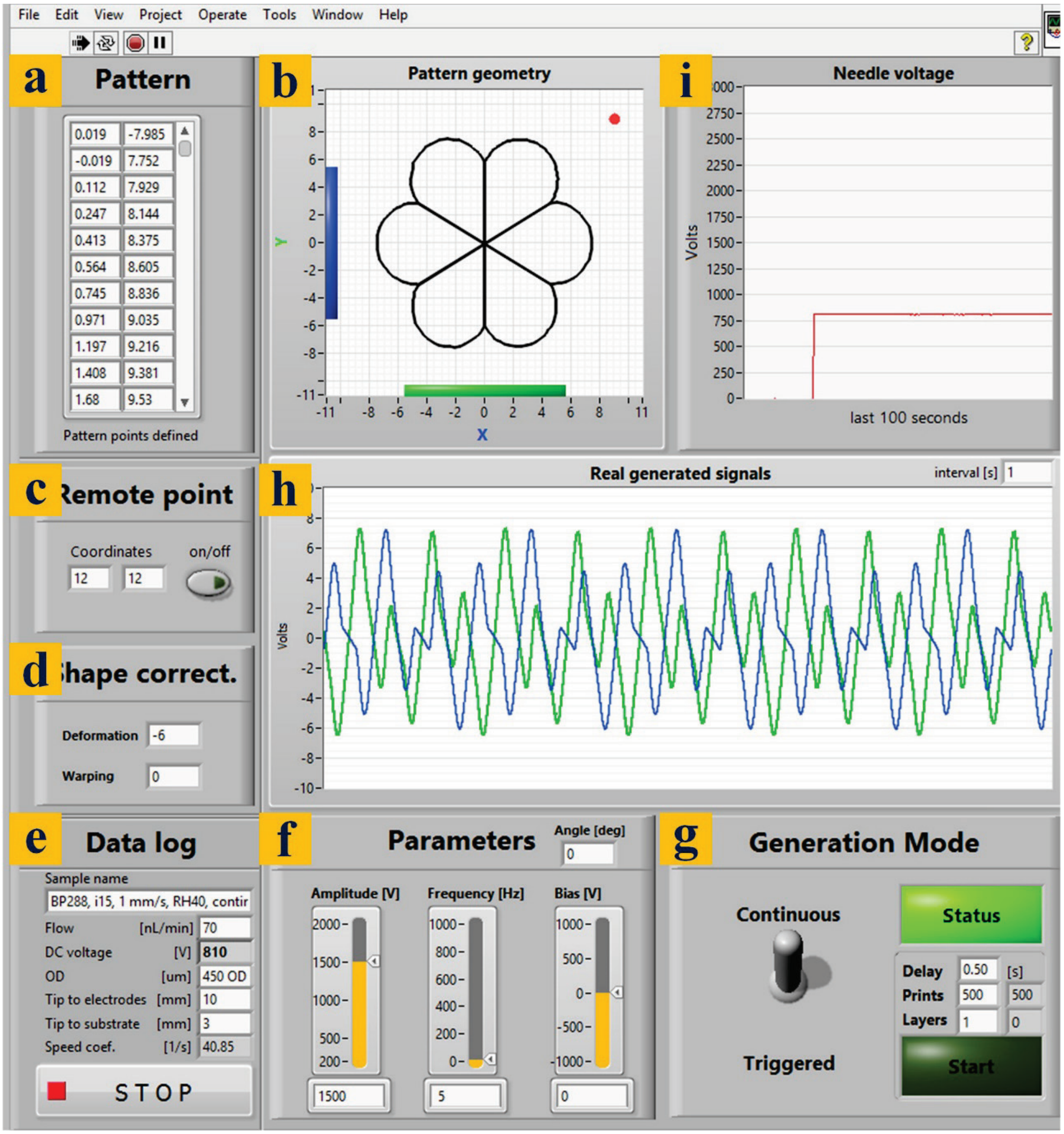
File
Edit
View
Project
Operate
Tools
Window
Help
a
Pattern
b
Pattern geometry
8
6
4
2
0
-2
-4
-6
-8
-11
-11
-8
-6
-4
-2
0
2
4
6
8
11
x
y
i
Needle voltage
Volts
2750
2500
2250
2000
1750
1500
1250
1000
750
500
250
0
last 100 seconds
c
Remote point
d
Shape correct.
h
Real generated signals
Volts
8
6
4
2
0
-2
-4
-6
-8
-10
e
Data log
STOP
f
Parameters
2000
1500
1000
500
200
1000
800
600
400
200
0
1000
500
0
-500
-1000
g
Generation Mode
Continuous
Triggered
Status
Start

0.019	-7.985
-0.019	7.752
0.112	7.929
0.247	8.144
0.413	8.375
0.564	8.605
0.745	8.836
0.971	9.035
1.197	9.216
1.408	9.381
1.68	9.53

Pattern points defined

interval [s] 1

Coordinates 12 12 on/off

Deformation -6

Warping 0

Sample name BP288, i15, 1 mm/s, RH40, contir

Flow	[nL/min]	70
DC voltage	[V]	810
OD	[um]	450 OD
Tip to electrodes	[mm]	10
Tip to substrate	[mm]	3
Speed coef.	[1/s]	40.85

Angle [deg] 0

Amplitude [V] 1500

Frequency [Hz] 5

Bias [V] 0

Delay	0.50	[s]
Prints	500	500
Layers	1	0

Figure 1.4. LabVIEW interface for EHD jet deflection. The pattern geometry is defined in (a) as coordinate points in XY space, and it is plotted in (b) together with the relative orientation of deflection electrodes. In (c) it is possible to define a point in the XY space to keep the jet motionless away from its usual default jet trajectory when the stage moves from one printed object to another. It is only available when the deflecting signal is generated in triggered mode. Shape correction parameters compensating for asymmetric electric field are set in (d). The relevant information of the printing is specified in (e), which is saved in a separate text file for each experiment. The jet speed is defined by setting the amplitude and frequency of the jet-deflecting signal and the voltage bias of the electrodes (f). The printing mode is defined in (g), which can be either continuous or triggered signal generation. The DAQ card generates the analog signals for both electrodes, which are measured and plotted, and continuously updated, in (h). In this graph, different colors refer to different electrodes. Finally, the nozzle voltage is monitored over time in (i).

1.3. Full control of patterning with ultrafast nanofibers

Fabrication of polymeric nanofibers by EHD jet printing has attracted considerable attention from researchers owing to a wide variety of applications in the field of sensors[35,36], energy storage[5,36], smart textiles[37,38], drug delivery[39,40], tissue engineering[41,42] and piezoelectric energy generators[43,44].

Printing with EHD jets requires a complete control of the arriving fiber deposition to print predefined fiber tracks on the collector. Since conventional EHD jet printing cannot guarantee the precise deposition of fibers, as the jet speed is generally much faster than the stage translation speed and, consequently, the jet buckles when it reaches the collector, electrostatic jet deflection printing is presented as a suitable approach to deposit precisely the airborne jet on the collector (Figure 1.5). The jet-deflecting electrodes modify continuously the electrical field around the jet in order to control its positioning and print any desired patterns.

- **Patterning of fibers with controlled alignment**

The deposition of straight fibers with accurate alignment and precise distance between fibers are needed for some specific purposes, such as the production of scaffolds that mimic the mechanical anisotropy of human tissues[45], the regulation of the growing direction of cells on the surface of the scaffold[46], etc. Therefore, the collection of aligned fibers has to be controlled during the printing, and electrostatic jet deflection printing opens the possibility to control the fiber positioning in one-dimensional (1D) plane, depositing straight fibers (Figure 1.5, left image) with controlled length by specifying the proper deflection parameters (*i.e.*, the amplitude and frequency of the deflecting signal).

- **Patterning of complex geometries**

Beyond simple 1D deflection, the patterning of complex fiber tracks with functional nanofibers is used to enhance the properties of some devices, such as sensors[47] or scaffolds[48]. Other purposes may be related to the production of scaffolds with different pore sizes to differentiate the cell growing[49]. In this scenario, complex fiber patterns can be printed directly on the collector after predefining the pattern geometry and controlling the electrical field around the jet via electrostatic jet deflection (Figure 1.5, right image).

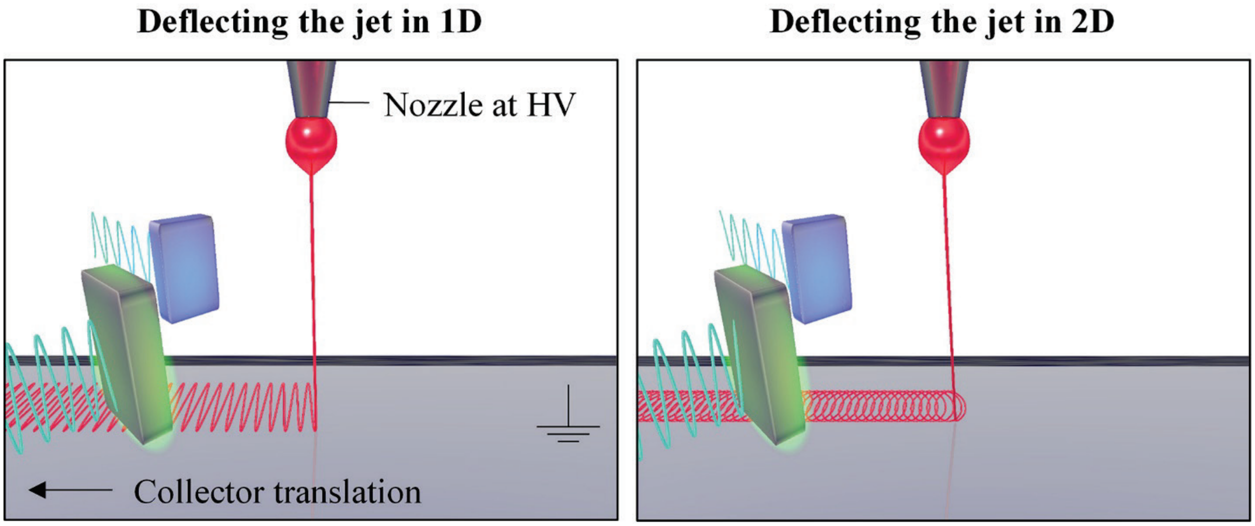

Figure 1.5. Fiber patterning using electrostatic jet deflection. The jet can deposit either aligned fibers or complex geometries via electrostatic deflection in a 1D or 2D plane, respectively.

As the jet-deflecting electrodes control the electrical field around the jet and govern the fiber positioning, the stage is only used to move the collector to print long fiber tracks. Therefore, electrostatic jet deflection printing should be appropriated for a large number of applications that require a precise control on the deposition of submicron fibers at fast speed.

1.4. Control of the jet speed

As it has been said, printing with high fidelity depends critically on controlling the jet arrival speed, which must be matched to the printing speed.

Electrostatic jet deflection allows computing the jet speed from the product of the frequency of the deflection signal and the width of the periodically printed pattern (times a factor that depends on the printed geometry). The simplest way to estimate it consists in deflecting the jet transversely to the stage motion to print a fiber track on the collector. Then, the jet speed is determined by multiplying double the width of the fiber track by the applied frequency of the jet deflecting signals. Figure 1.6 shows how jet speed influences the printed fiber pattern while the jet is being deflected transversally to the stage translation direction.

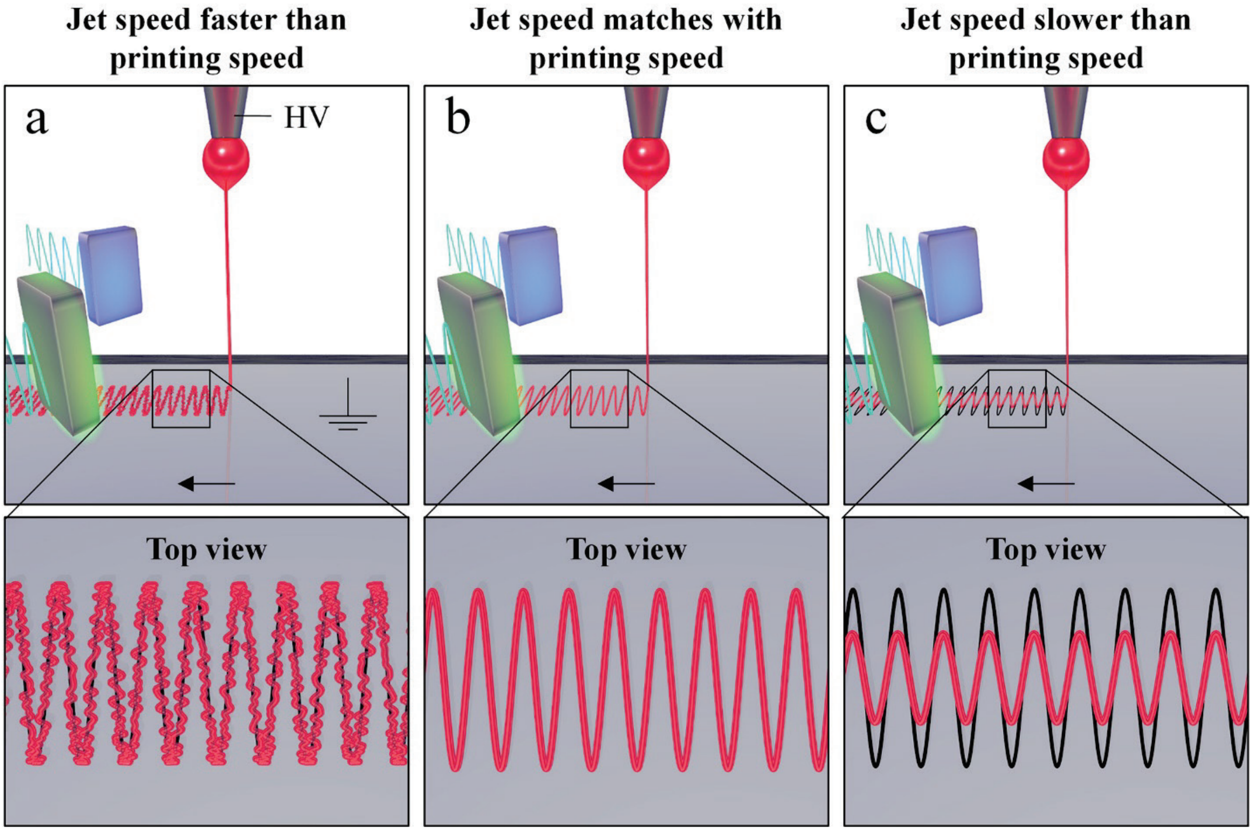
Jet speed faster than printing speed
Jet speed matches with printing speed
Jet speed slower than printing speed
a
HV
b
c
Top view
Top view
Top view

Figure 1.6. Effect of the jet speed on the printed pattern. Patterns printed at high quality are only obtained when the jet speed matches with the printing speed (b). If the jet speed is faster or slower, the quality of the printed pattern deteriorates (a,c). Black arrows indicate the collector motion direction. Black fiber tracks in (a,c) represent the intended fiber track set in the software.

If the jet speed is faster than the printing speed, the jet buckles when it reaches the collector, as the produced fiber length is larger than the needed fiber length. If the jet speed is slower than the printing speed, the jet cuts the corners of the pattern geometry, as it cannot follow the deflection speed that reproduces the shape of the structure. Only matching the jet speed with the printing speed allows printing patterns with high fidelity. The main challenge of matching the jet and printing speeds is due to the high sensitivity of the jet on the ink properties, ambient conditions and processing parameters, which affect the jet dynamics. Thus, it is essential to understand better how the jet speed depends on those variables and how it can be effectively controlled by tuning them. In this thesis, the effect of several variables on the jet dynamics is analyzed to understand how the jet speed can keep stable to match it with the desired printing speed. Those parameters are classified by:

1.4.1. Ink properties

Polymer molecular weight

The molecular weight (MW) of the polymer influences the morphology and microstructures of nanofibers, and can significantly affect their rheological and electrical properties. It affects the degree of entanglement of the polymeric chains in the solution, which should be relatively high to generate continuous fibers[50,51]. During the travel of the jet from the nozzle towards the collector, the jet is stretched, and the polymeric entanglements present in the structure ensure that this stretching happens without breaking the jet. Because of this, monomers cannot be used for EHD processes[52].

In general, if the MW is low, microparticles and beads are formed. On the other hand, too high MWs generate beaded structures[53].

A variety of methods can be employed to determine the MW: M_V (viscosity average), M_N (number average), M_W (weight average) and M_Z (z average)[52].

Polymer concentration

The polymer concentration also plays an important role in the fiber-forming process, as the spinnability of the ink depends heavily on this parameter[1].

Low polymer concentrations generate beads or discontinuous fibers due to the low viscosity and high surface tension of the ink, whereas high polymer concentrations may result in fibers surrounded by beads and pores[53,54]. Too high polymer concentration leads to the inability to maintain the necessary flow of the ink during the printing[1,55]. It is essential to use an optimal concentration of polymer to sustain stable EHD jetting and deposit smooth fibers[50,51].

Moreover, most of the polymeric solutions follow the power law relationship between polymer concentration and fiber diameter, which indicates that the fiber diameter increases with increasing the polymer concentration[1].

Ink viscosity

Ink viscosity is also crucial for determining the microstructure and morphology of the fiber. In general, polymer MW, polymer concentration and ink viscosity are closely related to each other and expected to behave correspondingly[51].

When the ink viscosity is too low, discontinuous fibers and polymer beads emerge in the sample since the ink tends to drip or the jet tends to break because of high surface tension. In contrast, when the ink viscosity is too high, the ink cannot eject from the drop, thus the formation of fibers cannot be developed[51,53]. The ink viscosity can be changed by adjusting the polymeric concentration of the solution, or by using different polymer MWs at a fixed polymer concentration[50].

Ink electrical conductivity

Ink electrical conductivity is dependent on the polymer type, solvent characteristics and other components of the solution. During EHD processes, an electric field is applied between the nozzle at high voltage and the grounded collector. The electrostatic forces will eject the polymeric jet, which will stretch along its fly because of the repulsive forces that exists on its surface.

Too low ink electrical conductivity leads to the elongation of the jet that prevents the formation of uniform nanofibers, and may cause beading. By increasing the electrical conductivity of the ink, the diameter of the fibers can be significantly decreased, and more uniform fibers are formed[51,54]. Exceedingly conductive inks are highly unstable in high voltages, and result in an extreme bending instability, causing broad diameter distributions.

The conducting nature of any ink can be improved by introducing ionic species (diluted acids, bases, salts, polyelectrolytes), which will promote the formation of fibers with small diameter[50,52,53].

Surface tension

The ink surface tension is mostly defined by the surface tension of the pure solvent altered by the properties of the added polymer, and it is closely tied to the ink viscosity. The charge present on the drop surface should be high enough to overcome the surface tension of the ink. The EHD jet moves forward from the drop towards the collector, and the surface tension may cause the breaking of the jet into drops, which leads to the formation of beads instead of fibers[52].

To prevent the breaking of the jet and assure the printing of uniform fibers, it is possible to decrease the surface tension by adding salts and surfactants, but this may introduce impurities into the final fiber[50–52].

Solvent volatility

Solvent volatility is another important aspect of printing approaches based on polymeric solution. The selection of solvent is critical to ensure that the ink is capable of ejecting EHD jets, and plays a pivotal role in the nanofiber porosity[54].

If an ink is prepared from solvents with very low volatility, wet or fused nanofibers may be produced. However, a highly volatile solvent may result in intermittent jetting because of the solidification of the drop at the jet ejection point[50].

Dielectric effect of solvent

This characteristic of the solvent has a large impact on EHD processes. The larger dielectric ensures a finer fiber formation without any beads in it. The incorporation of high dielectric solvents, such as dimethylformamide (DMF), can improve the morphology of the fibers[52].

1.4.2. Processing variables

Nozzle voltage

The fiber fabrication technique requires a HV to induce a change on the drop surface high enough to overcome the surface tension by the electrostatic force. This critical voltage required for initiating the EHD process varies from different solutions[52].

In general, higher nozzle voltages increase the speed of generated fibers, accelerate the solvent evaporation to harvest drier fibers and decrease the fiber diameter[51–53]. However, applied nozzle voltages exceeding the critical voltage will result in the formation of beaded nanofibers, owing to the increase in the jet speed for the same infusion pump rate. Too high nozzle voltages also produce irregular morphologies in the nanofiber structure[54].

Infusion pump rate

The infusion pump rate, or ink flow rate of the polymeric solution from the syringe, is another crucial process parameter. It determines, in part, the materials transfer rate, the jet speed and the morphological structure of the nanofibers[54]. A critical ink flow rate is required for the formation of uniform bead-less nanofibers, and it varies according to different inks composition (as with critical nozzle voltage).

Increasing the infusion pump rate beyond the critical value causes the nanofibers formed to have larger diameter, and results in the formation of beads due to the incomplete drying of the jet during its travel towards the collector and low stretching electrostatic forces[50,54]. Generally, a low flow rate is recommended to avoid perturbations on the electrical field around the jet caused by big drop sizes[51,53].

1.4.3. Setup design

Nozzle diameter

The nozzle inner diameter (ID) must be well adjusted since it is a critical feature to prevent needle blockage or dripping of the ink. In other words, it must be appropriately selected for the properties of the ink and the working conditions.

In general, small nozzle IDs cause the tension created on the drop surface increases, and too small nozzle ID may result in needle blockage. On the other hand, larger nozzle IDs produce stronger perturbations of the electrical field around the jet, which modify consequently the jet dynamics[51,52].

Nozzle to collector distance

The distance between the nozzle and the collector determines the jet flight time and stretching, which have a direct effect on the fiber dryness and diameter, and it may affect the morphology of the fiber as well[53].

Generally, when the working distance is very short, the jet does not have enough time to solidify before it reaches the collector, and beaded structures or flat fibers (also known as nanoribbons) are formed. On the other hand, if the working distance is too long, rounded nanofibers are deposited[50,51,54]. Therefore, an optimal distance between the nozzle and the collector allows the formation of thinner and dried fibers[51].

1.4.4. Ambient conditions

Temperature

A change in the temperature can alter the ink viscosity and the evaporation rate of the solvent. At elevated temperatures, the molecules' motion increases and, consequently, this leads to faster solvent evaporation from the drop surface, which causes an increase of the polymer concentration[52]. Tampering with the temperature allows the average fiber diameter to be controlled. Increasing the temperature has been shown to reduce the mean distribution of the nanofiber diameter[54]. In relatively lower temperature, beads are present in the sample[51].

Relative humidity

The humidity is another factor influencing the surface morphology of the fibers and the formation of beaded fibers, because the humidity can affect electrical charges carried by the jet and the volatilization of the solvent (thus, the solidification process of the printed fibers)[55]. Additionally, available water molecules in close proximity to the jet can dissolve in it or cause phase separation depending on the chemical characteristics of the ink, hence resulting in porous fibers[51,54].

1.5. Printing in steady state

Although EHD jet printing using solvent-based inks is considered as a very promising nano-writing method, certain difficulties in understandings and maintaining the jet speed constant over time have slowed down its automation and commercialization[56]. Main challenges include the controllability and stability of the jet speed during the printing and the lack of a reliable method for initiating the jet (both factors affect the uniformity of the printed fiber diameter)[57–60].

This printing approach is influenced by interactions of the electric field force, gravity force, capillary force, viscous force, air resistance and surface tension that are present on the drop surface[57]. Previous works have already demonstrated the influence of several process parameters on the jet speed[60–62], but further studies are needed to understand how to improve the printing stability. To gain insight and comprehension, the effect of the drop size and drying of its surface on the printing reproducibility is analyzed in this thesis, as both variables have been overlooked.

On the one hand, the droplet generation can be affected by multiple factors, such as the nozzle diameter, process parameters and solution properties[57]. The presence of the drop modifies the voltage gradient between the nozzle and the collector, altering the strength in which the electrical field pulls the jet, and thus influencing the jet speed. This effect on the jet speed has two origins. First, the drop introduces an electrical resistance that decreases the potential at the drop tip (larger drop size leads to larger potential drop and, consequently, lower the electric field at the drop tip). Then, at a set nozzle to collector distance, an increase of the drop size has associated a decrease of the distance between its surface and the collector, and the effective electric field is increased at the drop tip as a result. These two cases cause a variant jet speed, as its speed will not be constant over time. Figure 1.7 simulates how the drop size affects the electrical field in its surroundings[34].

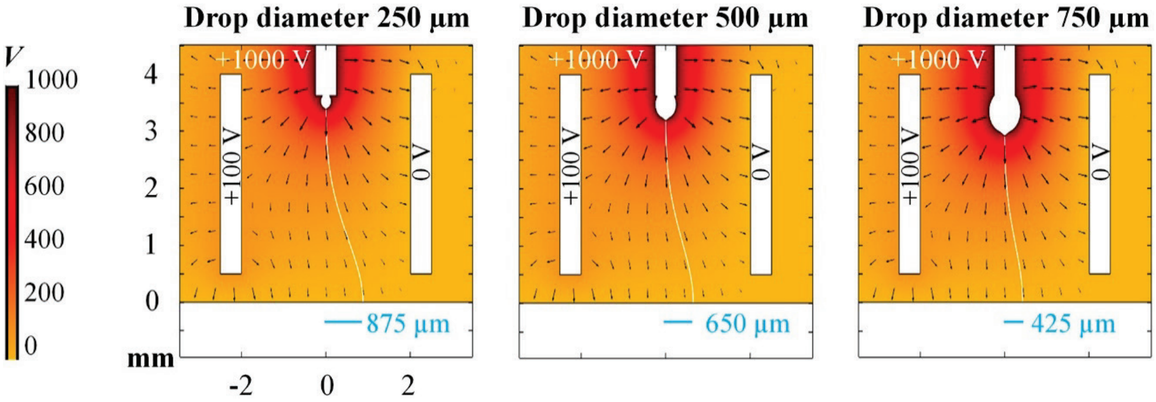

Figure 1.7. Analysis of the drop size effect on the electrical field. Electrostatic jet deflection is used to visualize how the drop size affects the jet speed. In this simulation, nozzle voltage was fixed at 1000 V, voltage bias applied on the electrodes at 50 V and deflection amplitude at 100 V.

On the other hand, the polymer concentration and the solvent composition define the drop properties, which may change during the printing if a considerable amount of solvent evaporates from the drop surface. As the jet speed is strongly influenced by the drop properties, it is important to minimize solvent evaporation from the drop to avoid printing heterogeneous patterns.

Therefore, it is challenging and meaningful to investigate the effect of the drop size and the drying of its surface on the printing stability over time, and electrostatic jet deflection printing facilitates this analysis, as it allows us to monitor not only the jet speed during over time, but also to examine the deposition location of the pattern when it is printed. Printing in steady states implies printing at constant jet speed and stable deposition location. If the jet speed changes over time, the amount of fiber that is placed on the collector will be different during the printing, collecting heterogeneous patterns as a result. If the deposition location changes over time, owing to the jet moving around the drop and its ejection point changes, the electrical field on the jet surrounding may change, altering the speed at which the jet is propelled towards the collector and printing heterogeneous patterns as a result. Both situations involve printing in a non-steady state, so they must be avoided to get reproducible prints.

Figure 1.8 illustrates the printed patterns that those instabilities generate:

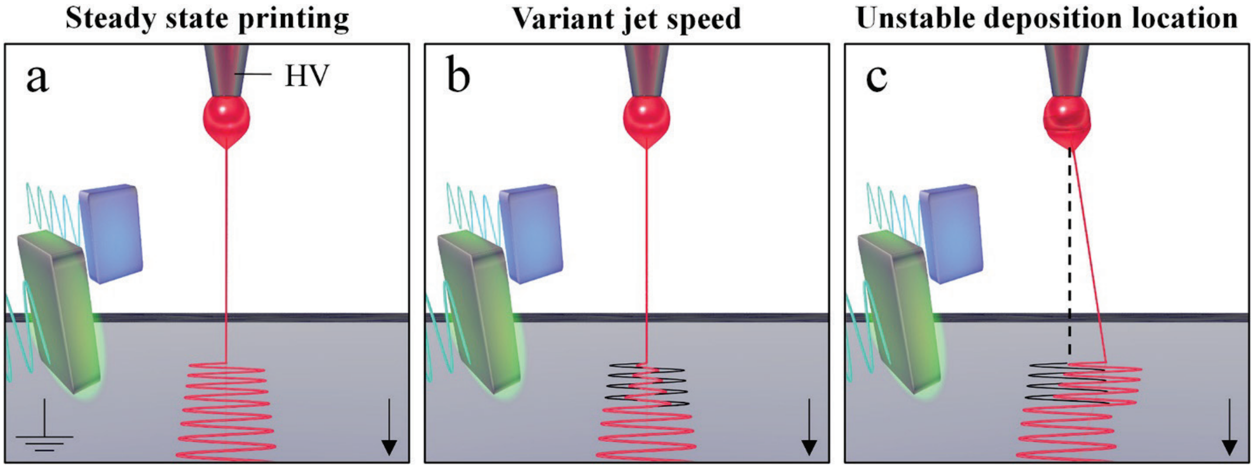

Figure 1.8. Heterogeneous fiber tracks resulting from different jet instabilities. Stable jet speed and deposition location allow printing fiber tracks in steady state (a), while heterogeneous fiber tracks will be placed on the collector if the jet speed (b) or the deposition location (c) changes during the printing. Black arrows indicate the direction of the collector motion. Black fiber tracks in (b,c) represent the intended fiber track set in the software.

1.6. EHD jet printing using molten polymers

EHD jet printing using molten polymers (commonly known as melt electrowriting, MEW) draws attention from both academia and industry due to the absence of solvents, allowing the absence of toxic residues accumulated during the process or remaining in the final product[63]. MEW is an additive manufacturing technique that is based on melting a polymer, to be used as an ink, and establishing later an electrical field between the nozzle and the collector to expel the jet towards the printing area, to create micro- and nano- polymeric fibers arranged in a pattern defined by mechanical stages[64]. From a manufacturing perspective, MEW can be considered as a hybrid fabrication technology between EHD jet printing and microextrusion, as it involves the extrusion of a molten polymer and the ejection of electrified jets towards the collector[64,65]. After the jet ejection, the polymeric filament cools and crystalizes when it travels from the nozzle towards the collector, leaving the solid polymer fiber on the collector[63,64]. The diameter of the printed fiber can be conveniently varied in a wide range from 800 nm to 50 µm, which is much thicker than the fibers fabricated using solvent-based inks[65].

A representative MEW setup has three important components[66]. The first one is the printhead where the polymer is melted, and it consists of a heating system and a thermal sensor. The second component is the HV supply that creates the electrical field between the nozzle and the printing area. Finally, the third component is the movable collector where the fibers are printed.

There are several important advantages of MEW versus other printing approaches[64,65]. Firstly, it is solvent-free and avoids the use of volatile and toxic chemicals, which otherwise would accumulate or require venting from the system. Coupled with using medical-grade polymer feedstock which has a long history of use as implants, MEW does not require degassing or post-process solvent removal which aids in translating to the clinic[67]. Secondly, micro-fibers can be accurately placed on the collector, which allows creating highly porous structures for bio-applications by leaving spaces between deposited fibers. MEW scaffolds tend to have high porosity, typically from 80-vol% to 98-vol% pore volume[68], which enables both cell attachment, proliferation and self-organization within the scaffold pores. Thirdly, the fiber diameter can be accurately set by balancing the instrument parameters so that the process is constant throughout the printing period, which may last multiple hours and days[69]. On the other hand, MEW also presents certain limitations, such as generally larger fiber diameter (from a few microns to fifty microns) in comparison with the ones obtained using solvent-based inks, or the high processing temperatures required for some polymers, which may lead to their fast degradation[63,65].

Regarding the areas of implementation, the scalability and reproducibility of MEW make it viable in a myriad of application fields, such as soft sensors[70–72], filtration and separation[73,74], flexible electronics and robotics[75], biomedical applications[76,77] and drug delivery[78–80] among others.

Poly(ε-caprolactone) (PCL) is currently a gold standard feedstock for MEW, and operating conditions can be tuned to obtain a specific fiber diameter during the printing[69]. This condition is important, as the fiber diameter has to be decreased and the jet speed must be increased to implement EHD jet deflection in conventional MEW printer in order to expand its printing capabilities (Figure 1.9).

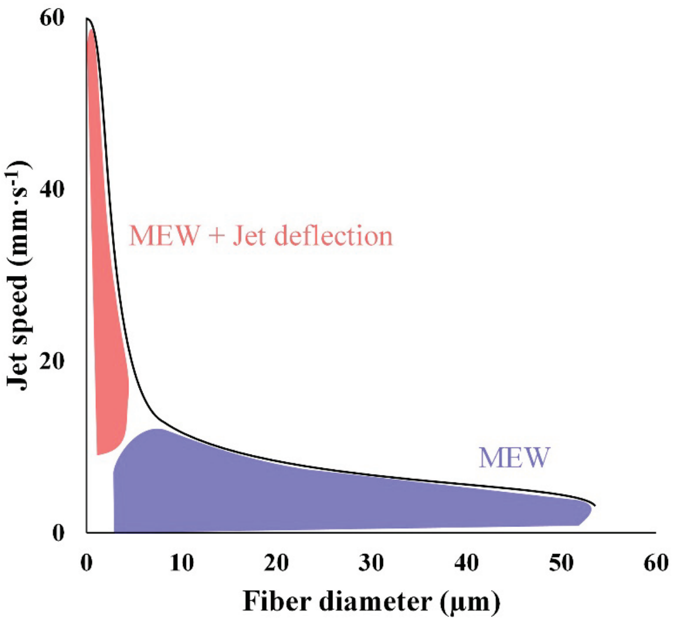

Figure 1.9. Comparison between printing capabilities of conventional MEW and EHD jet deflection printing of molten polymers. Conventional MEW typically deposits thick fibers at slow speed. After optimizing the operation conditions to get thin and fast jets, and implementing EHD jet deflection, the upgraded MEW system can achieve submicron prints at fast speed.

For this reason, it is important to note the effect of the molten polymer properties and the working conditions on the jet dynamics and thickness.

Polymer molecular weight

The polymer MW affects the viscosity of the molten polymer and the stability of the EHD jet. Using polymers with low MW gives low ink viscosity when the polymer is melted, but the jet may break during the printing due to its insufficient viscoelasticity, not capable of maintaining the thin liquid jet in a stretched airborne state.

When the polymer MW is increased, the ink viscosity and elasticity increase due to higher entanglement of the polymeric chains. Consequently, the jet stability is improved and the jet breaking during the printing are avoided.

Nozzle diameter

The nozzle diameter has a huge effect on the diameter of the printed fibers. Generally, smaller nozzle diameters provide thinner fibers due to the large pressure drop, and thus reduction of the flow rate of the molten polymer.

Pressure

The pressure applied to the syringe to push the molten polymer also directly affects the fiber diameter and its morphology. The pressure defines the flow rate with which the molten polymer is expelled through the nozzle, and it has been shown that low flow rates are needed for MEW thin fibers because more charges exist on polymer melts with a lower flow rate[81].

Lower pressure applied on the syringe results in lower flow rate of the molten polymer through the nozzle, which entails the printing of thin fibers. On the other hand, higher pressures yield thicker fibers by causing higher flow rate, and the jet will have less time to be stretched before it reaches the collector.

High voltage applied

The HV can be applied either to the nozzle or to a metallic plate under the glass collector (which prevents any damage to the heating sensors in the printhead in case of arcing). Both options create the electrical field needed to expel the jet towards the printing area. The HV range applied for MEW depends on the material to be EHD jetted and the working conditions. The conductivity and the viscosity of the molten polymers are the crucial properties that define the HV needed to get stable jet and print desired fiber diameter on the collector.

Generally, higher applied voltage leads to faster jets and thinner fibers, as stronger electrical field causes more stretching of the jet while it is flying towards the printing area.

Printhead temperature

Choosing the appropriate temperature of the printhead mainly depends on the melting point of the polymer. First, the polymer pellets are filled into a syringe, which is placed into the printhead. Then, the printhead temperature starts to rise, melting the polymer. Typical working temperatures are set 10 – 30 ºC above the polymer melting temperature[63].

Higher temperatures result in lower viscosities of the molten polymer, but too high temperature leads to faster polymer degradation and, separately, an insufficiently solidified jet deposition that does not support high-fidelity printing.

Nozzle to collector distance

The nozzle to collector distance plays an important role as it provides time for the jet to cool down and solidify before the fiber reaches the collector. Therefore, too short nozzle to collector distances may result in the deposition of molten fibers and crossover points caused by their fusion[63,66]. On the other hand, larger nozzle to collector distance allows the elongation and the stretching of the jet, which deposits thin fibers on the collector. However, at a fixed high nozzle voltage, the electrical field becomes weaker as the nozzle to collector distance increases, and thus the jets will be ejected at a slower speed. The typical nozzle-to-collector distance is about 3 – 5 mm.

1.7. Objectives of the thesis

The aims of the present thesis is, first, to demonstrate the capabilities of electrostatic jet deflection printing to accurately align and deposit fast EHD jets into well-defined fiber tracks. Using this strategy, fiber tracks with preset width, fiber alignment and directionality, as well as with easily quantifiable and controlled fiber density, should be printed. In addition, combining the jet deflection with the stage translation would enable us to pattern the same fiber length into tracks whose widths can be selected between millimeters down to the submicrometer scale, regardless of the jet speed, stage translation speed, or other fiber parameters.

The second goal of this thesis is to determine in situ the EHD jet speed without analyzing individual printed fibers, but from the overall size of the printed fiber track while the jet is being electrostatically deflected. This method would allow quantifying easily the jet speed using standard optical inspection equipment

The third objective of the present thesis is to determine the dependence of the jet speed on different process parameters, ink properties and ambient conditions (using electrostatic jet deflection). This data would allow us to understand how to tune the jet speed during the printing.

A fourth purpose consists in identifying several instabilities that occur during the printing process and analyzing how they are influenced by different printing parameters. Later, several strategies have to be proposed to indicate how avoid those instabilities.

Finally, a fifth challenge addressed in this thesis is the implementation of the electrostatic jet deflection on EHD jets from molten polymer. This work has been carried out during the research stay conducted in Prof. Paul Dalton group, at the University of Oregon (United States). As EHD jets made from molten polymers are more viscous and are much slower than EHD jets made from solvent-based inks, the printing conditions have to be changed first to eject thin and fast jets. After that, deflecting electrodes can be placed around the nozzle to explore EHD jet-deflection printing using molten polymers.

Chapter 2

Materials and methods

2.1. Materials and inks preparation

For solvent-based inks formulation (Chapters 3 – 6), polyethylene oxides (PEO) of various MWs were purchased from Sigma-Aldrich (#182001, viscosity-average molecular weight (M_V) 0.3 MDa; #182028, M_V 0.6 MDa; #372781, M_V 1 MDa; #189472, M_V 5 MDa). Ethanol (EtOH), acetone and ethylene glycol (EG) were acquired from different sources. Reagent-grade deionized water (H_2O) was obtained from Purelab flex (Elga). All chemicals were used as received, without further purification, and all inks were kept in sealed vials at room conditions during several months. Silver (Ag) NPs of diameter ca. 50 nm were synthesized using polyvinylpyrrolidone (PVP) as ligand[82]. After synthesis, the NPs were thoroughly washed by multiple precipitation and redispersion cycles using ethanol as solvent and acetone as antisolvent, and finally, and were precipitated for posterior use. Thus, obtained Ag NPs could be dispersed later in polar solvents, such as water and ethanol. Deionized water was the main solvent, to which some amounts of ethanol or ethylene glycol were added to tune the ink properties. The use of ethanol allows decreasing the ink surface tension and increasing the solvent evaporation rate, thus enabling the use of lower voltage for EHD jetting and facilitating jet drying into mostly solid fiber upon deposition, respectively. The use of ethylene glycol allows on the other hand reducing the evaporation rate during printing and achieving more constant drop properties over time. PEO inks were prepared by dissolving PEO (typically 2 – 10 wt%, depending on its MW) in the solvent mixture during 24 hours under magnetic stirring. Higher MW PEO generally improves jet stability and allows using lower jetting voltages[83]. Ag NPs inks were prepared by adding the PEO ink into a flask containing precipitated Ag NPs and dispersing them using ultrasonication and magnetic stirring.

For molten polymers used as ink (Chapter 7), medical grade PCL was purchased from Corbion (PURASORB PC 12), and it was used as received. Pellets of the polymer (≈ 0.8 g) were added into a syringe (Nordson EFD #7012074, 3mL), which was later placed into an oven (Thermo Fisher, Isotemp 100L FA) at 90 ºC for 2 days to get a homogeneous degassed melt before running the experiments.

Ink electrical conductivity and viscosity (Chapters 5 and 6) were measured using a water hardness sensor (Lutron electronic, model CD–4309) and a viscometer (Brookfield engineering, model DV2T, with spindles SC4-18 and SC4-34). The entanglement number (η_e), or average number of entanglements by each polymer chain[84], was estimated using Shenoy's model[85–87]:

$$\eta_e = \frac{\phi_P \cdot M_w}{M_e} \tag{2.1}$$

Where η_e is the entanglement number, ϕ_P is the polymer volume fraction, M_w is the polymer weight-average MW and M_e is the average MW between entanglements in the melt (for PEO, $M_e = 2100$ for all range of MW[85]).

2.2. Printer setup and printing protocol used for solvent-based inks

The ink was loaded into a glass syringe (Hamilton #81320, 1 mL) and supplied to the nozzle by a syringe pump (Harvard Apparatus, Pump 11 Pico Plus Elite 70-4506) with infusion pump rates in the range 20 - 70 nL·min^{-1}. Either stainless needles with blunt tips (Hamilton N726S, 26s gauge, 127 µm ID, 474 µm OD) or borosilicate glass tips, with a diameter of c.a. 200 - 300 µm, were used as nozzles. Borosilicate glass tips were manufactured by pulling borosilicate glass tubing (Sutter Instruments, B100-50-15; 1.0 mm OD, 0.50 mm ID) using a pipette puller (Sutter Instruments P-97) and manually breaking the tips by scratching two tips against each other. Later, the large (tubing) end of the glass tips were glued atop of a stainless-steel needle with a blunt end (B Braun Sterican, 27 gauge; 0.47 mm OD). No surface treatment was applied to their ends. A positive potential was applied to the nozzle using a Matsusada AU-20P15 high voltage supply. Silicon wafers (University Wafers #452, p-type, <100>) were used as the substrate, and were placed on an electrically grounded plate, mounted atop of a motorized XY translation stage (PI miCos linear stages PLS-85 with 10 mm range in both X and Y with RS422 encoders). Prior to printing, silicon wafers were cleaned with isopropanol to remove organic contamination.

EHD jetting was initiated by applying a HV in the range 800 - 1200 V on the needle and punching the meniscus with a sharp tip for breaking the surface tension of the drop. The voltage required for jet initiation was lower for nozzles and pendant drops of smaller size. Once the jet was initiated, it was printed in a small area of the substrate for 2 minutes for stabilizing it, to ensure it reaches consistent jet speed before collecting data. To determine the effect of different parameters on the produced patterns, the stage translated the collector describing a zigzag patterns composed of 10 mm segments spaced at 0.5 mm, until a printing area of 10 x 10 mm^2 was covered (Figure 2.1). The jet trajectory was analyzed to detect changes in the location where printed patterns are deposited, and its deviation was monitored establishing the centerline of the fiber track printed on the collector as reference (Chapter 6). The collector was either translated continuously to print 2D fiber tracks or only moved in steps between which the substrate remained motionless while 3D structures were printed by electrostatic jet deflection. The separation between the nozzle tip and the printing collector was typically set at 3 mm, but it was modified in Chapter 5 to analyze the effect of the nozzle to collector distance on the jet speed.

The jet was deflected from its default trajectory using jet-deflecting electrodes (made of steel) located 10 mm away from the default jet trajectory[34]. The size (height, width and thickness) of those electrodes was 10 × 3.0 × 0.5 mm, and they were positioned at 90 degrees from one another. In this configuration, the electrodes were glued to a plastic holder made with an SLA 3D printer (Formlabs Form 2) using RS-F2-GPCL-04 clear resin while the electrode to substrate distance was fixed at 1 mm. As practiced conventionally, our 3D printing was controlled through the parameterization of the layer-by-layer deposition process to print an object with predefined geometry, size, and microstructure. A custom-made software (developed in LabVIEW) together with a DAQ card (National Instruments USB-6259) generated the jet-deflecting electrodes voltages, defined as a function of the geometry of the predesigned pattern, the layer printing frequency and the signal amplitude. Synchronized analog signals (max. ± 10 V) provided by the DAQ card were amplified (max. ± 2000 V, with Matsusada AMJ-2B10 and Trek 677B amplifiers) and applied to the jet-deflecting electrodes typically within 500 - 2000 V amplitude and frequency selected in the range 20 - 500 Hz.

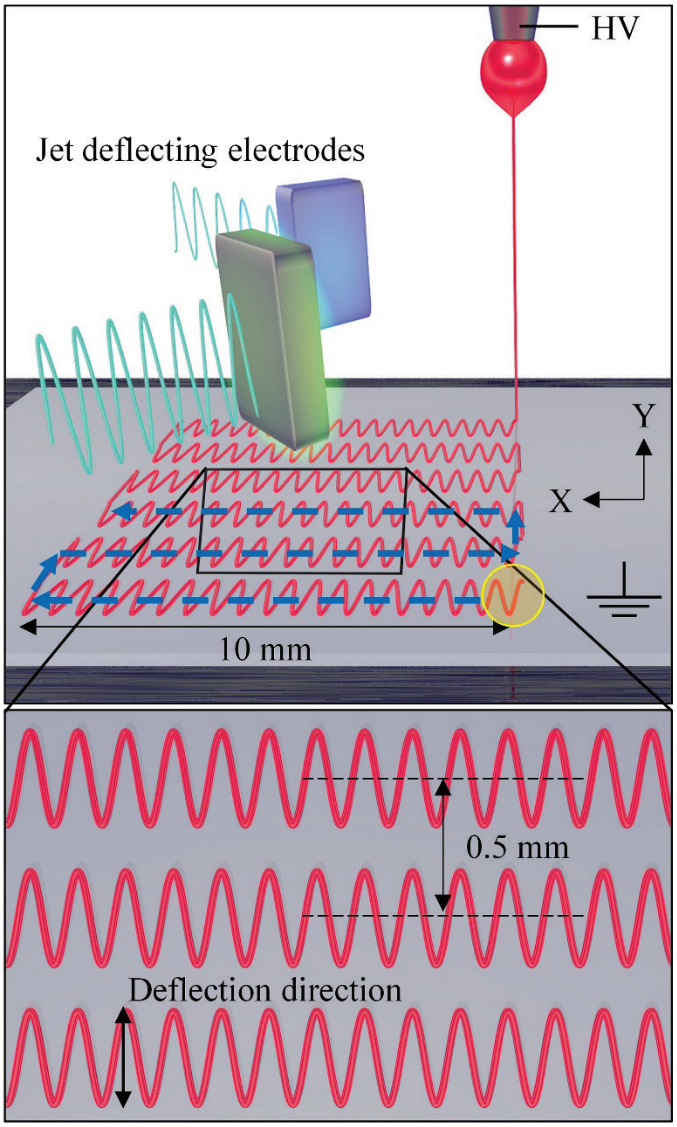

Figure 2.1. Schematics of the EHD jet deflection printing and complete travel of the jet (default trajectory) over the substrate. Initially, the mechanical stage translates along the X-axis for 10 mm from an initial X = 0 position (orange circle). Later, it moved describing zigzag patterns (blue lines) composed of 10 mm in X-axis spaced at 0.5 mm in Y-axis, until a 10 mm x 10 mm square has been printed, containing 20 lines along the X-axis. Meanwhile, this motion is produced, the jet is periodically deflected by auxiliary electrodes along Y (transversally to the stage main translation direction).

During the printing process, the ink drop at the end of the glass tip was monitored using a CMOS camera (Basler acA2040-25gc) mounted on an optical microscope consisting of a 12X lens with adjustable zoom and focus (Navitar 1-50486), a 2X lens adaptor (Navitar 1-62136) and a 5X microscope lens (Mitutoyo 1-60226). The nominal working distance resulted in 34 mm, and the optical axis was set horizontal. A high-intensity light source (AmScope HL-250-A) was positioned behind the observed object under ca. 5° angle from the camera's optical axis, so direct light did not reach the camera. For real-time monitoring of the liquid drop during the printing process, a paper sheet was placed between the drop and the light source (bright-field setting). Figure 2.2 illustrates the setup used for deflecting electrostatically EHD using solvent-based inks (Chapters 3 – 6).

The printing process was carried out under room ambient conditions, at a temperature and relative humidity in the ranges 18 – 20 °C and 35 – 65%, respectively. However, to ensure reproducible solvent evaporation, a laminar flow of dry nitrogen gas (700 mL·min^{-1}) was supplied around the jet from a tube located next to the nozzle.

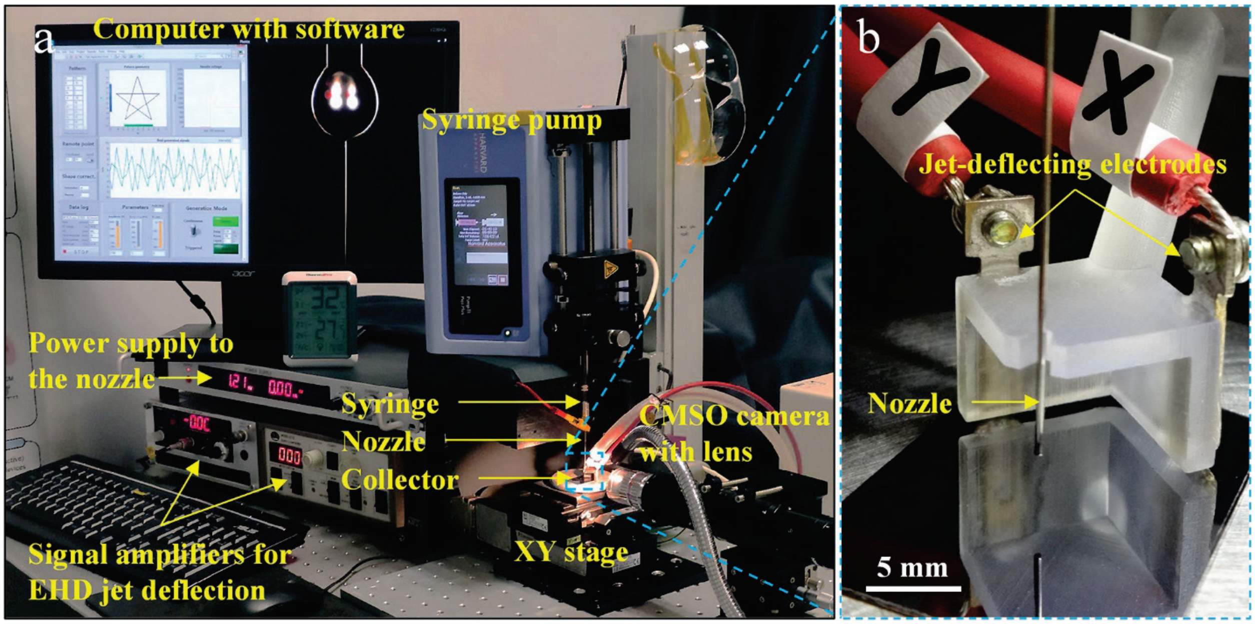
a
Computer with software
Syringe pump
Power supply to the nozzle
Syringe
Nozzle
Collector
CMSO camera with lens
XY stage
Signal amplifiers for EHD jet deflection
b
Y
X
Jet-deflecting electrodes
Nozzle
5 mm

Figure 2.2. EHD jet-deflection printing setup using solvent-based inks. a) Conventional EHD jet printing setup is improved through the implementation of auxiliary electrodes around the nozzle to control the deposition of the airborne jet on the collector. b) Jet deflection electrodes arrangement, with the electrodes mounted on a plastic holder made with a 3D printer.

2.3. Printer setup and printing protocol used for molten polymers

A syringe attached to the nozzle and filled with PCL pellets was placed in a printhead and was heated at 80 ºC using a heating control (Novus Automation, N1020). The melt was supplied to the nozzle (Nordson EFD 32G, 0.10 mm of ID) using an adjustable air pressure system (SMC, ITV series), connected to the syringe through a pressure adapter (Nordson EFD, #7012341) and supplied 0.5 bar using a compressor (Makita, MAC320Q). A high voltage source (Gamma high voltage, RR3-20P/24/M1219) was used to apply a positive potential to the nozzle. Glass microscope slides (VWR, #48300-026) and silicon wafers (University Wafers #857, p-type, <100>) were used as the collector, and were placed on an electrically grounded metal plate, mounted atop of a motorized XY stage (Zaber, LSQ300A). Different G-Codes that define the stage path were generated using Matlab. The stage translation speed was set at 1 – 2 $mm \cdot s^{-1}$, and the nozzle to collector distance was fixed at 5 mm. The printing process was carried out under ambient conditions, at a temperature and relative humidity in the range of 19 – 21 ºC and 30 – 60 %, respectively. EHD jetting was initiated by applying a HV (7 kV) to the nozzle and waiting a few minutes until the jet was ejected. Once the jet was initiated, it printed in a small area of the collector for 15 minutes for stabilizing its speed. Figure 2.3 illustrates the setup used for deflecting electrostatically EHD using molten polymers as inks (Chapter 7).

The jet was deflected from its default jet trajectory using four EHD jet-deflecting electrodes located 7.5 mm away from the nozzle. Two electrodes were placed on the X-axis, while the other two on the Y-axis. A DAQ card (National Instruments, USB-6259) was used to generate the four synchronized analog signals (max ± 10 V) which after amplification (max. + 10 kV, Ultravolt, HVA series) were applied to the jet-deflecting electrodes. These voltages had a DC component (*i.e.*, a bias voltage) of 3 kV and an AC component with a peak-to-peak amplitude of 4 kV and a frequency of 10 – 100 Hz. The AC component of one electrode is equal to -1 times the AC component of the other electrode in the same pair.

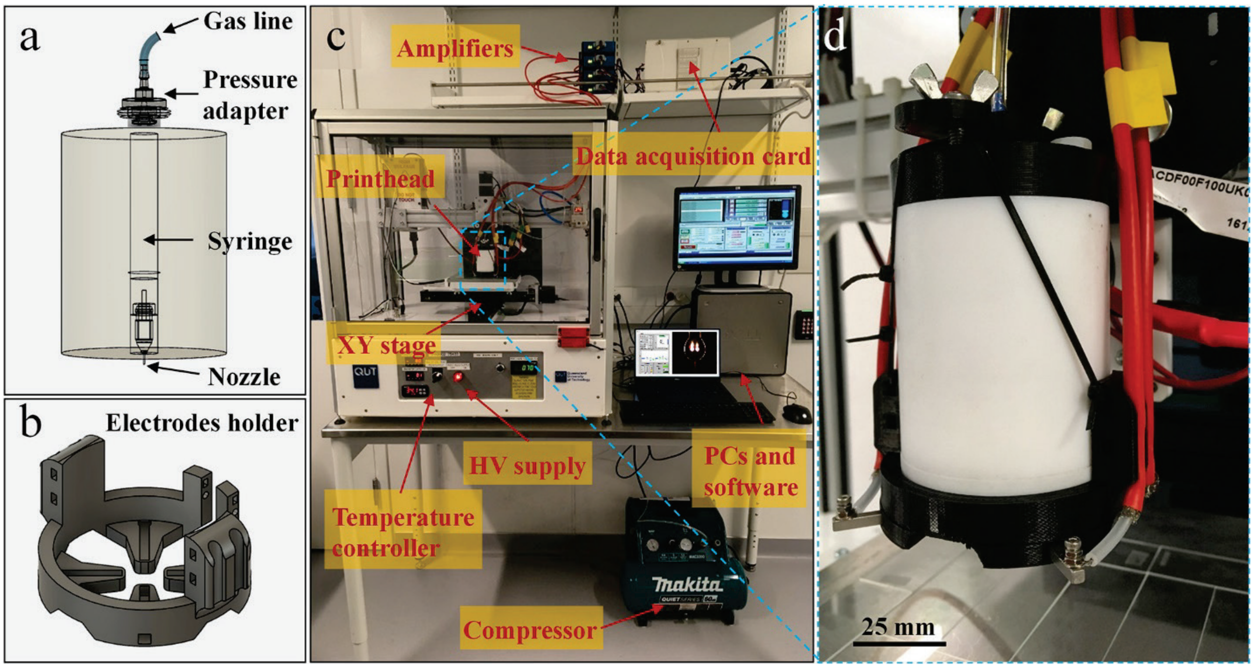
a
Gas line
Pressure adapter
Syringe
Nozzle
b
Electrodes holder
c
Amplifiers
Data acquisition card
Printhead
XY stage
HV supply
PCs and software
Temperature controller
Compressor
d
25 mm

Figure 2.3. EHD jet deflection printer setup using molten polymers. a) Conventional printhead used in common MEW setups, composed of a syringe placed in a heating unit and connected to a gas line through a pressure adapter. The nozzle typically protrudes about 1 mm. b) Design of the electrodes holder. c,d) Setup of the upgraded MEW printer (c), illustrating all of the components and magnifying the printhead and the electrodes holder (d).

2.4. Drop size and volume computation

The ink drop radius was measured during the experiment to estimate the drop volume (Chapter 6). Scheme 2.1 illustrates the method used to estimate the drop radius and volume from the CMOS camera frames.

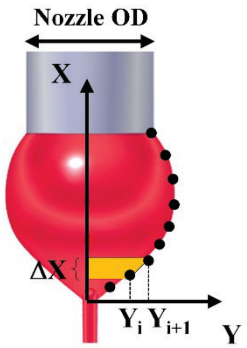

Scheme 2.1. Drop volume estimation. Coordinate system used to determine the drop size.

First, a coordinate system was defined around the drop by fixing its origin at the jet ejection spot and dividing half of the drop into ΔX portions. An XY digitizer provided the coordinates, which were used to compute ΔVi:

$$\Delta V_i = \frac{1}{3} \cdot \pi \cdot \Delta X \cdot (Y_i^2 + Y_{i+1}^2 + Y_i \cdot Y_{i+1}) \tag{2.2}$$

Then, the drop volume was calculated using:

$$V_d = 2 \cdot (\textstyle\sum_{i=1}^{n} \Delta V_i) \tag{2.3}$$

2.5. Jet speed and flow rate determinations

To determine jet speed, the jet was cyclically deflected in a direction normal to that of the stage displacement, and the width of the printed track was then measured with a confocal microscope. From such measured width of the fiber track (L) and the known frequency of the jet deflecting signal (ν), the jet speed at its arrival at the substrate (U_J) was estimated as:

$$U_J = 2 \cdot L \cdot \nu \tag{2.4}$$

To determine the polymer flow rate, two assumptions were made: (1) the fibers have a circular cross-section and are not porous, so their volume coincides with the volume of printed polymer and can be computed from the observed fiber diameter D and L; (2) the ink density (ρ_{Ink}) can be calculated from the known weights and densities of the constituent polymer and solvents. Thus, the polymer volumetric flow rate propelled in the jet ($Q_{P,jet}$) can be estimated as:

$$Q_{P,jet} = U_J \cdot A = \frac{\pi}{2} \cdot L \cdot \nu \cdot D^2 \tag{2.5}$$

Then, multiplying $Q_{P,jet}$ by the polymer density (ρ_P), the polymer mass flow rate in the jet ($M_{P,jet}$) can be calculated as:

$$M_{P,jet} = \frac{\pi}{2} \cdot L \cdot \nu \cdot D^2 \cdot \rho_P \tag{2.6}$$

Finally, by assuming that the weight concentration of polymer in the ink ($C_{P,Ink}$) at the jet is equal to the initial solution value (in absence of evaporation), upper bounds to the jet mass flow rate (M_{Jet}) and the jet volumetric flow rate (Q_{Jet}) can be estimated:

$$M_{Jet} = \frac{M_{P,jet}}{C_{P,ink}} \tag{2.7}$$

$$Q_{Jet} = \frac{M_{Jet}}{\rho_{Ink}} \tag{2.8}$$

2.6. Fiber characterization

Deposited fiber tracks shown in Chapter 3 were inspected after printing by confocal microscopy and macro-photography. Confocal imaging was done on Sensofar PLu Neox microscope with polarized light enhancing the contrast between printed fibers and the silicon substrate. Confocal images larger than 0.5 mm were obtained by stitching multiple images of a smaller field of view, performed within Sensofar software. Micro-photography of rotating PEO fiber tracks (Chapter 3) was performed using the same CMOS camera and microscope assembly that was used for monitoring the printing process, while the camera was imaging the sample from the top, light source was fixed at an oblique angle to the substrate, and the substrate was rotated for 360 ° around camera's optical axis.

To simulate machine-inspection imaging of printed fiber tracks (Chapter 4), PEO fiber tracks collected as the substrate is moved were imaged after printing using the same CMOS camera and microscope assembly that was used for in situ inspection.

Fiber diameters showed in Chapters 5 and 6 were inspected using an Auriga scanning electron microscope (SEM) from Carl Zeiss operated at 1 - 5 kV and using either an in-lens backscattered electrons detector or a secondary electrons (SE2) detector. Previously, the samples had been sputtered with a thin copper layer using a DC magnetron sputter (Emitech K575X, 85 mA, argon, 90 seconds) to improve the quality of SEM images and to protect the PEO fiber from degradation/shrinkage caused by the electron beam.

Fibers tracks obtained in Chapter 7 were inspected using several optical microscopes (Thermo Fisher EVOS XL Core and Keyence VHX7000). 3D structures and individual fibers showed in this chapter were analyzed using the SEM operated at 1 kV (SE2 detector). Previously, the samples were sputtered with a thin silver layer using a DC magnetron sputter (Emitech K575X, 85 mA, argon, 90 seconds) to improve the quality of SEM images.

2.7. Electrical current measurement

Energy balances estimated in Chapter 5 were computed by measuring the electrical current during the printing using an electrometer (Keithley, 6517b) and after calculating the jet speed and measuring the diameter of the printed fibers.

Chapter 3

Patterning with aligned electrospun nanofibers

The capabilities of electrostatic jet deflection printing to deposit submicron fibers at fast speed are showed in this chapter.

EHD jets can be electrostatically deflected to print a wide variety of fiber tracks with well-defined width and fiber orientation. Combining the electrostatic deflection of the jet with the translation of the stage allows the precise control of the fiber track width over a broad range, ranging from submicrometric single nanofiber width to millimeter-wide tracks.

3.1. Fiber tracks with controlled width and fiber orientation

The schemes of conventional and jet-deflection EHD printing processes are illustrated in Figure 3.1. As described in Chapter 2, a conventional EHD printer (Figure 3.1a) generally comprises a thin nozzle, a syringe pump to supply ink from the syringe to the nozzle, an XY motorized stage that translates a grounded collector, a power supply that provides high voltage to the nozzle and a control system. The jet-deflection EHD printer (Figure 3.2b) additionally contains two auxiliary electrodes placed at 90 degrees to one another and located around the nozzle to modify the electric field in the vicinity of the jet during its travel to the substrate, two amplifiers that intensify the analog signal applied to the deflecting electrodes, and additional controls to generate the jet deflection signal[34].

As observed from the left side of the confocal images in Figure 3.1c,d, the track obtained with the conventional EHD printing process is made up of buckled fiber, with uncontrolled orientation and distribution. Notice that the width of the printed fiber track is variable with poorly defined edges. It is also difficult to predict and adjust it, as it depends on the dynamics of buckling, which in turn depends in a complex way on numerous parameters, including ink composition, applied voltage, stage translation speed and ambient humidity among others (Figure 3.2a, top). When turning the jet deflection field on (right side of Figure 3.1c,d), the same fiber length is aligned at a chosen angle with respect to the track direction (set by the stage movement), thus creating a track of well-defined width.

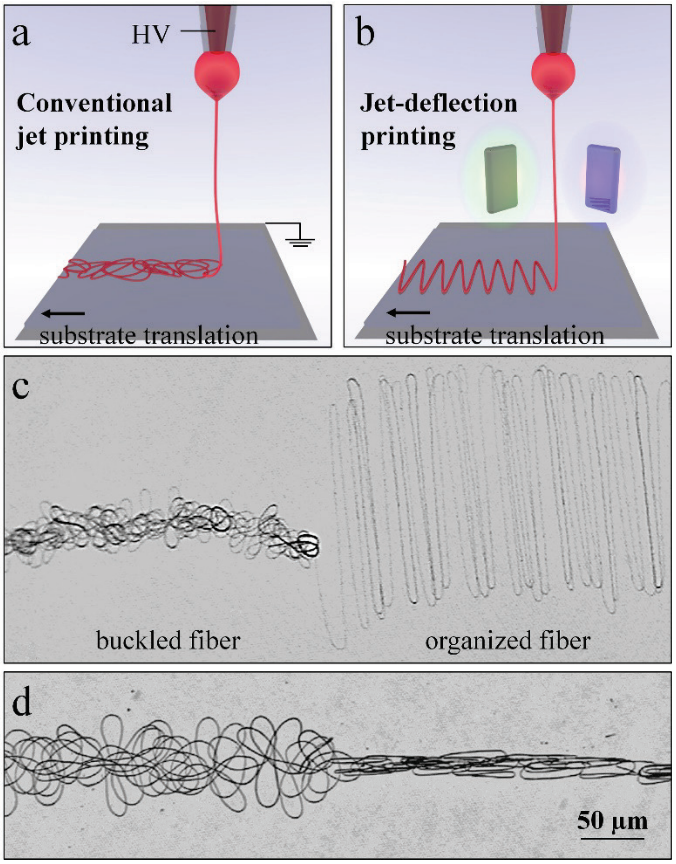

Figure 3.1. EHD printing of submicrometer fibers into tracks while translating the substrate. a) Scheme of the conventional EHD printing process. b) Scheme of the jet-deflection EHD printing process where the fiber deposition is controlled via electrostatic jet deflection using auxiliary electrodes. c,d) Confocal microscopy images of fiber tracks that initially (left side) contain buckled fiber printed using conventional EHD jet printing, and which, upon turning on the jet deflection field (right side), develops into a wider (c) or thinner (d) fiber track containing fibers aligned perpendicular (c) or parallel (d) to the track direction defined by the movement of the stage.

When using jet deflection, Figure 3.2a shows that the width of the fiber tracks stays constant upon changing the stage translation speed. When the jet speed exceeds the stage translation speed, the fiber track width is strictly defined by the jet speed and by the selected jet deflection frequency and amplitude (Figure 3.2b,c,d). At a fixed signal amplitude (A), doubling the frequency (v) decreases the track's width in half because the width is determined by the jet's swing during one half period (since the fiber does not stretch under the pull created by electrostatic jet deflection). Changing the signal amplitude at a fixed frequency has the opposite effect, an increase of amplitude translating into wider tracks (Figure 3.2b,d). A lower limit exists, however, on the amplitude and frequency of the jet-deflecting signal for which aligned fiber can be printed.

For example, in Figure 3.2b, at 100 Hz, this lowest amplitude was reached between 1500 and 2000 V. Below this threshold value, the length of fiber produced is larger than the length of fiber needed for printing, and the fiber buckles.

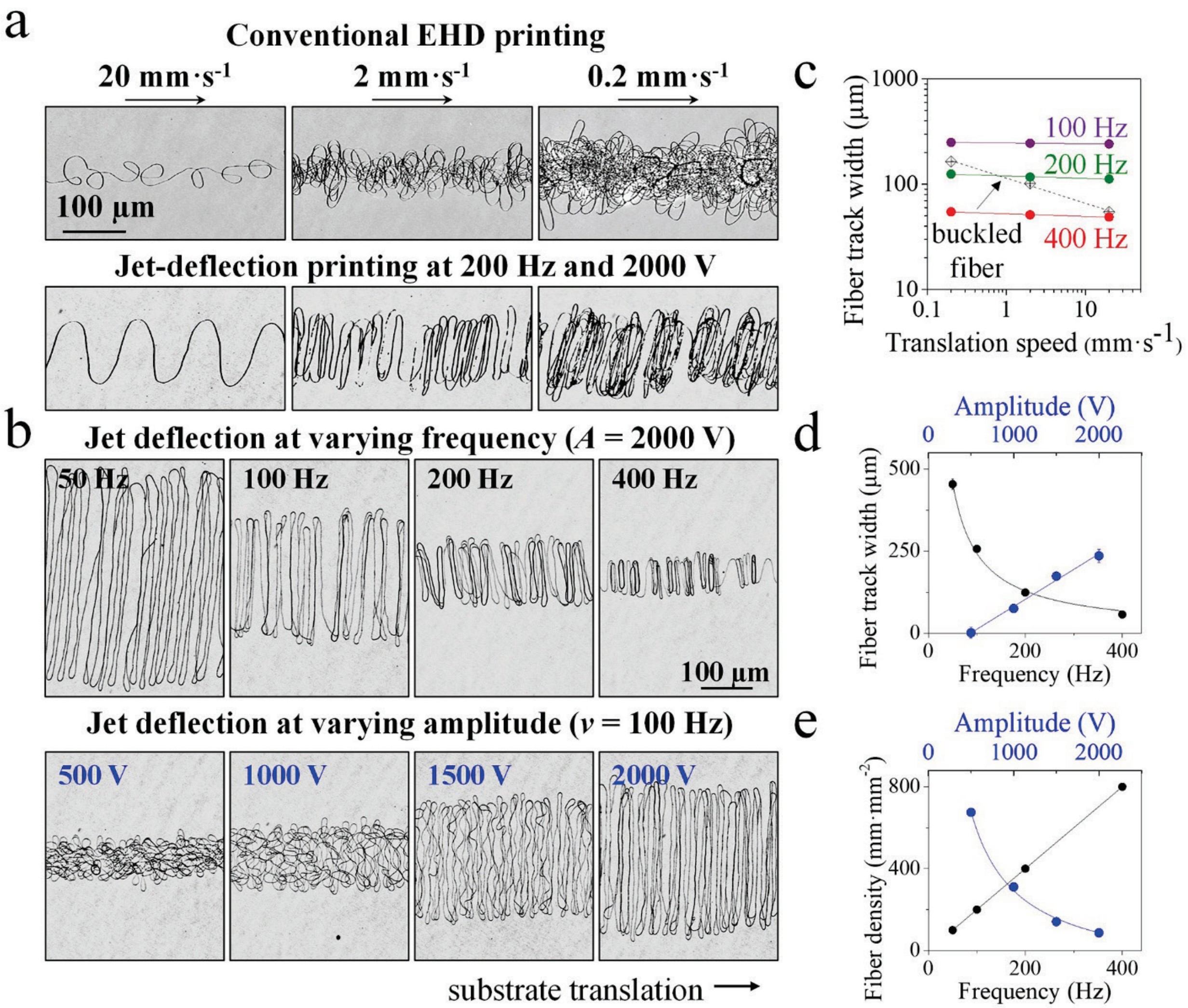

Figure 3.2. Fiber track width and density. a) Confocal microscopy images of the buckled (upper) and organized (lower) fiber tracks printed at translation speeds ranging from 20 to 0.2 mm·s^{-1} while fiber deposition speed was 40 mm·s^{-1} (as computed from organized fiber) via conventional (upper) and jet-deflection (lower) printing. In the lower images, organized fibers were deflected perpendicularly to the direction of the substrate translation. b) Confocal microscopy images of fiber tracks produced using jet deflection at increasingly higher signal frequency and amplitude. The jet speed was 59 mm·s^{-1} and the substrate translation speed 1 mm·s^{-1}. c) Dependence of the fiber track width on the substrate translation speed, while fibers are deposited via conventional and jet deflection printing (2000 V amplitude). d,e) Influence of the deflection frequency and amplitude on the fiber track width (d) and the fiber density expressed as mm of fiber length per mm^2 or fiber track area (e), both from the images shown in (b).

The control of the fiber alignment with electrostatic jet deflection also allows adjusting and quantifying the fiber density. The fiber density can be adjusted by changing the translation speed, which does not affect the track's width (as long as the electrodes control the jet positioning, Figure 3.2a), or the deflection frequency or the deflection amplitude, which do modify the width of the fiber track (Figure 3.2b,d,e). As shown in Figures 3.2e and 3.3, within a proper parameter range, the fiber density decreases in inverse proportion to the speed of the translation stage and to the deflection signal amplitude, and it increases linearly with the signal frequency.

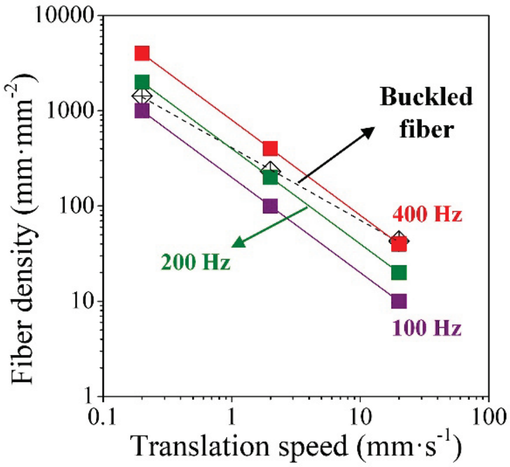

Figure 3.3. Effect of the substrate translation speed on the fiber density. a) Fiber density for tracks printed at different jet deflection frequencies while substrate translation speed changed from 20 mm·s^{-1} to 0.2 m·s^{-1}.

3.2. Effect of solvent evaporation on the morphology of the depositing fiber

In EHD jet printing using solvent-based inks, the evaporation of the solvent strongly affects the properties of the jet and plays an important role in the printing outcome. The solvent evaporation rate depends on multiple parameters, such as the ink composition, the equilibrium vapor pressure of the solvent, the ambient conditions and the diameter of the pendant drop (which mainly depends on the nozzle diameter and the infusion flow rate). The optimum solvent evaporation rate allows depositing dry fibers on the collector and avoids the excessive drying of the drop surface that may cause clogging of the nozzle. On the other hand, the wettability of the jet does not only affect the jet dynamics, but also the mechanical properties of the arriving fibers.

Figure 3.4 illustrates the differences between the patterning of fibers by wet and fast jets (left images) or dry and slow jets (right images) while squares and diamonds were printed. Small curvature radius resulted from a wet-arriving jet that allowed the jet to bend easily to reproduce the pattern geometry defined by the deflecting signal, while a big curvature radius resulted from a dry-arriving jet that could not bend easily and deteriorated the geometry of the printed pattern.

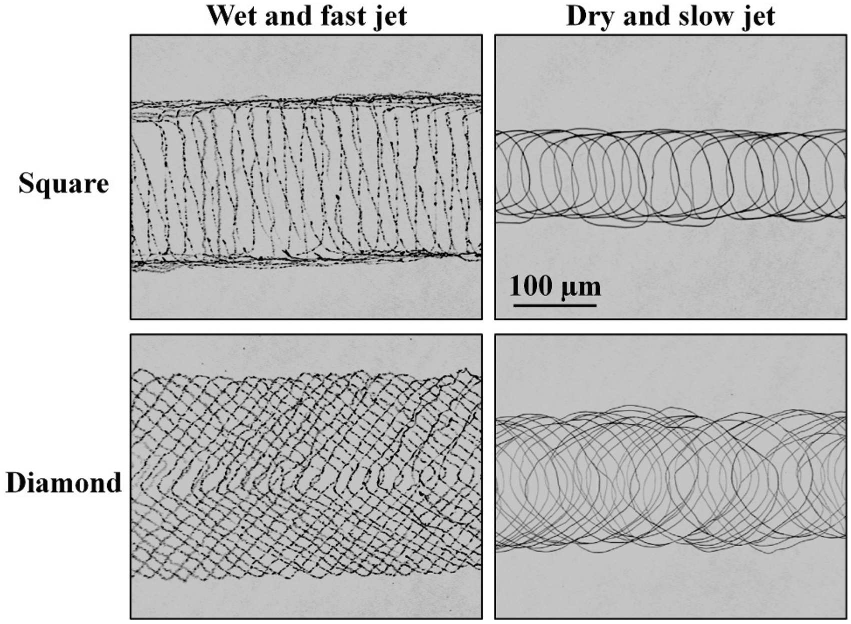

Figure 3.4. Dependence of the fiber patterning on the mechanical properties of the jet. Top and bottom images show squares and diamonds printed by wet (left) and dry (right) jets. The jet was deflected at the same signal amplitude (2000 V) and frequency (50 Hz) in both cases.

3.3. Fiber patterns

As displayed in Figure 3.5, the direction of the fiber alignment with respect to the fiber track can be tuned continuously. Deflecting the fiber orthogonally to the stage translation direction provides the widest tracks (Figure 3.5a, panel G). When the deflection angle coincides with the translation direction, the fiber self-assembles into a nanowall with an effective width approaching that of a single fiber (Figure 3.5a, panel A). In such 3D wall, the fiber is not completely horizontal but is printed with a small angle with respect to the substrate plane (Figure 3.5b,c). The length of such a nanowall is not limited by the distance the jet is deflected by during one oscillation period, but rather by the preset translation of the substrate relative to the nozzle.

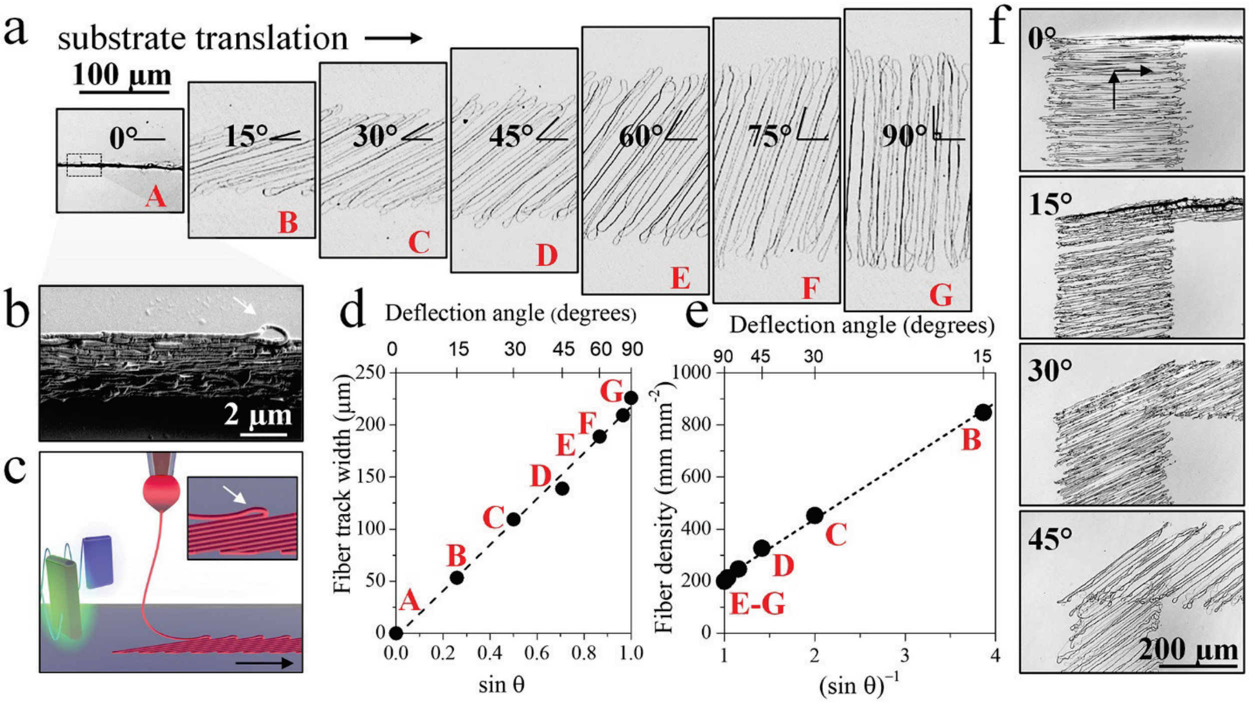

Figure 3.5. Controlling the track width and fiber density by changing the deflection angle. a) Confocal microscopy images of fiber tracks printed at increasing deflection angle as the substrate translates sideways. b) Scanning electron microscopy (SEM) image of a fiber assembled into a wall with high aspect ratio and submicron width, for panel A in (a). c) Scheme of the mechanism of printing of a wall longer than the fiber deflection length. The white arrows plotted in (b,c) point at a fiber loop. d) Dependence of the fiber track width on the deflection angle relative to the translation direction. The plotted line shows the linear fit of the data points with the sinus of the deflection angle (θ). e) Dependence of the fiber density on the deflection angle relative to the stage translation direction. The plotted line shows the linear fit of the data points with the inverse of the sinus of θ. f) Confocal microscopy images of fiber tracks with a corner where the track width changes with the stage translation direction in a magnitude depending on the deflection direction. Black arrows indicate the stage path.

At fixed stage translation speed, deflection frequency and amplitude, the track width linearly correlates with the sinus of the deflection angle (Figure 3.5d). At the same time, the fiber density increases with the decrease of the deflection angle, being inversely proportional to its sinus (Figure 3.5e). It reaches the highest value when the deflection angle is zero, which is when the fiber is deflected in the direction of the stage translation. Additionally, the fiber density is expected to change also when changing the stage translation direction, as shown in Figure 3.5f.

Beyond simple 1D deflection, more complex fiber patterns can be produced by independently controlling the voltage at the deflection electrodes to produce complex motifs. Figure 3.6 displays several examples of fiber patterns with different geometries and fiber density.

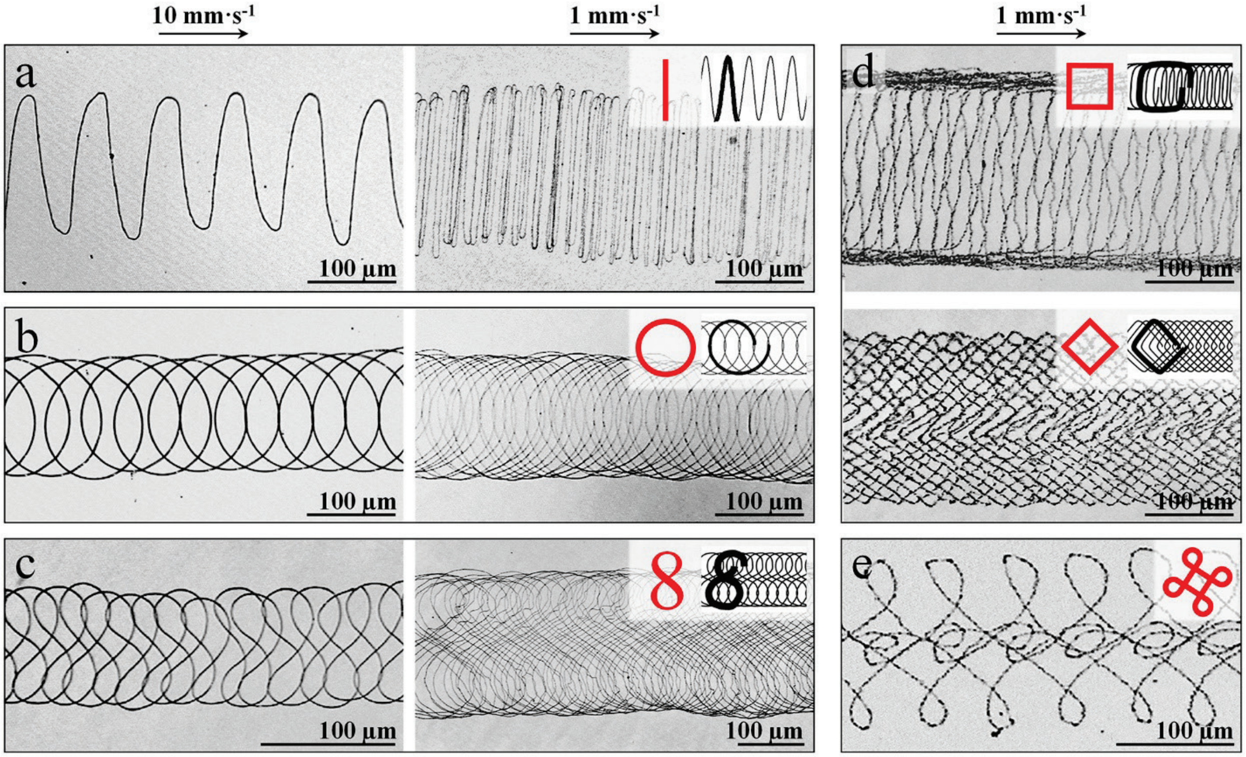

Figure 3.6. Fiber tracks printed by deflecting the jet to follow various motifs (colored in red). Confocal microscopy images of the tracks printed with the following motifs: line (a), circle (b), figure of eight (c), square (d, top), diamond (d, bottom), and 4-loop pattern (e). Insets display a scheme of the printed pattern. Panels a-c display the track printed at two different stage translation speeds (left: 10 mm·s^{-1}; right: 1 mm·s^{-1}) but constant jet-deflecting amplitude (2000 V) and frequency (200 Hz). Panels d-e were printed at constant stage translation speed and jet deflecting conditions (amplitude 2000 V, frequency 50 Hz).

The deflection motif was defined and reproduced using the LabVIEW software for generating deflection signals, and the size of the printed motif depends on the jet speed, motif geometry and the motif repetition frequency and amplitude of the deflection signal. For each pattern, the fiber density was varied via the substrate translation speed, as shown by the left and right panels in Figure 3.6a-c. Depending on the motif, the fiber directionality and density can either be even throughout most of the fiber track (e.g. Figure 3.6a) or uneven (Figure 3.6d, top).

Even more complex track patterns can be achieved by modulating the deflection parameters as the track is being printed. Figure 3.7a,b displays tracks printed while the deflection motif (line) is continuously rotated. The difference between the patterns printed in Figure 3.7a and 3.7b is the ratio between the motif rotation rate and the stage translation speed. Notice that the motif size in these patterns was not changed along the track length, but only the deflection angle was tuned. Figure 3.7c,d shows the fiber tracks obtained when the deflection angle was abruptly and cyclically modified by 90 ° and 45 °, respectively. In contrast, Figure 3.7e,f displays images of patterns obtained at a constant deflection angle but changing the deflection frequency along the track. By cycling the value of the deflection frequency, the track width is smoothly modified while printing the same fiber length per unit length, and changing the fiber density as a consequence. Notice that, in these examples, the deflection amplitude is constant, and the track width is determined by the available fiber length per unit time (which maintains constant since the jet speed remains constant as well) while the frequency is being modified. As displayed in Figure 3.7g-i, it is also possible to modify the track center position by changing the bias voltage at the jet deflection electrodes while the stage is translated. This change can be either continuous, as in Figure 3.7g,h, or abrupt, as in Figure 3.7i. Besides, different parameters can be simultaneously adjusted to obtain a virtually unlimited range of patterns. As an example, an abrupt change in frequency is paired with a change of the center position in Figure 3.7j. Such complex transitions in jet deflection enable the printing of fast fibers into tracks with highly controlled and custom-designed anisotropic properties that fit the requirements of each application field.

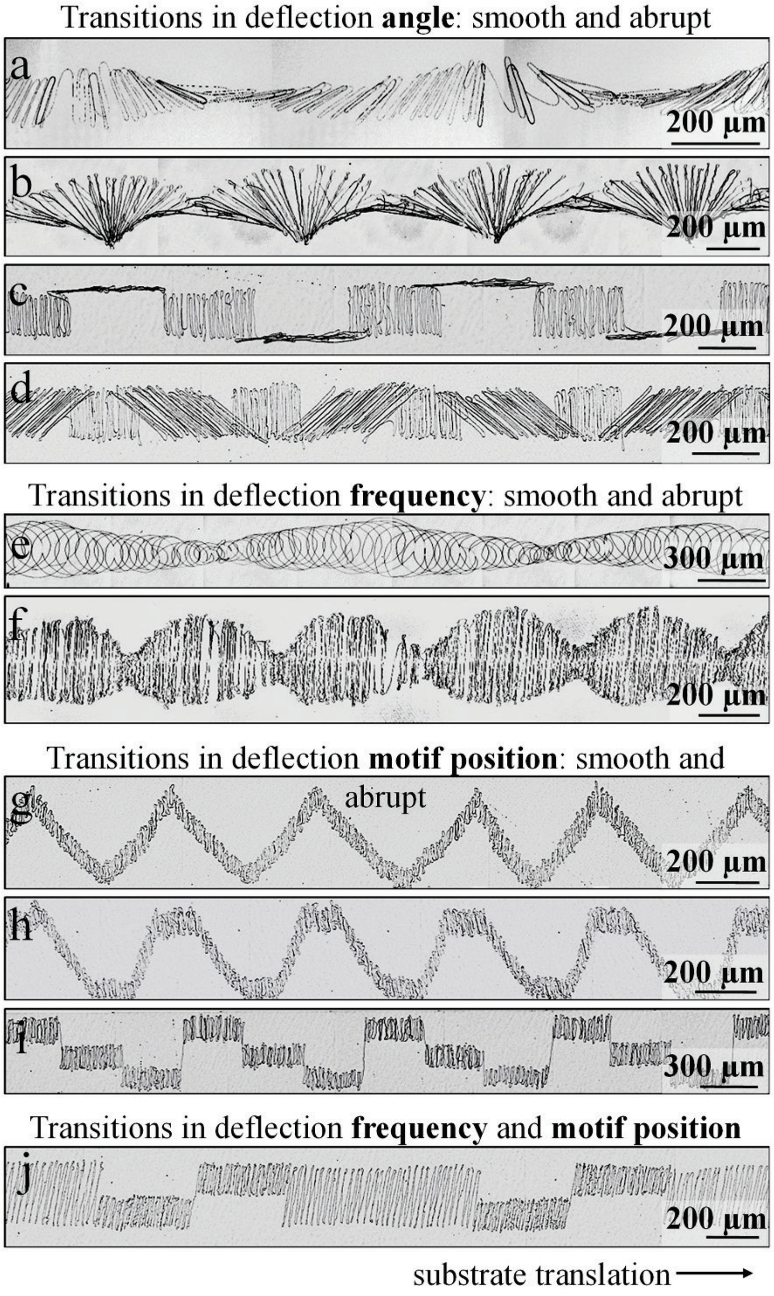
Transitions in deflection angle: smooth and abrupt
a
200 µm
b
200 µm
c
200 µm
d
200 µm
Transitions in deflection frequency: smooth and abrupt
e
300 µm
f
200 µm
Transitions in deflection motif position: smooth and abrupt
g
200 µm
h
200 µm
i
300 µm
Transitions in deflection frequency and motif position
j
200 µm
substrate translation

Figure 3.7. Modifying the jet deflection parameters along the track. Confocal microscopy images of fiber tracks obtained by cycling the jet deflection parameters: a,b) Continuous change of the deflection angle with a deflection frequency of 200 Hz and a translation speed of 4 mm·s^{-1} (a) and 2 mm·s^{-1} (b). c,d) Abrupt change of the deflection angle by 90 ° and 45 °. e,f) Smooth threefold change of the deflection frequency using a circle and line motif. g,h) Continuous change of the center position. i) Abrupt change of the center position. j) Abrupt x2 increase in frequency paired with controlled fiber positioning. All patterns were produced by slowly translating the substrate as shown, while fiber patterning was achieved solely by jet deflection.

3.4. Towards applications: accurate fiber patterning with anisotropic properties

Figure 3.8 displays confocal images of interdigitated electrodes printed without (Figure 3.8a) and with (Figure 3.8b) the aid of the electrostatic jet deflection. The electrical conductivity of a track will depend on the amount and orientation of the constituent fiber. In addition, the smallest attainable size of an interdigitated microelectrode depends on the smallest attainable width of the printed tracks. In conventional EHD printing, buckled fiber is randomly deposited, which limits the control on the track width and the narrowest track that can be printed (Figure 3.8a). On the other hand, the electrostatic deflection of the jet enables the printing of the same length of fiber into well-defined tracks with preset width and density of aligned fiber (Figure 3.8b), allowing even the printing of thin nanowalls with widths approaching the width of a single nanofiber (Figure 3.5b). The electrostatic deflection of the jet enables to control the anisotropy of the track's properties, such as optical, electrical, magnetic, wettability, cell guidance, etc. As a demonstration, Figure 3.8c,d displays optical images of the IREC logo printed with buckled fiber and aligned fiber. The logo was imaged from the top under oblique illumination from one side, while being rotated 360 º to observe the change in their brightness. The random fiber track (Figure 3.8c) is not sensitive to the illumination direction, showing a constant brightness, as expected from its isotropic fiber deposition. In contrast, the logo containing the aligned fiber track (Figure 3.8d) displays a much higher brightness when illuminated at an angle that is orthogonal to the fiber alignment direction, almost completely disappearing when illuminated along the fiber orientation. Figure 3.8e displays the Chinese greeting Ni Hao (你好) printed by the ancient art of calligraphy, mimicking its masterful handwriting with jet deflection, i.e. producing fiber tracks of variable width depending on the writing direction.

Successful implementation of the developed patterning technique toward applications will require the use of materials with tailored properties. As the focus of the present work is on devising a method to control the alignment of nanofibers, for simplicity we used only a PEO solution as a current gold standard for the EHD jet printing. However, due to the effective decoupling of the EHD jetting and jet-deflecting approach, this strategy should be applicable to any composition already shown to support stable EHD jetting[88].

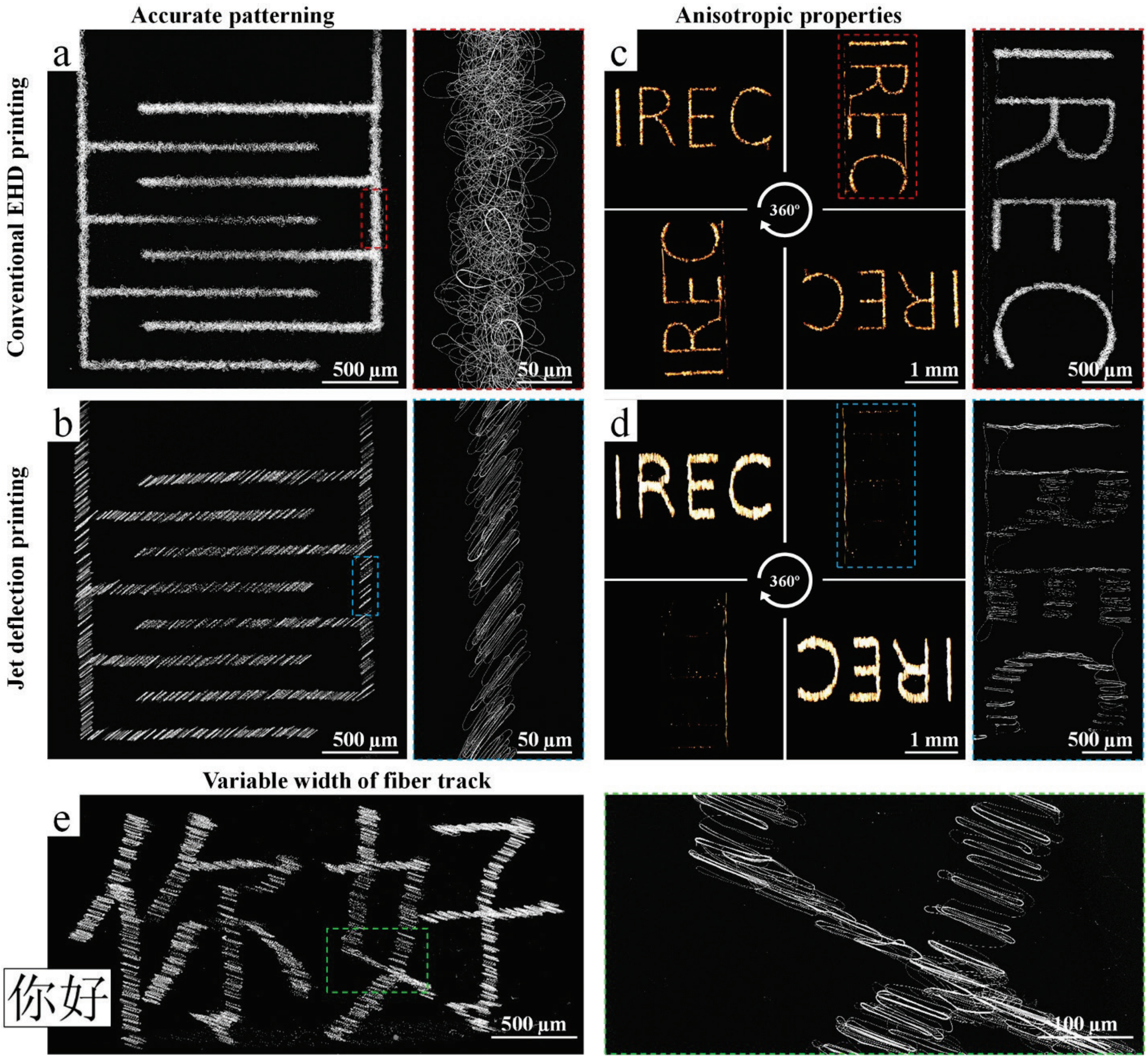
Accurate patterning
Anisotropic properties
a
Conventional EHD printing
500 µm
50 µm
c
IREC
360°
1 mm
500 µm
b
Jet deflection printing
500 µm
50 µm
d
IREC
360°
1 mm
500 µm
Variable width of fiber track
e
你好
500 µm
100 µm

Figure 3.8. Toward applications. a,b) SEM images of interdigitated microelectrodes printed with buckled fiber (a) and aligned fiber (b). The jet deflection has a potential to reduce track width and increase fiber density, thus allowing decreasing electrode's footprint or enhance its performance. c,d) Optical images (left) of IREC logo printed with buckled (c) and aligned (d) fiber, viewed under oblique illumination as the patterns are rotated 360 º, and SEM images of the same logos (right). In contrast with the logo made of buckled fiber, the logo made of aligned fiber shows an anisotropic light scattering, resulting in high brightness when fibers are perpendicular to the light source and disappearing when parallel to it. e) SEM image of a printed pattern of the Chinese greeting 你好 (Ni Hao).

Chapter 4

Matching the jet speed with the printing speed

Printing with high fidelity requires matching the jet arrival speed with the printing speed, and electrostatic jet deflection facilitates this condition. On the one hand, the printing speed is defined by the deflecting parameters (that is the amplitude and frequency of the deflecting signal). On the other hand, as the printing speed is known, the jet speed can be computed experimentally by measuring the size of the printed patterns, allowing the use of inexpensive optical equipment to determine in situ the jet speed.

Therefore, the main goal of this chapter is to show how the jet speed can be estimated when 2D patterns or 3D structures are printed. Additionally, this chapter illustrates the effect of the jet-deflecting signal parameters on the printing speed and the deposited patterns. All together will help us to establish a procedure to measure the jet speed easily, which should match later with the printing speed to provide prints with the best quality.

4.1. Determining the jet speed from 2D patterns

In the conventional EHD jet printing method, the stage is translated at increasing speeds, from a value lower than the jet speed, until the *matched speed regime* is found (Scheme 4.1). At the lower stage speeds, the jet buckles onto the substrate due to the fiber length produced is larger than the fiber length needed, printing loops with random shapes as a result. The amplitude of the loops reduces at increasing the stage translation speed, eventually changing to a serpentine pattern made of meanders whose amplitude decreases as the stage speed keeps increasing. Eventually, a straight fiber forms when the stage speed matches or exceeds the jet speed (Figure 4.1a, bottom panel). In this last case, the jet is stretched by tension transferred from the contact point of the jet with the substrate.

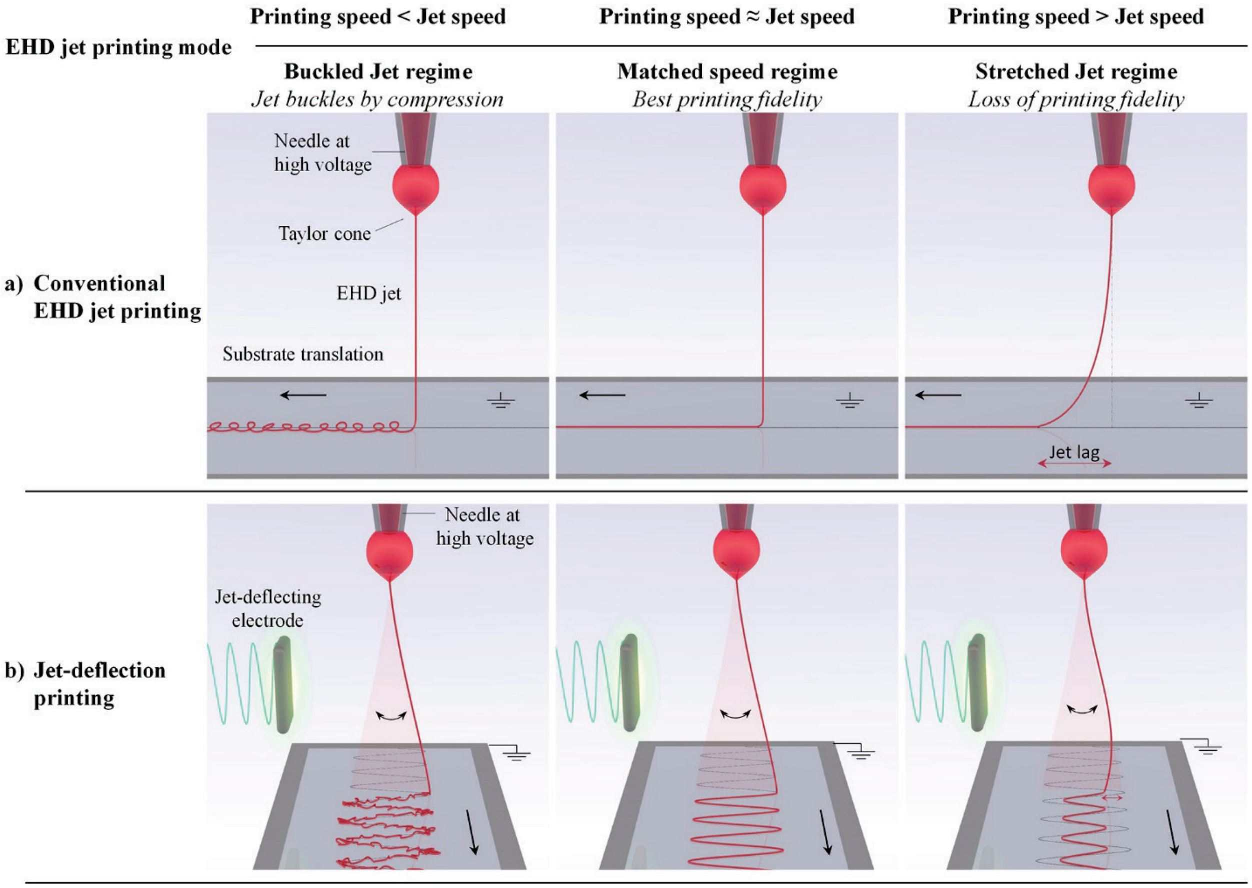
EHD jet printing mode
Printing speed < Jet speed
Printing speed ≈ Jet speed
Printing speed > Jet speed
Buckled Jet regime
Jet buckles by compression
Matched speed regime
Best printing fidelity
Stretched Jet regime
Loss of printing fidelity
a) Conventional EHD jet printing
Needle at high voltage
Taylor cone
EHD jet
Substrate translation
Jet lag
b) Jet-deflection printing
Needle at high voltage
Jet-deflecting electrode

Scheme 4.1. Classification of printing regimes of EHD jet-based printing. a) Conventional EHD jet printing. b) Electrostatic jet deflection printing.

Conventional method to analyze the jet speed by increasing the stage translation speed are based on searching for the critical condition at which the jet first becomes straight. Unfortunately, a straight jet is still obtained when the jet speed is exceeded by the stage speed. Therefore, increasing the accuracy of the jet speed determination is difficult. Another disadvantage of this method is that a fast (and fast-accelerating) stage is needed (at least as fast as the jet), where this could be a challenge because EHD jets can attain speeds well in excess of 1 $m \cdot s^{-1}$. In addition, a powerful microscope is needed to precisely resolve the position of a single fiber on the printed substrate, enough to distinguish a perfectly straight fiber from meandering fibers with a low amplitude. Because of these shortcomings, the in-line implementation of the conventional method seems exceedingly complex.

We propose a new approach based on analyzing printed patterns obtained with substrate translation while periodically deflecting the jet transversely to the stage translation direction in order to print a repeating pattern or motif (Figure 4.1b). As explained in Chapter 2, the jet speed is determined by dividing the length of fiber L printed in one period of jet deflection by one period T (the inverse of the frequency v of the jet deflecting signals). This determination does not require a fast stage and is nearly independent of stage speed. As the substrate speed increases from a low value, the pattern's amplitude decreases while its wavelength increases (Figure 4.1b, panels A through F). When the substrate speed exceeds the jet speed, the fiber becomes straight (Figure 4.1b, panel G), just as in the conventional method. The key advantage of this method lies in the fact that all of the generated patterns shown in Figure 4.1b except panel G can be used to compute the jet speed from the known geometry of the printed pattern. The jet speeds computed from the panels in Figure 4.1b are shown in Figure 4.1c. The consistency of the jet speed data determined at different stage speeds proves that the stage motion did not impart speed to the fiber.

The proposed jet deflection approach overcomes the above-mentioned difficulties of the conventional methods, as it requires neither matching speeds nor resolving individual fibers (nor having a fast stage). In fact, the proposed method works better at low stage speeds, where the accuracy on the track's width will be better. In addition, a single pass suffices in the new approach, in contrast to the conventional method, where many passes are needed to find the critical *matched speed regime* condition. Finally, the required stage travel is much smaller in our method as the stage can be moved much slower than the jet. In the conventional method, the substrate may need to travel several millimeters or more, while accelerating up to the jet speed, and then decelerate back to zero. For instance, for an acceleration of 20 – 30 $m \cdot s^{-2}$ typical of a high-performance stage, reaching 0.5 $m \cdot s^{-1}$ would require acceleration/deceleration travel of at least 4 – 6 mm, giving a total travel of at least 20 mm.

Finally, note that in panel B of Figure 4.1b the fiber is more regularly distributed than in panel A, where the density of fibers is less homogeneous. This happens by the tendency of the fibers to fall on top of previously deposited ones due to electrostatic attraction. Such attraction is the result of the charge reversal taking place after deposition caused by electrostatic induction[34,89]. This phenomenon has no impact on the determination of speed, because the width of the track is not affected.

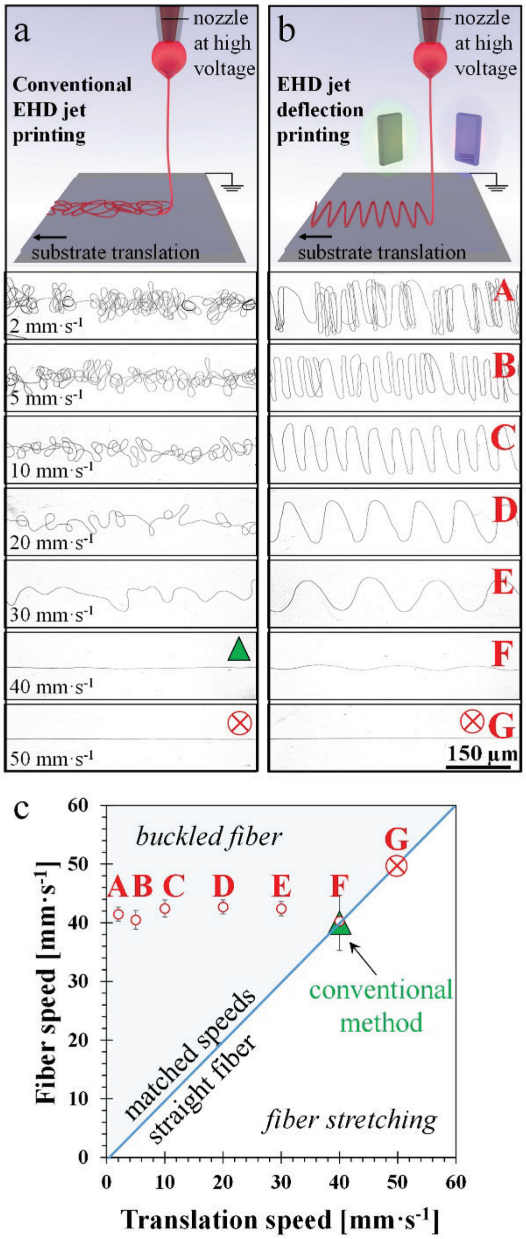

Figure 4.1. Comparison of conventional and jet-deflection printing for determining the fiber speed. a) Conventional EHD jet printing: Schematic and SEM images of a PEO fiber collected at different substrate speeds. The stage speed matches the jet speed when straight fiber is printed. b) Jet-deflecting printing: The jet is electrostatically deflected perpendicularly to the substrate translation at 200 Hz with 1200 V signal amplitude. The jet speed is determined from the width of the printed pattern at any stage speed. c) Jet speed determined by the conventional method (green triangle) and by the jet-deflection method (circles). Error bars are obtained from the standard deviation computed from 3 to 5 data points for each translation speed. Ink composition: 7 wt% PEO 0.3 MDa in 1:1 wt. H_2O:EtOH. Syringe pump rate: 70 nL·min^{-1}. Stainless needle with blunt end used as nozzle (127 µm ID). Nozzle voltage was set at 1500 – 2000 V. SEM images obtained using in-lens detector and shown in negative for better contrast.

4.2. Jet deflection strategy based on 3D structures

The idea for obtaining the jet speed from a printed track and a jet deflection signal of known frequency can be extended to the case where 3D structures are printed by periodically stacking layers of fibers. Electrostatic charge dissipation and charge reversal here become key in promoting the precise self-assembly of the fibers. The XY translation stage is stationary during the printing of each object, moving only from object to object. Figure 4.2 shows several examples of 3D printed structures: (a-c) straight walls made with PEO fiber, (d-e) cylinders made of a PEO-Ag NPs composite, and more complex patterns, such as boxed scaffolds (f), triplets (g-h), flowers (i), as well as interdigitated (j) and single (k) microelectrodes. Some images are shown as SEM micrographs (panels b, c, e), but their widths are large enough to be resolved optically (600 μm for the walls and 8 μm for the cylinder). As an example, Figure 4.2d shows an optical photo of a 29 μm wide cylinder.

The jet speed is computed for a 3D object much like for a 2D object: the product of fiber length L printed in one period times the frequency ν of the jet-deflecting signal. For the case of walls (Figure 4.2a-c), two layers of fiber are deposited per period (20 ms). Therefore, the jet speed equals twice the wall length (0.6 mm) times the frequency of the jet-deflecting signal (50 Hz), namely 60 mm·s^{-1}. For the case of the cylinder in Figure 4.2e, the jet speed is equal to the diameter (0.008 mm) times π and times the frequency of the jet-deflecting signal (100 Hz), namely 2.5 mm·s^{-1}. Note that neither the object's height nor the number of fiber layers (up to 150 in the case of the walls) are used in the computation.

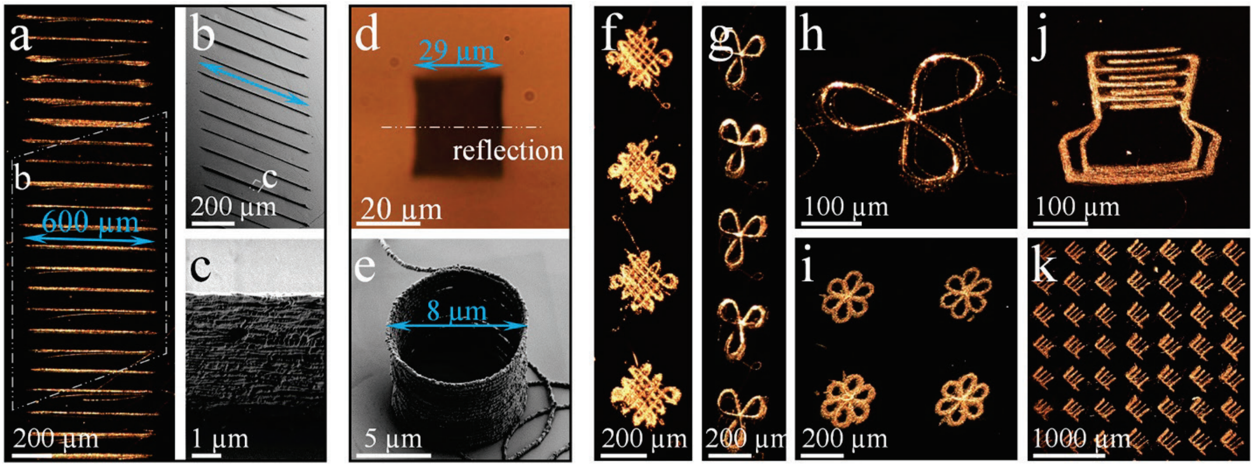

Figure 4.2. Jet speed determination from the size of printed structures. Optical images (a, d, f-k) and SEM micrographs (b, c, e) of 3D printed structures on still Si wafer substrates by EHD jet-deflection, and which can be used for determining the jet speed. SEM micrographs were taken by means of tilting the sample 45º. a-c) Straight walls with 50, 100, and 150 layers, printed by a 60 mm·s^{-1} jet using 50 Hz sawtooth signals (150 layers for (c)); d-e) cylindrical structures of PEO and 50 nm Ag NPs, where d) shows a 100-layer cylinder printed at 200 Hz (Oblique view) and at 18.2 mm·s^{-1} jet speed, and e) a 25-layer cylinder printed at 100 Hz and 2.5 mm·s^{-1} jet speed; f-k) Complex patterns: boxed scaffolds (f), triplets (g-h), flowers (i), interdigitated electrodes (j) and separate electrodes (k), with jet-deflecting frequency at 12.5 Hz (j), 50 Hz (f, i, k), and 100 Hz (g, h). Inks used: 8 wt% PEO 0.3 MDa in 4:1 wt. H_2O:EG for (a-c) and (j), while 5 wt% Ag NPs in 4.75 wt% PEO 0.3 MDa in 1:3 wt. H_2O:EtOH was used for the rest. Glass tips were used (200 µm ID) as nozzle in all cases. Dry nitrogen was supplied around the nozzle for (d-e). Nozzle voltage ranged between 800 and 1200 V, and nozzle to collector distance was 3 mm.

4.3. Influence of the jet deflection parameters on the printing speed

The jet deflection parameters, *i.e.* the jet-deflecting amplitude and frequency, define the printing speed that should match with the jet speed to provide the best quality prints. Therefore, it is important to understand how they affect the jet speed.

Figure 4.3a shows how the width of a 2D track varies with the jet deflection signal amplitude at constant frequency, on an EHD jet moving at 140 mm·s^{-1} towards the collection substrate. At low printing speeds, which are defined by the signal amplitude and frequency, the jet buckles over the collector, and the width of the fiber track, shown in Figure 4.3b, increases linearly with amplitude (cases A through F). This corresponds to the *buckled jet regime* in Scheme 4.1b.

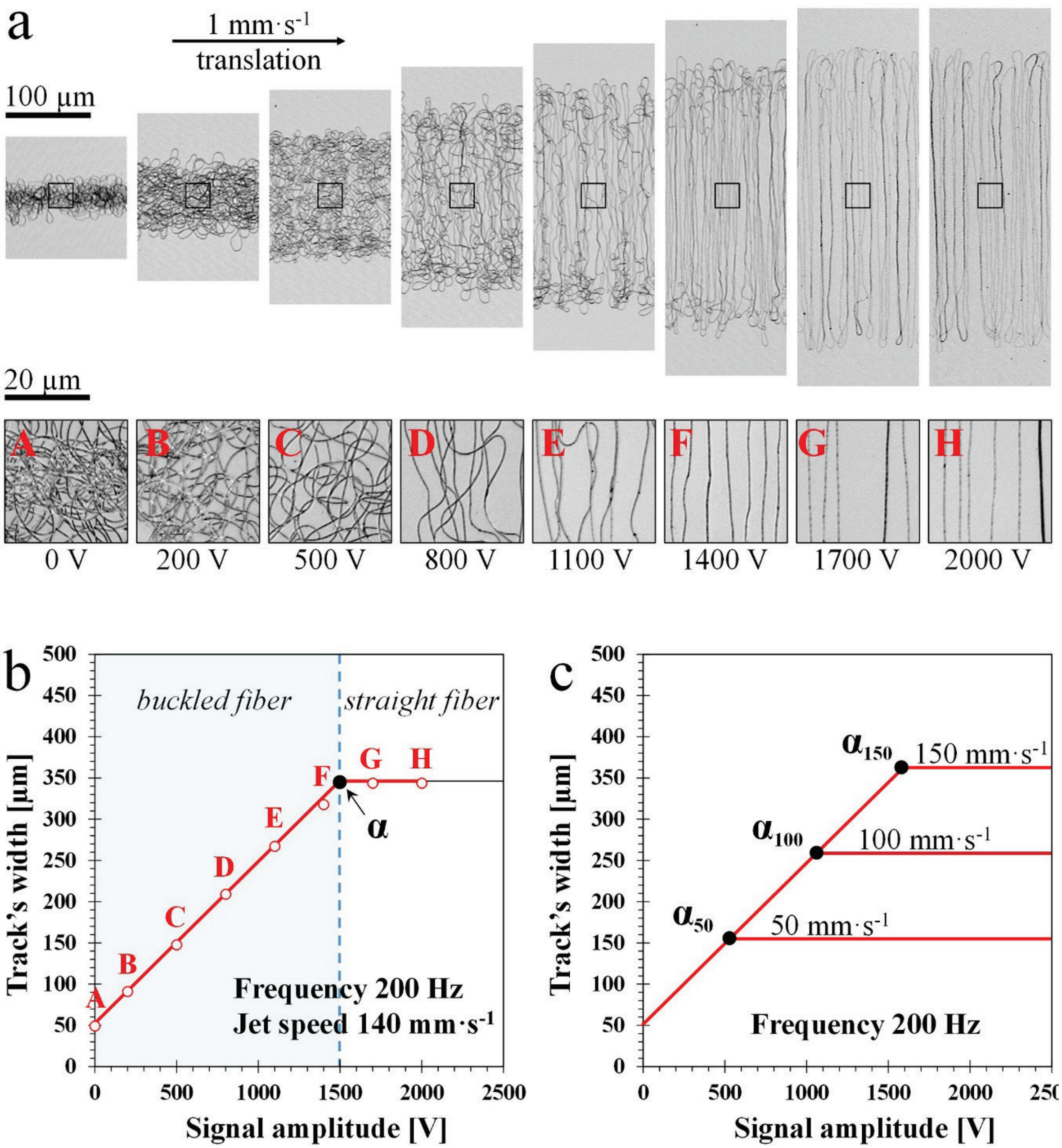

Figure 4.3. Effect of the jet-deflecting signal amplitude on the width of a 2D pattern printed on a slow-moving substrate. a) Confocal microscopy images of PEO fiber collected as the substrate moves at 1 mm·s^{-1} and the jet is deflected in the perpendicular direction with a sawtooth wave at 200 Hz, for different amplitudes of the jet-deflecting signal. b) Dependence of the width of the printed fiber track on the signal amplitude at constant frequency, covering the different printing regimes. Buckled fiber is collected in the blue shaded zone, where the jet speed cannot be determined by the proposed method. c) Printed track's width versus signal amplitude extrapolated from panel (b) at different fiber speeds. Ink composition: 3 wt% PEO 1 MDa in 1:1 wt. H_2O:EtOH. Syringe pump rate: 70 nL·min^{-1}. Glass tip nozzle at 950 – 1100 V. Dry nitrogen gas was supplied around the jet.

Eventually, a critical condition is reached, represented on this graph as α, for which the printed fiber is aligned, corresponding to the *matched speed regime* in Scheme 4.1b. As the signal amplitude increases beyond that for the critical condition, the fiber remains aligned, while track's width remains constant (cases G and H). This corresponds to the *stretched jet regime* in Scheme 4.1b. The constancy in pattern width arises probably because, beyond condition α, the jet resists stretching as the electrical force acting on the jet due to the jet deflection signal is mostly transverse to the jet, becoming unable to develop any significant mechanical tension along the jet. Conceivably, an ink could be soft enough to yield under this electrical force, in which case the track's width would be expected to increase after point α. Still, the critical condition would probably be detectable in the plot of the track's width versus amplitude by a change (decrease) in slope after α. Figure 4.3c illustrates how, at this signal frequency, the pattern width is expected to vary with the signal amplitude for different jet speeds. The sloped part of the curves, which corresponds to buckled fiber, is the same up to each critical point, which is attained at larger amplitudes for larger jet speeds.

Figure 4.4 shows the role played by the frequency of the jet-deflecting signal, while keeping constant amplitude. When the frequency is low enough, the jet undergoes buckling, at condition A (50 Hz). As the frequency is raised, the extent of the buckling is reduced. Eventually, jet buckling disappears as the printed fiber becomes straight at the critical condition α, reached between conditions A and B in Figure 4.4b, and which corresponds to the *matched speed regime* (Scheme 4.1b). Beyond this condition, in the *stretched jet regime* showed in Scheme 4.1b, the track's width decreases with increasing frequency (conditions B-E), as imposed by mass conservation. Indeed, assuming a constant diameter fiber, the simple inverse dependence $W = \frac{U_J}{2 \cdot \nu}$ fits the data well (Figure 4.4b), where W is the fiber track width. The good agreement between theory and experiment suggests that the jet deflection did not cause fiber stretching (as concluded in Figure 4.3b by a different argument).

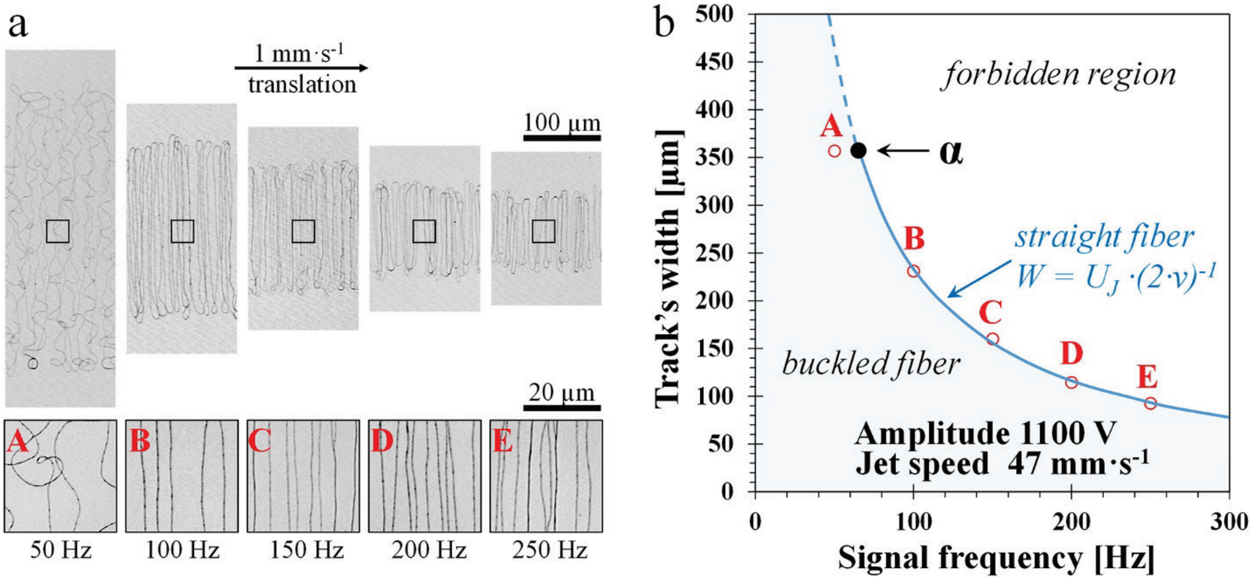

Figure 4.4. Effect of the frequency (ν) of the jet-deflecting signal on the width (W) of a printed pattern on a slow-moving substrate. a) Confocal microscopy images of the PEO fiber collected while the substrate is moved at 1 mm·s^{-1} and the jet is deflected perpendicularly by a sawtooth signal for different frequencies of the jet-deflecting signal at fixed amplitude (1100 V). b) Width of the printed fiber track versus frequency. The blue shaded area displays the region where the jet buckles and jet speed cannot be determined by the proposed method. Ink composition: 3 wt% PEO 1 MDa in 1:1 wt. H_2O:EtOH. Syringe pump rate: 70 nL·min^{-1}. Glass tip nozzle at 950 – 1100 V. Dry nitrogen gas was supplied around the jet.

4.4. Case study: Jet speed determination using 2D tracks in the presence of jet instabilities

The approach for determining jet speed was applied to detect instabilities in the EHD jetting causing jet speed pulsing or movement of jet ejection point. Figure 4.5 displays two different situations, showing for each confocal microscopy images of 2D printed tracks and graphs of the corresponding jet speed, as obtained by our method, and the centerline position of the printed fiber track. In both cases, the track's width can be easily converted to jet speed, as twice the track's width times the jet deflection frequency ($U_J = 2 \cdot W \cdot \nu$). In Figure 4.5a, the changing width of the track reflects a beating in the jet speed of about 1.2 Hz, while the jet is deflected at a much faster frequency (500 Hz). Figure 4.5b shows a case in which a correlation exists between the centerline position of the printed pattern and its width, thus the jet-speed.

This is the result of a beating of the jet ejection point as shown in images of the ink drop in Figure 4.5d, indicated by red and yellow arrows. In the case of Figure 4.5a, for which the centerline position remained constant in time, the point of jet ejection on the drop did not beat, as demonstrated in Figure 4.5c. The process of detecting the two types of jet instability shown in Figure 4.5 can also be automated using in situ inspection equipment and image recognition software, and then be used for ensuring stable jetting conditions while printing.

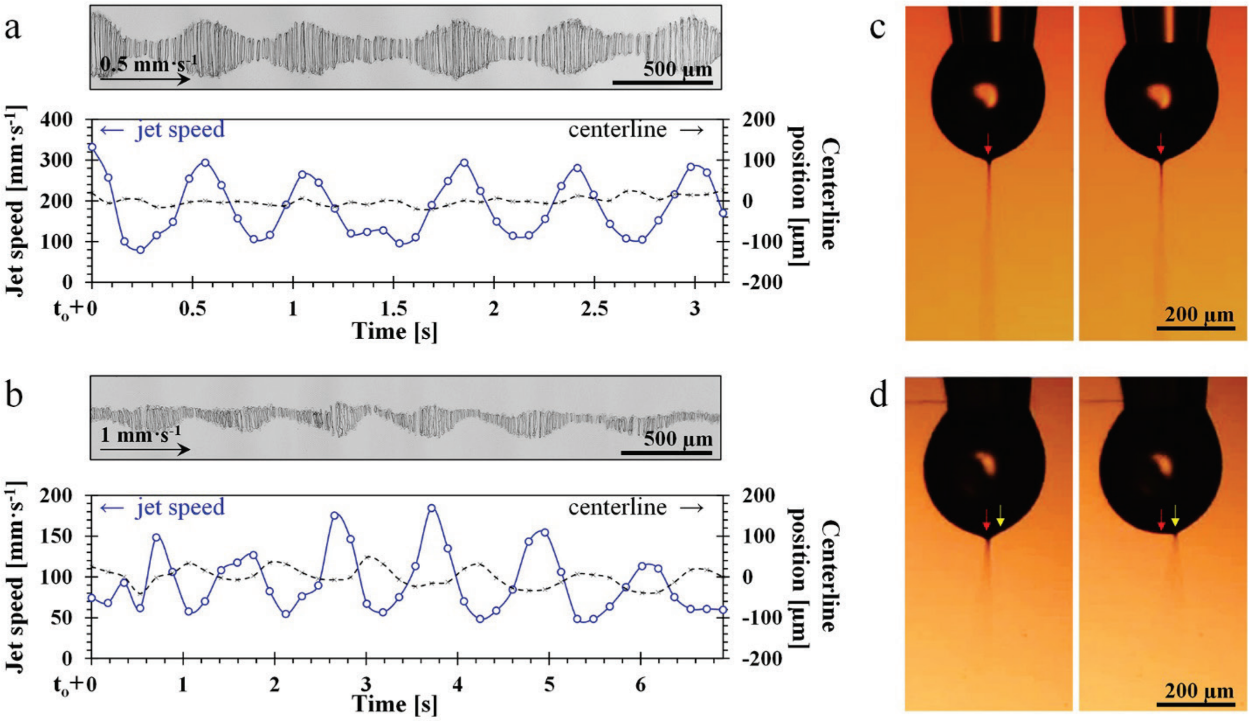

Figure 4.5. Detection of the jet speed instabilities. Jet instabilities occurred during PEO fiber collection on a moving substrate, while the jet was deflected in the perpendicular direction with a sawtooth signal at 500 Hz and 2000 V amplitude. a-b) Confocal image of the fiber track and plot of the jet speed and track's centerline position for (a) jet with pulsating speed, and (b) jet pulsation with displacement of the jet on the pendant drop. c-d) Optical images of the pendant drop with EHD jet during printing corresponding to cases shown on (a-b), respectively. Arrows indicate the point of jet ejection. Nozzle voltage: 1000 V. Ink composition: 3 wt% PEO (1 MDa) in 1:1 wt. H_2O:EtOH. Syringe pump rate: 50 nL·min^{-1}. Dry nitrogen gas was supplied around the jet.

4.5. Practical application

Before starting the printing process or when changing a parameter of the system, the speed of the jet generated from the specifically used ink, printing parameters, and environmental conditions need to be determined to adapt the printing speed by adjusting the movement of the stage (when a stage is used to create a pattern) or the jet deflection signal (when jet deflection is used). Once the printing process has started, the in situ and in line measurement of the jet speed can be used for a better control of the EHD printing process, enabling additional adjustment of the dimensions of the printed object, and detecting and compensating for instabilities in the printing system, the ink, or the environment.

By way of example, Figure 4.6a shows a pair of interdigitated electrodes produced using the stage movement to define the electrode shape and jet deflection to adjust the width of the electrode arms. The jet speed during the printing of this electrode was 170 mm·s^{-1}. The EHD printing parameters and thus the jet speed can be intentionally modified during the printing process to produce electrodes with different size and geometry, but also with different arm width, different electrode microstructure, amount of material deposited, and thickness of the deposited fiber. Besides, the printing speed could be maximized considering the size and precision required for the object to be printed to minimize production time. The minimum time required to print each object, and also the printing precision and repeatability, depend on the jet speed.

It could be of interest to print objects of different sizes in the same process or objects with features that require different printing precision. Conveniently, this jet speed can be rapidly adjusted by just modifying the nozzle voltage. However, owing to the complex interrelation between the several parameters influencing it, the easiest and most precise strategy to match continuously jet and printing speeds is to measure continuously the jet speed to adjust later the printing speed. On the other hand, during the printing process, the speed of the jet can be also unintentionally changed due to variations in the process or environmental parameters, *e.g.* a change in ambient temperature or humidity. When the jet speed is measured in situ, this information can be used as feedback for the real-time adjustment of the printing parameters to correct the jet speed or for the real-time adjustment of the printing speed, defined by the movement of the stage (in stage-driven printing) or the frequency of the jet deflection (in jet-deflection printing), to compensate for the change of external parameters.

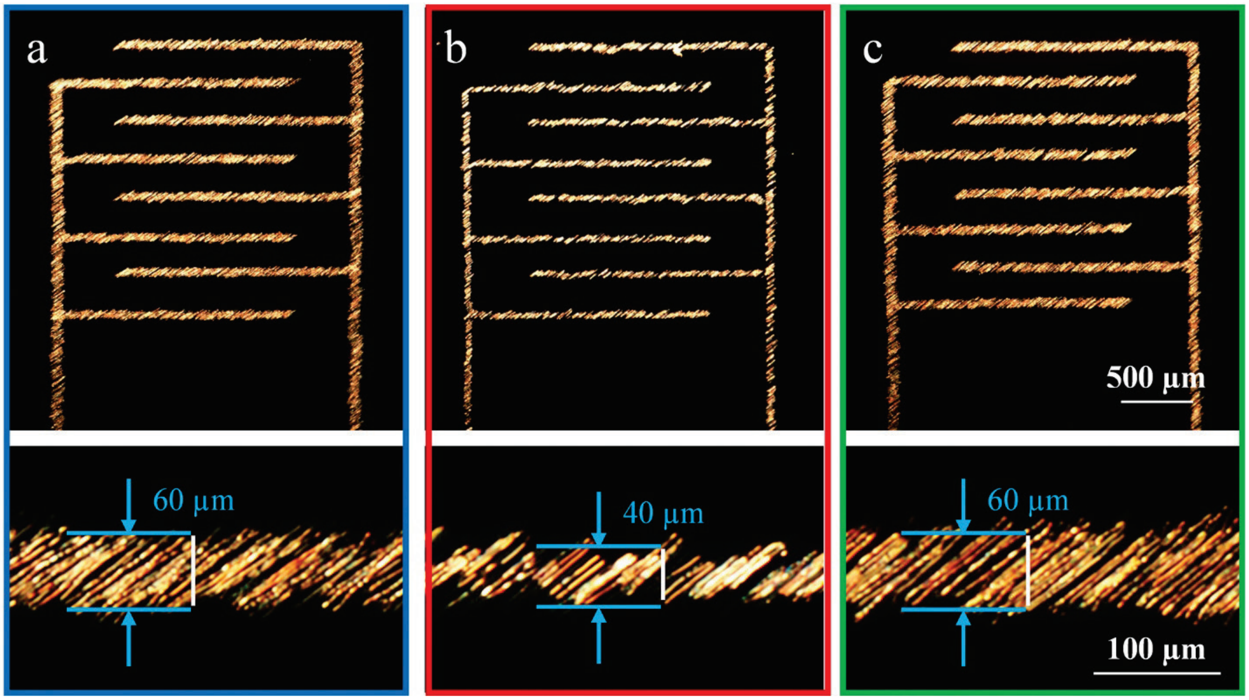

Figure 4.6. Interdigitated electrodes printed using the XY stage translation to define their geometry and jet deflection to define their arm width. a) Electrodes printed using a nozzle voltage V_N = 700 V, a jet speed U_J = 170 mm·s^{-1}, a deflection frequency of ν = 1000 Hz, and a stage speed U_S = 4 mm·s^{-1}. b) Thinner electrodes obtained when reducing the jet speed through a decrease of the nozzle voltage: V_N = 630 V, U_J = 115 mm·s^{-1}, ν = 1000 Hz, U_S = 4 mm·s^{-1}. Notice that a similar change would be obtained when reducing the ambient relative humidity for example. c) Electrodes with recovered geometric parameters and fiber density produced by adjusting the deflection frequency and stage speed to the new jet speed. V_N = 630 V, U_J = 115 mm·s^{-1}, ν = 670 Hz, U_S = 2.7 mm·s^{-1}.

Figure 4.6b displays the same interdigitated electrodes as in Figure 4.6a but printed with a lower jet speed, 115 mm·s^{-1}. In this case, the lower jet speed was not related to a change of any external parameter, but it resulted from a decrease of the nozzle voltage. Notice that if no additional process parameter is modified, the arm width of the new electrode is strongly reduced, which would significantly change the characteristics of the electronic device. Larger changes in the jet speed could result in larger deterioration of the printed object due to fiber bucking or fiber stretching, as discussed in the introduction. Our method allows rapidly determining the jet speed to either adjust it to return to the previous value (by changing nozzle voltage if the jet speed was unintentionally modified by a change of printing conditions, for example) or by adjusting the printing parameters to recover the desired object characteristics.

In Figure 4.6c we display the same interdigitated electrodes, obtained with the same nozzle voltage as in Figure 4.6b, but printed after adjusting the process parameters, in this case the jet deflection frequency and stage speed, to accumulate the same amount of fiber, thus compensating for the jet speed change. By doing so, the initial electrode arm dimensions and internal geometry were recovered.

The proposed method allows for in situ and in line jet speed determination to EHD printing. Importantly, the method can be easily implemented in an EHD printer regardless of whether or not the printer uses jet deflection during the printing (although jet deflection is used in the determination of jet speed). While the present work provided a proof-of-concept where the opportunities and regimes at which this approach is best practiced are explored, further work is required for the implementation and validation of the in-situ monitoring system, which includes the development of proper illumination system, detectors to capture the printed pattern geometry and an algorithm for image recognition and computation of the jet speed discussed above. Image analysis is typically done by applying a threshold to convert obtained images into black-and-white to enhance accuracy. Then, the fiber track width can be computed by calculating the number of pixels representing the fiber track. Preferably, the width of the fiber track and the centerline position can be determined through detecting the edges of a fiber track, similarly to Figure 4.5a-b, ultimately allowing not only the in-situ monitoring of the jet speed, but also of the stability/displacement of the jet ejection point on the pendant drop. Depending on the size and complexity of printed objects, such image recognition may be used even continuously.

Once the jet speed is computed, these data may be used for the feedback loop control of the printing process. As printing speed and jet speed must be matched for printing with high fidelity, two options exist. One is controlling the jet speed via such parameters as nozzle voltage or ink supply rate for bringing the jet speed to its preset value. The opposite strategy would be to adjust the jet deflection parameters such that the printing speed would match the new jet speed. To find proper jet deflection parameters, first the desired motif and its size must be selected, which allows computing the fiber length going into one layer. Practically, this is easily achieved in our custom-made software, which computes a “perimeter” dimensionless number, representing the length of the motif divided by the length of its size in X or Y dimension (e.g., such a number equals to 4 for a square, to π for a circle, etc.).

Then, multiplying this dimensionless number by the desired size of a printed motif (e.g., 0.2 mm), the length of the fiber needed for printing one layer is obtained. Then, deflection frequency is computed by dividing the specific jet speed by the fiber length needed for one layer. Finally, for the computed frequency, the deflection amplitude must be chosen which provides the necessary jet deflection angle[34]. We point out that successful implementation of the proposed method for the in situ speed monitoring and automated control in a feedback loop would require extensive parametric study of the jet deflection process, as well as subsequent optimization of an algorithm matching those speeds. Considering that this method enables measuring the jet speed multiple times per second, it will prove priceless for generating data sets free of human error and bias for high-throughput analysis of multiple printing parameters and ink compositions on the jet speed and stability. Future advancement of EHD jet printing requires more automation of the printing process and is dependent on the capability to monitor the EHD jet stability and arrival speed in situ. As the present work enables a simple method to compute the jet speed from the width of fiber tracks, it opens fascinating opportunities for the future automation of EHD jet printing.

4.6. Implementation of an in situ inspection system

As it has been previously said, the method can be implemented using standard machine-inspection optics and image recognition software, to automatically detect the widths of the printed structure (both of 2D fiber tracks and of 3D structures). Figure 4.7 illustrates this, where the printed fiber tracks are imaged with a standard CMOS camera coupled to a conventional microscope using standard fiber optic illumination (see Chapter 2 for further details). The jet was electrostatically deflected along a plane perpendicular to the direction of stage motion (Figure 4.7a). The stage moved much slower than the jet speed, so that fiber was laid down nearly perpendicularly to the direction of substrate motion, as it is shown in Figure 4.7b-d. The frequency and amplitude of the jet deflection signal were high enough to deposit fiber without buckling. As the fiber is straight and perfectly aligned, the jet speed is computed as the product of twice the width of the track times the frequency of the jet-deflecting signal. The computed jet speeds for Figure 4.7b-d were: (b) 42 $mm \cdot s^{-1}$, (c) 37.5 $mm \cdot s^{-1}$, and (d) 37 $mm \cdot s^{-1}$.

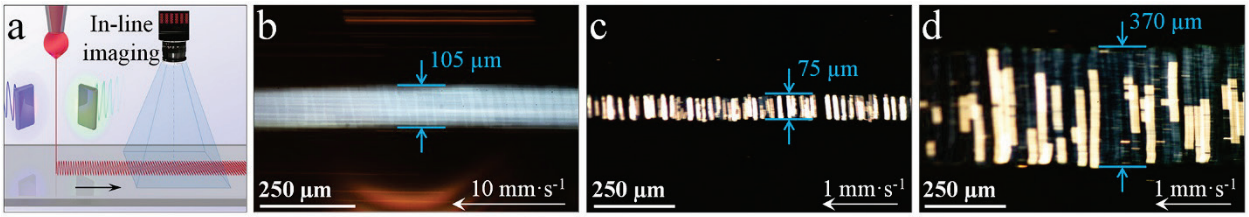

Figure 4.7. In-situ monitoring of the jet speed via the width of a printed fiber track. Schematic (a) and top-view optical photographs (b-d) of PEO fiber tracks collected while the substrate moves sideways, and the jet is deflected in the perpendicular direction with a sawtooth signal, with frequencies and amplitudes of: (b) 200 Hz and 1200 V, (c) 250 Hz and 1100 V, and (d) 50 Hz and 1100 V. The photographs were taken with a CMOS camera with the same substrate speed as used during printing. Exposure times: (b) 50 ms, (c) 10 ms and (d) 25 ms. Deposition conditions: (b) is the same as case C in Figure 4.1b, and (c) and (d) are close to Figure 4.4 cases E and A, respectively, but with a slower jet (leading to straight fibers). The computed jet speeds were: (b) 42, (c) 37.5, and (d) 37 mm·s^{-1}.

As the track's width can be optically determined using a standard camera, this method does not rely on resolving individual fibers and does not require expensive microscopy nor laborious analysis. Figure 4.7b used 10 mm·s^{-1} substrate speed, producing a blurred image, while Figure 4.7c and 4.7d used a lower speed of 1 mm·s^{-1}, resolving individual fiber tracks. The shiny golden lines visible in this case result from stronger scattering from multiple fibers stacked on top of each other by self-assembly (as explained earlier). The track's width, however, is independent of the extent of self-assembled fiber under these conditions. Note also that in Figure 4.7b the substrate travels 500 µm during the exposure time, so the illusion of individual fibers may result from aliasing of the printing frequency (200 Hz) with the LED light source frequency (50 Hz).

Chapter 5

Parametric study on the jet speed and fiber diameter

After demonstrating the capabilities of electrostatic jet deflection printing when the jet arrival speed matches with the printing speed, the goal of this chapter is to show how the jet speed can be tuned by modifying several printing parameters. Here, electrostatic jet deflection is used to determine the dependence of the jet speed and the characteristics of the collected fiber on several ink properties, ambient conditions and processing parameters.

5.1. Effect of the jet dynamics on the printing quality

Figure 5.1 illustrates the effect of relative variations of the jet speed on the quality of the printed pattern. Several flowers were printed on a motionless collector by using jet deflection electrodes. Each flower was deposited by stacking 10 layers one on top of the other, at a printing speed of 50 layers per second.

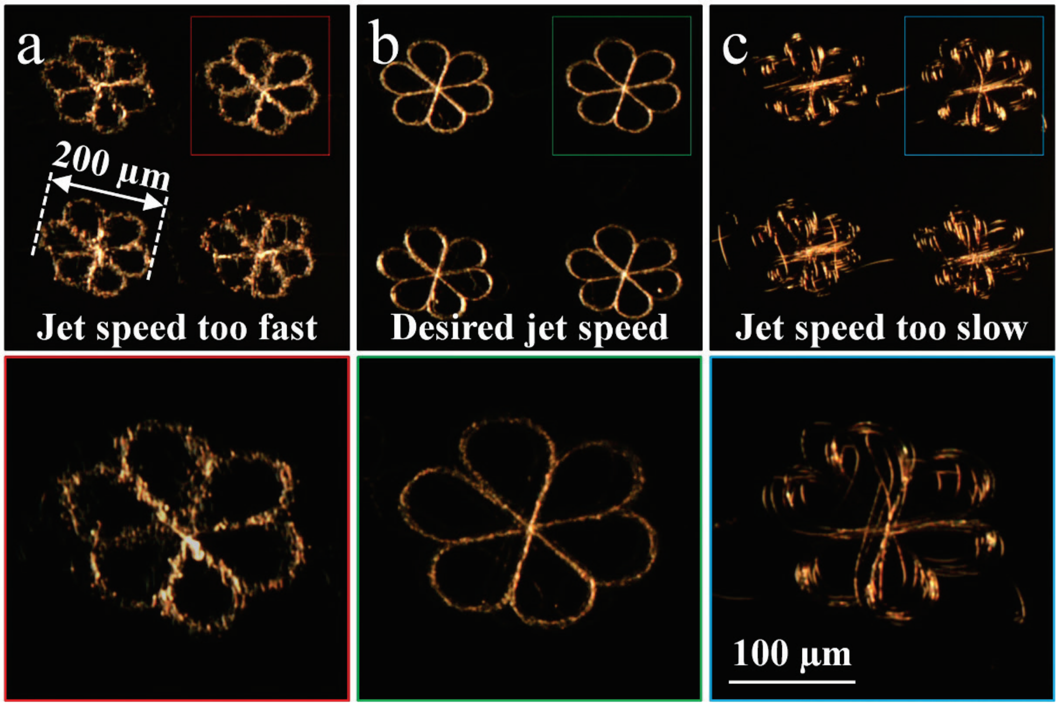

Figure 5.1. Effect of the jet speed (U_J) on the quality of the printed patterns. The printing speed (U_P) was controlled by the amplitude and frequency of the signal applied to the jet deflection electrodes. The top images show flowers produced from the overlapping of 10 fiber layers, and the bottom images display a magnified single flower. a) $U_J > U_P$, resulting in buckled fiber. b) $U_J \approx U_P$, achieving a proper fiber deposition that allows stacking different layers, one on top of each other, to build 3D structures. c) $U_J < U_P$, resulting in poor control of the fiber positioning.

As illustrated in this figure, matching the jet and printing speeds is fundamental to reproduce accurately a predefined design. Too fast and too slow jets result in poor quality patterns as the collected fiber is too long or too short and thus buckles or cuts corners on its arrival at the collector (Figure 5.1a,c). Thus, accurate printing requires being able to measure the jet speed, understand how it changes with the numerous parameters and being able to tune either the printing or the jet speed. A non-exhaustive list of the parameters that influence the jet speed is displayed in Table 5.1. These parameters can be classified regarding the ink properties, processing parameters, printer setup and ambient conditions. In the following sections, we detail how some of these parameters affect the jet speed and the collected fiber diameter.

Table 5.1. Operational parameters that affect the jet speed. Parameters are classified relative to the ink properties, processing, printer setup and ambient conditions. The bold parameters are the ones analyzed in the present work.

	Parameters
Ink	**Polymer** type, **MW**, **concentration**
	Solvent vapor pressure
	Additional components (**salts**, nanoparticles)
	Ink properties (density, **viscosity, electrical conductivity**, electrical permittivity, surface tension)
Processing	**Nozzle voltage**
	Infusion pump rate
	Stage translation speed
	Jet deflection parameters (amplitude, frequency)
Printer setup	**Nozzle to collector distance**
	Nozzle surface roughness, **diameter**, geometry
	Stage translation acceleration
Ambient	**Temperature**
	Relative humidity
	Atmosphere composition
	Pressure

5.2. Ink properties

Figure 5.2 displays the dependence of the jet speed and the fiber diameter on four ink parameters: polymer MW, polymer concentration, ink viscosity and ink electrical conductivity. To determine the influence of the polymer MW beyond variations in viscosity, we produced jets from inks containing different concentrations of polymers with distinct MWs, in the range from 0.3 MDa to 5 MDa, such that they had similar zero-shear viscosity, of around 1.8 – 1.9 Pa·s (Table 5.2).

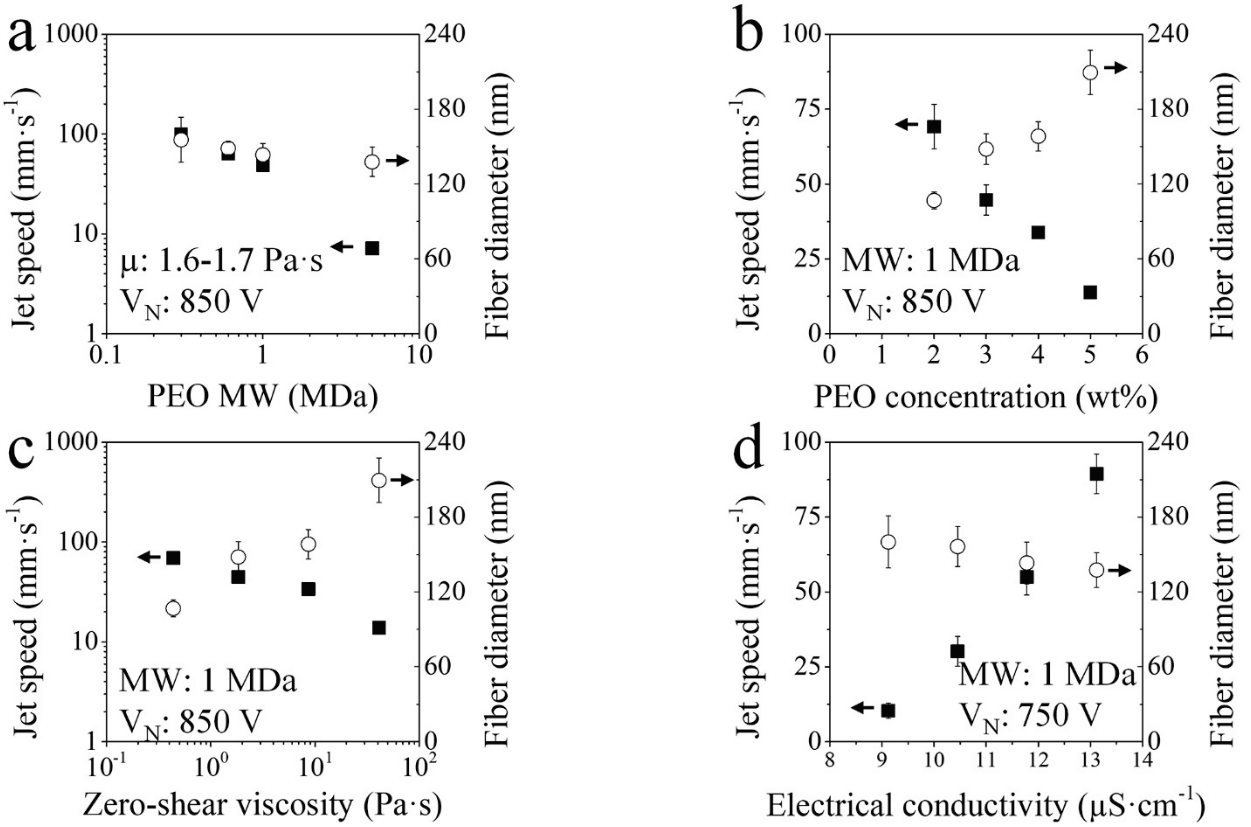

Figure 5.2. Effect of ink properties on the jet speed (axis Y-left) and the fiber diameter (axis Y-right). The infusion pump rate was fixed at 70 nL·min^{-1}, temperature and relative humidity at 19.5 ºC and 60 %, respectively. The nozzle to collector distance was set at 3 mm, and a nozzle with 250 μm of outer diameter was used. a) Effect of the polymer MW. Ink zero-shear viscosity was set at 1.8 – 1.9 Pa·s. b) Effect of the polymer concentration, choosing ink batches composed of PEO at 1 MDa. c) Effect of the ink viscosity of the ink batches used in graph “b”. Nozzle voltage (V_N) in (a,b,c) was set at 850 V. d) Effect of the ink electrical conductivity using ink batches composed of 3 wt% PEO at 1 MDa and different concentrations of NaCl. Nozzle voltage (V_N) was fixed at 750 V.

Figure 5.2a displays the effect of the PEO MW on the jet speed and the fiber diameter at a fixed nozzle voltage (V_N). Inks containing higher MW polymers resulted in slower jets associated with the higher elasticity of the ink (*i.e.* higher entanglement number, Table 5.2), so the jet is slowed down by higher elastic dissipations. Regarding the fiber diameter, as the PEO MW increases and its concentration in the ink decreases to keep similar zero-shear viscosity, slightly thinner fibers were collected on the substrate, as a result of the lower concentration of PEO in the jet.

Table 5.2. Composition and properties of the inks used in this work. PEO of different M_V was dissolved in a solvent is composed of a H_2O:EtOH mixture (1:1 mass ratio). Prior to properties measurement, inks were stored overnight in an oven at 25 ºC to ensure measuring the zero-shear viscosity (η_0) and the electrical conductivity (σ) at the same temperature for all inks.

Ink batch	**PEO wt %**	**PEO M_v (MDa)**	**NaCl wt%**	**Solvent**	**n_e**	**η_0 (Pa·s)**	**σ ($\mu S \cdot cm^{-1}$)**
#1	5.5	0.3	0	H_2O:EtOH (1:1, wt.)	6.1	1.92	13.1
#2	3.9	0.6	0		8.5	1.87	11.4
#3	2	1	0		7.1	0.44	8.3
#4	3	1	0		10.7	1.84	9.0
#5	4	1	0		14.5	8.66	9.6
#6	5	1	0		18.3	41.2	9.9
#7	3	1	0.3		10.7	1.93	10.5
#8	3	1	0.6			1.94	11.8
#9	3	1	0.9			1.94	13.1
#10	1.4	5	0		24.6	1.90	6.1

Figure 5.2b,c displays the effect of the PEO concentration and the ink viscosity on the jet speed and fiber diameter, setting 1 MDa as the PEO MW. Additionally, Figure 5.3 illustrates the effect of the PEO concentration on the ink viscosity. Consistently with previous reports[60,90–92], the ink viscosity increases with the PEO concentration, slowing down the jet speed because of the electrostatic forces has to overcome higher viscous forces.

Regarding the diameter of the printed fibers, increasing the PEO concentration and ink viscosity, thicker fibers are printed since thicker jets containing a larger amount of polymer are pulled from the drop owing to the stronger viscous forces (Figure 5.2b,c)[58,62].

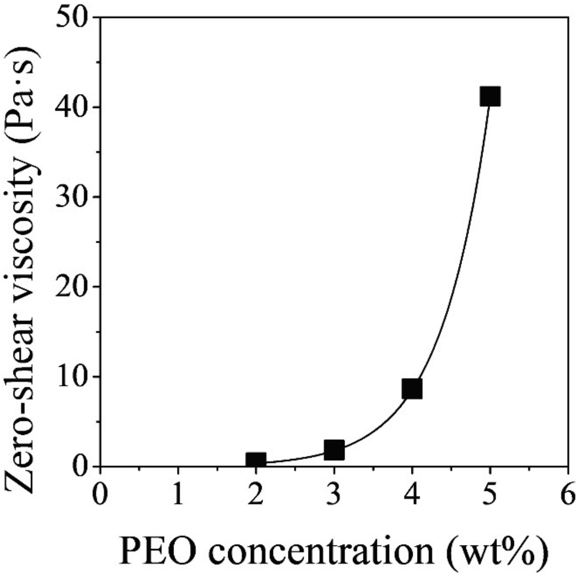

Figure 5.3. Effect of the PEO concentration on the ink's zero-shear viscosity. PEO 1 MDa was dissolved in different concentration for measuring the ink zero-shear viscosity. The solvent is composed of a mixture of H_2O:EtOH (1:1, wt.). Viscosity measurements were carried out at 25ºC. The zero-shear viscosity data fits with the equation $y = 0.016 \cdot 4.82^x$, where the variable "*y*" is the zero-shear viscosity (in Pa·s) and "*x*" is the PEO concentration (in wt%).

Adding salts to the ink allows tuning its electrical conductivity, which is another parameter that produces a huge effect on the jet speed. As Figure 5.2d illustrates, the ink electrical conductivity increases by the addition of larger amounts of NaCl (Table 5.2), and faster jets are ejected because a higher ion concentration accumulates at the drop surface, thus increasing the pulling force towards the grounded collector. Concerning the fiber diameter, increasing the ink electrical conductivity resulted in slightly thinner fibers, as a result of more pointy jet ejection point that produced thinner jets[62].

5.3. Processing parameters

The influence of the V_N and infusion pump rate on the jet speed and fiber diameter is displayed in Figure 5.4. Graph "a" from this figure shows how higher V_N generated faster jets, as a result of the stronger electrical field between the nozzle and the substrate. This higher electric field concentrated more ions on the drop surface, so more pointy Taylor cone was produced and thinner fibers were collected[93].

As shown in Figure 5.4b, the jet speed does not monotonously change with the infusion pump rate, but a maximum jet speed is obtained at a particular infusion rate. In contrast, thinner fibers are printed on the substrate as the infusion pump rate increases. We hypothesize that, at low infusion pump rates, the drying of the drop surface increases the jet viscosity, resulting in slow jets. This hypothesis is consistent with the increase of the fiber thickness when decreasing the infusion pump rate. As the infusion rate increases, the effect of the solvent evaporation decreases since higher infusion rates allow diluting the polymer concentration and refreshing the drop surface. However, too high infusion pump rates involve a large growth of the drop size, perturbing the electrical field around the jet. As a result, weaker electrostatic forces pull the jet, reducing its speed.

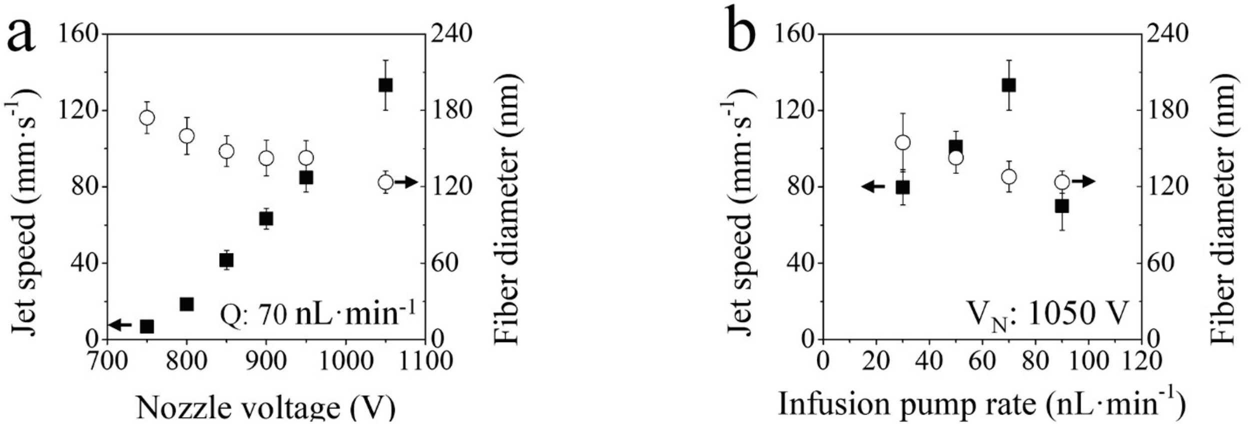

Figure 5.4. Effect of processing parameters on the jet speed (axis Y-left) and the fiber diameter (axis Y-right). Ink composed of 3 wt% PEO at 1 MDa was chosen to carry out this study. Temperature and relative humidity were maintained at 19.5 ºC and 60 %, respectively. Nozzle to collector distance was fixed at 3 mm and a nozzle with 250 µm of outer diameter was used. a) Effect of the V_N, while the infusion pump rate was fixed at 70 $nL \cdot min^{-1}$. b) Effect of the infusion pump rate, fixing V_N at 1050 V.

5.4. Setup design

We examined the effect of the nozzle to collector distance (H) and the nozzle outer diameter (OD) on the jet speed and the fiber diameter (Figure 5.5). As shown in Figure 5.5a, the jet speed decreases when increasing the nozzle-to-collector distance at a fixed voltage, which is related to the weaker electric field generated and thus the weaker pulling force. Regarding the fiber diameter, while we observed that stronger electrical fields allow collecting thinner fibers (Figure 5.4a), larger nozzle to collector distances also provided thinner fibers. We speculate that this fiber thinning with the increase of the distance is related to an additional stretching of the fiber before it reaches the substrate. Figure 5.5b displays how slower jets and thicker fibers are produced as the nozzle OD increases. At a set V_N, a larger nozzle OD implies weakening the electrical field around the jet, reducing the strength in which the electrostatic force pulls it. Besides, a larger nozzle OD entails a faster rate of solvent evaporation from the drop surface, due to the increase of the drop surface area. Consequently, the drop becomes more viscous. Both effects result in slower jets. Concerning the fiber diameter, as larger nozzle OD has associated faster solvent evaporation, increasing the polymer concentration, and consequently thicker fibers are collected[57].

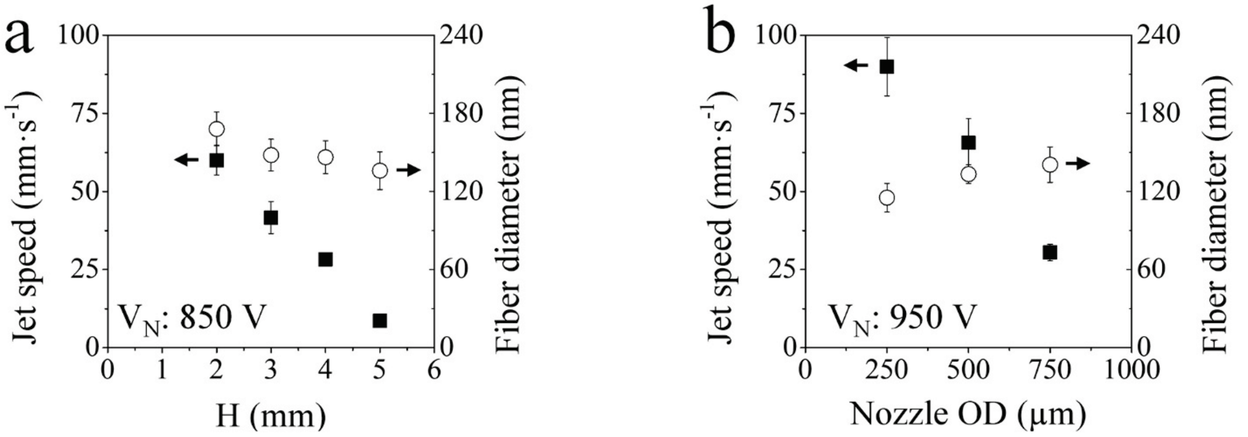

Figure 5.5. Effect of the printer setup on the jet speed (axis Y-left) and the fiber diameter (axis Y-right). Ink composed of 3 wt% PEO at 1 MDa was chosen to carry out this study. Infusion pump rate was fixed at 70 nL·min^{-1}, and temperature and relative humidity were maintained at 19.5 ºC and 60 %, respectively. a) Effect of the nozzle to collector distance at $V_N = 850\,V$. b) Effect of the nozzle outer diameter, fixing V_N at 1050 V.

5.5. Ambient conditions

When increasing the ambient temperature, the jet speed decreases and the fiber diameter increases, as Figure 5.6a displays. However, the jet speed increases and the fiber diameter decreases as the ambient relative humidity (RH) increases (Figure 5.6b). We associate these results to a faster drying of the drop surface at higher temperature and lower RH, so the drop polymer concentration and viscosity rise, leading to slower jets and thicker fibers.

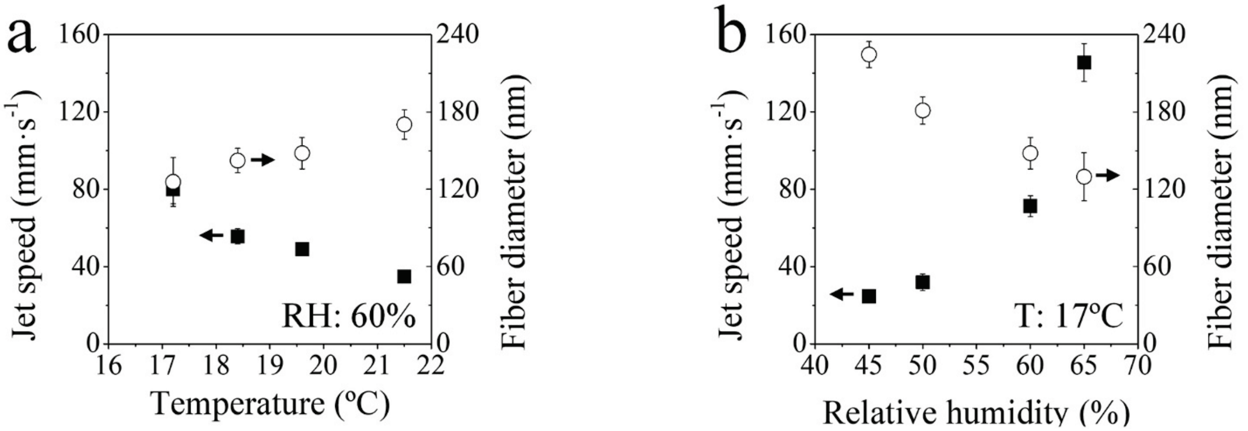

Figure 5.6. Effect of the ambient conditions on the jet speed (axis Y-left) and the fiber diameter (axis Y-right). Ink composed of 3 wt% PEO at 1 MDa was chosen to carry out this study, fixing V_N at 850 V and infusion pump rate at 70 nL·min^{-1}. A nozzle (250 µm of OD) was placed 3 mm away from the substrate. a) Effect of the temperature, while RH was maintained at 60 %. b) Effect of the RH, keeping constant the temperature at 17 ºC.

5.6. Energy balance for viscoelastic EHD jets

In developing a theoretical model, one must deal with the balances of mass, charge, momentum and energy. Instead of a complete theoretical framework, here we develop an energy balance under some simplifying assumptions. The goal is to use known parameters to theoretically predict jet speed or some estimate (or bound) of the jet speed.

The speed of EHD jets is defined by the equilibrium of multiple physical forces, such as hydrodynamic pressure and electrostatic forces[57,94]. In the energy balance, electrical work is mainly performed to obtain kinetic energy and surface energy as is involved in the formation and acceleration of a jet. In the process, the liquid resists this by different mechanisms, as viscous dissipation or elastic stretching. Since the variables involved are average variables at a given height (distance to the nozzle), we ignore radial dependences of the variables[95].

The balance that we propose considers the entrance and exit of energy into an imaginary box which contains only the jet, and has the upper side at the start of the jet (inside of the drop) and its bottom side at the end of the jet (near but above of the collector). As the start of the jet is assumed to be inside of the drop, at a point where the liquid starts to accelerate significantly from near quiescence, the variables and properties of the liquid (including speed) are assumed known. In addition, although the jet moves inside, we consider that this motion does not alter the energy balance, and therefore it is ignored.

Assuming a dielectric and incompressible liquid (constant density ρ and viscosity η) and negligible gravity effect at the liquid-air interface[96], the energy balance around the jet is defined as:

$$\dot{W} = \dot{K} + \dot{E}_S + \dot{E}_\mu + \dot{E}_E \tag{5.1}$$

where $\dot{W}$ is the electrical work, $\dot{K}$ is the kinetic energy, $\dot{E}_S$ is the surface energy, $\dot{E}_\mu$ is the viscous dissipation and $\dot{E}_E$ is the elastic energy.

Viscous dissipation and elastic energy terms are hard to estimate unless some knowledge of the velocity field is available. Additionally, as the ink is viscoelastic, viscous dissipation term is somehow connected to the elastic energy term, making more complicated their computation. Therefore, we propose the following inequality that involves all measurable variables:

$$\dot{W} > \dot{K} + \dot{E}_S \tag{5.2}$$

As $\dot{W}$ is the product of the electrical current times the voltage drop from the liquid drop (nozzle voltage) to the grounded collector, $\dot{K}$ is the product of the jet kinetic energy per unit volume exiting the system times the jet volume per unit time exiting the system and $\dot{E}_S$ is the product of the surface tension coefficient (γ) times the surface generation rate ($\dot{S}$), the previous inequality can be written as:

$$IV_N > \frac{1}{8}\pi\rho D^2 v^3 + \gamma\pi D v \tag{5.3}$$

where I is the electrical current in [A], V_N is the nozzle voltage in [V], ρ is the jet density in [kg·m^{-3}], D is the jet diameter in [m], v is the jet speed in [m·s^{-1}] and γ is the surface tension in [N·m^{-1}]. An efficiency defined as the ratio of $\dot{K} + \dot{E}_S$ divided by $\dot{W}$ can be used to check whether a significant portion of the work is invested in producing a thin jet with high speed, when the efficiency is reasonably close to 1, or only a small portion of the work is invested in this.

Figure 5.7 displays how much of the electric energy provided to the drop through HV was used as kinetic and surface energy to expel thin and fast jets when changing the ink properties, processing and setup parameters and ambient conditions. Such low values of efficiencies (*i.e.*, 0.1 – 1.4 %) are expected considering that the volume of the drop is immensely larger than the volume of the jet, so we hypothesize that most of the energy provided to the drop is used to overcome viscoelastic forces. As described in Sections 5.2 – 5.5, weaker electrical fields and drying of the drop surface result in slower jets, and therefore the efficiency of the energy provided to the drop needed to expel the jet decreased. On the other hand, higher efficiency was generally obtained when faster jets were ejected towards the collector. However, increasing the nozzle voltage in order to increase the jet speed did not cause an increase in the efficiency. This fact may be due to, while the jet was ejected at faster speed, its diameter was becoming thinner (Figure 5.4), and therefore the energy invested in moving a portion of mass from the drop towards the collector was kept similar.

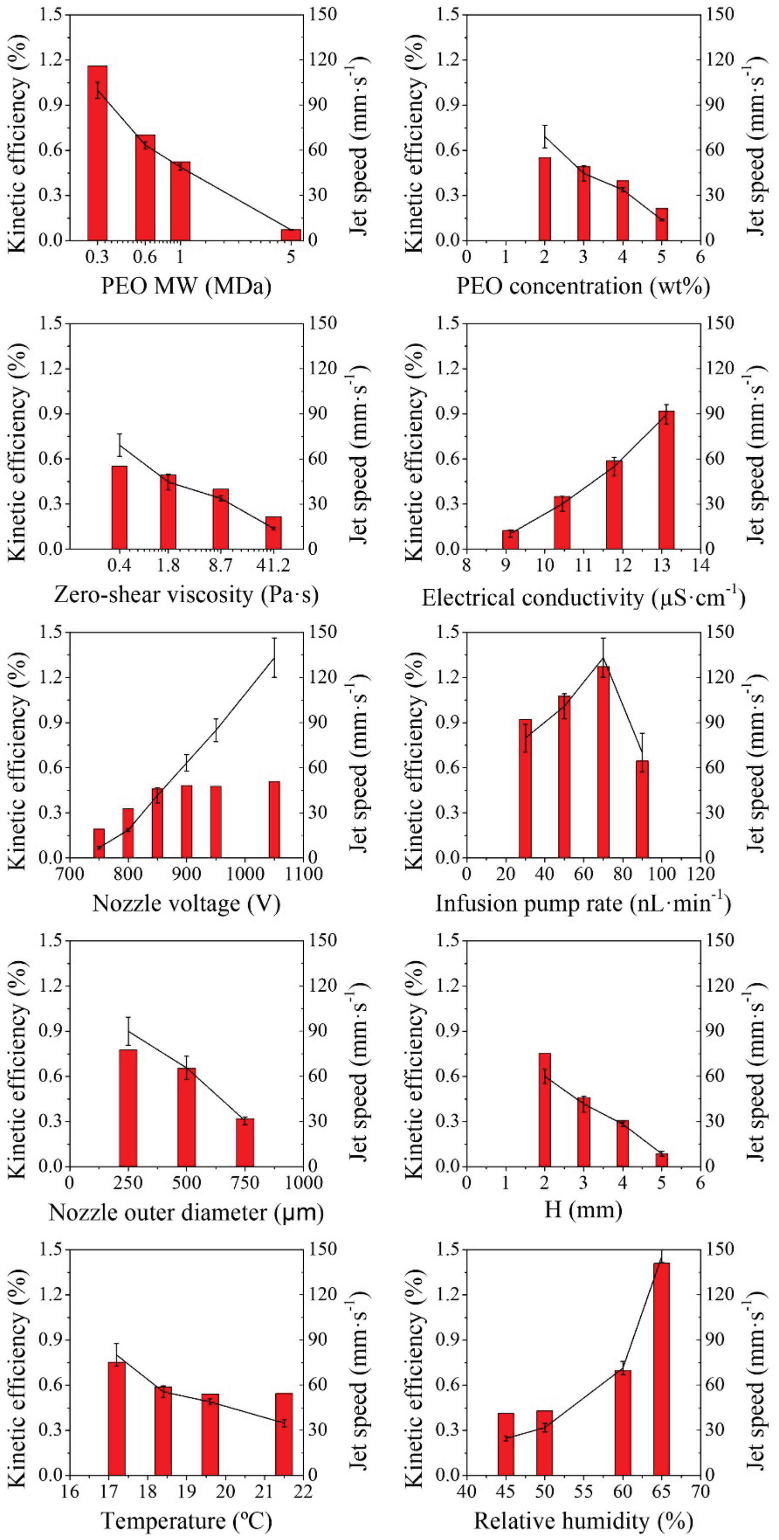

Figure 5.7. Electric energy invested in ejecting thin and fast jets. The jet speed and fiber diameter obtained in previous sections are used to compute how much of the energy provided to the drop is used to expel the jet. Kinetic efficiency (red bars, Y-left axis) and the jet speed (black lines, Y-right axis) are plotted at different ink, processing and ambient parameters.

Chapter 6

Stability and reproducibility of EHD jet printing

Using solvent-based inks provides great material versatility, but it may result in a poor stability of printing caused by the solvent evaporation from the drop, which strongly affects the drop properties. Therefore, the goal of this chapter is to study the parameters that affect the stability of EHD jet printing using solvent-based inks. To gain insight into the evolution of the printing process, the drop size and the jet ejection point are simultaneously monitored.

6.1. Parameters that affect the jet dynamics

Figure 6.1a displays a non-exhaustive list of the parameters that govern the EHD printing process and define the properties of the printed product. The list is classified into operational (or control) variables, dependent (or response) variables of the EHD jetting process, and characteristics of the printed pattern.

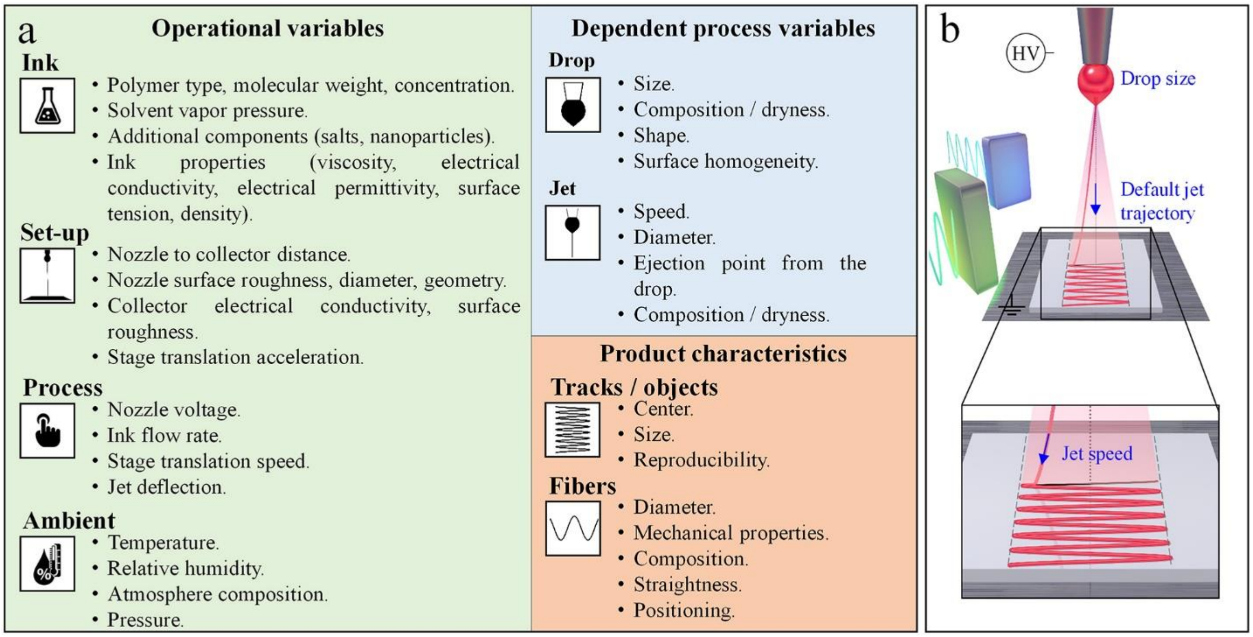
a
Operational variables
Ink
• Polymer type, molecular weight, concentration.
• Solvent vapor pressure.
• Additional components (salts, nanoparticles).
• Ink properties (viscosity, electrical conductivity, electrical permittivity, surface tension, density).
Set-up
• Nozzle to collector distance.
• Nozzle surface roughness, diameter, geometry.
• Collector electrical conductivity, surface roughness.
• Stage translation acceleration.
Process
• Nozzle voltage.
• Ink flow rate.
• Stage translation speed.
• Jet deflection.
Ambient
• Temperature.
• Relative humidity.
• Atmosphere composition.
• Pressure.
Dependent process variables
Drop
• Size.
• Composition / dryness.
• Shape.
• Surface homogeneity.
Jet
• Speed.
• Diameter.
• Ejection point from the drop.
• Composition / dryness.
Product characteristics
Tracks / objects
• Center.
• Size.
• Reproducibility.
Fibers
• Diameter.
• Mechanical properties.
• Composition.
• Straightness.
• Positioning.
b
HV
Drop size
Default jet trajectory
Jet speed

Figure 6.1. Principle of the EHD jet printing process with jet deflection and classification of the parameters involved in its performance. a) Parameters that govern the EHD jet printing process are divided between the operational variables, which can be modified by the user, the dependent variables, which cannot be directly controlled, and the product characteristics. b) Scheme of an EHD jet printing process including jet deflection electrodes.

To rationalize the complex EHD printing process, the stability of the dependent variables and their effect on the printing performance are examined by monitoring the drop size, the jet ejection point and how the patterns are printed over time by electrostatically deflecting the jet (Figure 6.1b).

6.2. Influence of the polymer molecular weight on the jet stability

When formulating an ink, it becomes necessary to increase its viscosity to avoid the development of capillary waves on the liquid jet, leading to the Plateau-Rayleigh instability. This instability deforms the cylindrical geometry of liquid jets causing their breakup into droplets. In our jets, the presence of a polymer in the ink is therefore essential to produce a stable jet, and its MW influences the printing process[83]. To determine the influence of the polymer MW independently from the obvious effects of viscosity, we produced jets from inks containing different concentrations of polymers with distinct MWs, in the range 0.3 MDa to 5 MDa, such that they had similar zero-shear viscosity, of around 1.8 – 1.9 Pa·s. Table 6.1 illustrates the properties of the inks used in this study.

Table 6.1. Ink compositions and their properties: PEO of different MWs were dissolved at different concentrations in a solvent composed of a H_2O:EtOH mixture (1:1 by wt.) to analyze the effect of the polymer MW on the jet speed and its stability. Additionally, 1 MDa PEO was dissolved in different solvent compositions to examine the effect of the drying of the drop surface on the jet ejection point. n_e indicates the entanglement number of each ink[85]. Before the measurement of the ink properties, the inks were kept inside an oven at 25 ºC overnight, and then the zero-shear viscosity (η_0) and electrical conductivity (σ) measurements were carried out at room temperature.

Ink batch	PEO M_v (MDa)	PEO wt %	Solvent	n_e	η_0 (Pa·s)	σ (µS·cm^{-1})
#1	0.3	5.5	H_2O:EtOH (1:1, wt)	6.1	1.92	13.1
#2	0.6	3.9		8.5	1.87	11.4
#3	1	3		10.7	1.84	9.0
#4	5	1.4		24.6	1.90	6.1
#5	1	3	H_2O:EG (4:1, wt)	12.4	4.22	39.2

However, to get similar ink viscosity, increasing the polymer MW results in decreasing the polymer concentration, and consequently the ink electrical conductivity of these inks is slightly reduced, which may affect the jet speed[51,97]. The jet speed was determined by measuring the width of the track printed when cyclically deflecting the jet using auxiliary electrodes, as shown in Figures 6.2 and 6.3 (see Chapter 2 for details).

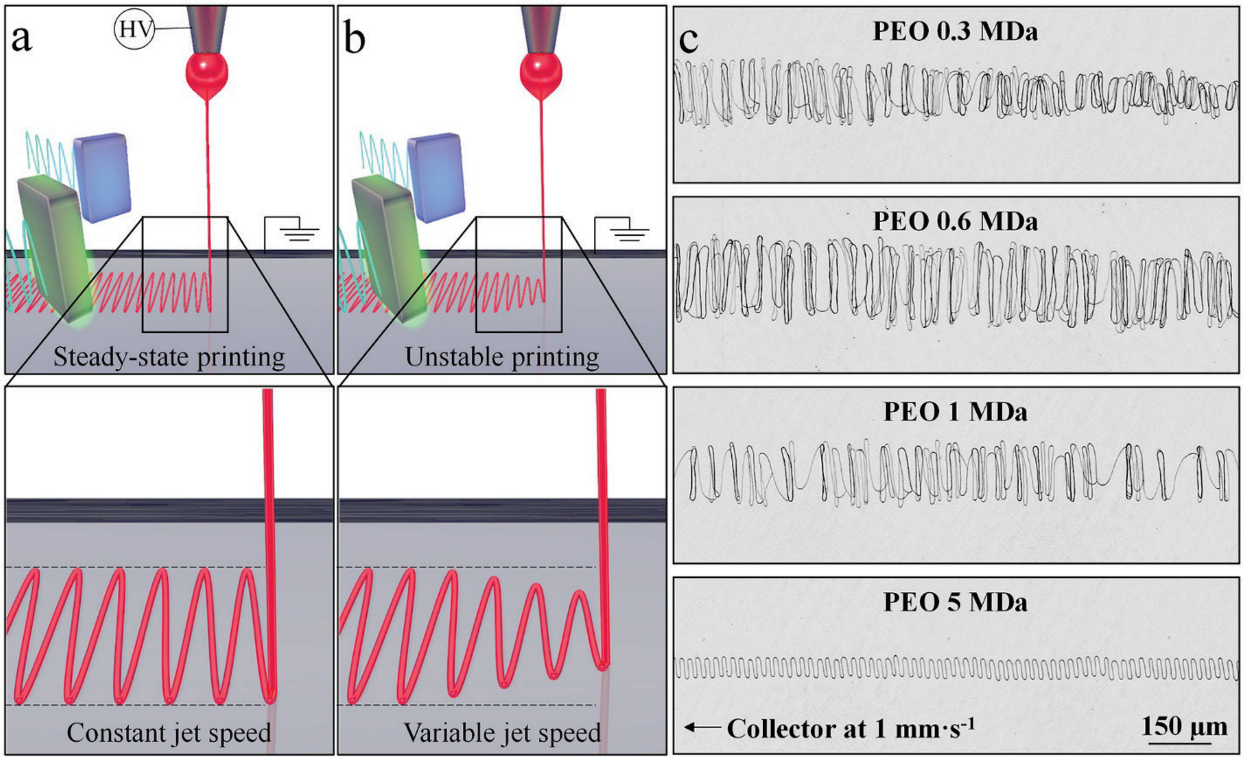
a
HV
Steady-state printing
b
Unstable printing
c
PEO 0.3 MDa
PEO 0.6 MDa
PEO 1 MDa
PEO 5 MDa
← Collector at 1 mm·s⁻¹
150 µm
Constant jet speed
Variable jet speed

Figure 6.2. Influence of the PEO MW on the printed pattern. The jet was deflected at different frequencies to match the printing speed with the jet speed. Then, the fiber track width and the known frequency of the deflecting signals are used to estimate the jet speed. a) Steady-state printing, in which the patterning of homogeneous fiber track and the jet speed keep constant. b) Unstable printing, which involves the patterning of fibers with variable lengths, as the jet speed changes. c) Patterning of fibers using PEO of different MWs. Nozzle voltage was fixed at 750 V and infusion pump rate at 70 nL·min^{-1}. Deflecting signal amplitude was set at 2000 V, while frequency was established at 300 Hz, 250 Hz, 150 Hz and 50 Hz for solutions with PEO 0.3 MDa, 0.6 MDa, 1 MDa and 5 MDa, respectively.

Figure 6.3 displays the time evolution of the jet speed at a fixed nozzle voltage of 750 V. During 5 minutes of printing, the jet broke twice when using an ink containing 0.3 MDa PEO, just once when using 0.6 MDa PEO, and did not break for 1 and 5 MDa PEO, for which the printing was stopped at 5 minutes. In subsequent experiments, we ran PEO 1 MDa beyond 30 minutes of printing (shown later below). The greater stability enabled by the higher MW PEOs is related to the higher number of entanglements of the polymer chains in the solution (Table 6.1), which increases its elasticity. This higher elasticity stabilizes the jet against breaking when being stretched by the electrical field[62,85,90].

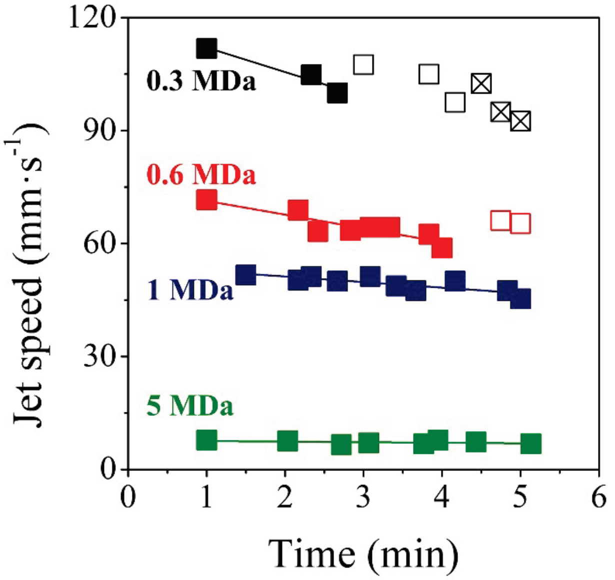

Figure 6.3. Influence of the polymer MW on the jet speed stability at constant zero-shear viscosity (1.8 – 1.9 Pa·s). PEO of different MWs were tested to analyze the jet speed stability. Ink compositions and their properties are shown in Table 6.1. Nozzle voltage was set at 750 V, while infusion pump rate was maintained at 70 nL·min^{-1}. At time 0, the jet was initiated. For the 0.3 and 0.6 MDa sets, different symbol fillings represent data obtained from different initiations of the jet after it was interrupted. Solid lines show the linear fitting of the time-dependence of the jet speed before its interruption.

Polymers with low MW enabled the ejection of faster jets, as observed from the tracks obtained at higher deflecting-signal frequency (Figure 6.2). These faster speeds are associated with not only a higher ink electrical conductivity[51,94,97,98], but also with a lower elasticity of the ink (i.e. lower entanglement number, Table 6.1), which means that the jet is slowed down by lower elastic dissipations.

In terms of stability, the jet speed was constant for the high MW PEO, but it decreased over time for the low MW PEOs. These variations in the jet speed were clearly visible in the printed patterns. When using low MW PEO, variable track widths, thus fiber lengths, were obtained along the track, demonstrating an unstable jet speed. In contrast, uniform fiber track widths were obtained with the slower jets from high MW PEO. Considering the jet speed stability for the 1 MDa case, this composition was chosen for further experiments on the stability of the printing process.

6.3. Stability of the drop size

The pendant drop at the exit of the capillary modifies the electric field between the nozzle and the collection substrate, thus altering the electrical pull on the jet toward the collector, and consequently influencing its speed. On the one hand, the drop introduces an electrostatic shielding at the jet emission, thus weakening the electrical field in that region. The larger the drop size, the larger perturbation of the electrical field and thus the lower the electric field at the drop tip. On the other hand, at a set nozzle-to-substrate distance, an increase in the drop size is associated with a decrease in the distance between its surface and the substrate, so the electrical field at the drop tip is enhanced. Overall, in a change of the drop size, the electrical field distribution around the jet changes, and so is the speed at which it is propelled towards the substrate. Thus, one a priori aims at adjusting the infusion pump rate so that the drop size stays constant.

Figure 6.4 shows the time evolution of the drop size, jet speed, fiber diameter and jet volume flow at two pump infusion rates, 20 and 40 $nL\cdot min^{-1}$. While the smallest infusion pump rate allows reaching a stable drop size sooner, the highest infusion pump rate results in a sustained increase in the drop dimensions (Figures 6.4a). Interestingly, the high infusion pump rate condition provides a more stable jet speed and thus a more stable printing (Figure 6.4b,d). At the smallest infusion pump rate tested, the jet speed and jet flow rate strongly decreased shortly after the drop size had stabilized, to disappear finally after around 15 minutes of jetting. At both flow rates tested, the fiber diameter is relatively constant over time (Figure 6.4c), although it tends to increase.

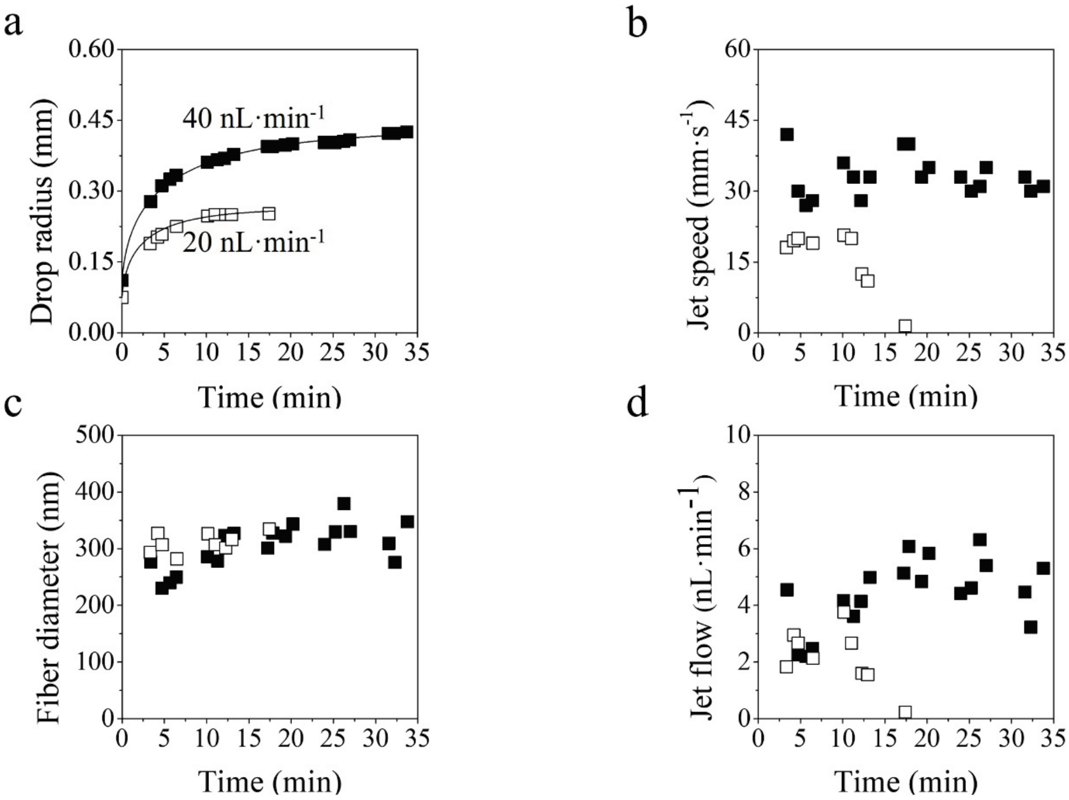

Figure 6.4. Evolution of the drop and jet parameters for two different infusion pump rates. The ink contains 1 MDa PEO and the nozzle voltage was set at 1000 V. Open and solid data points refer to 20 and 40 nL·min^{-1} infusion pump rates, respectively. a) Drop radius. The fitting function is based on Equation 6.3. b) Jet speed during the printing. Similar values were achieved by fixing infusion pump rate at 40 nL·min^{-1}, while the jet speed was not constant over time at 20 nL·min^{-1}. c) Diameter of the collected fiber. Thicker fibers printed on the collector suggests that the drop surface dried during the printing. d) Jet volumetric flow rate estimated with Equation 2.8.

Per unit time, the volume of ink injected (Q_{Ink}) is equal to the sum of the volume of ink ejected (Q_{Jet}), the volume of solvent evaporated (Q_E), and the volume change of the drop (dV_d/dt):

$$Q_{Ink} = Q_{Jet} + Q_E + \frac{dV_d}{dt} \tag{6.1}$$

Assuming that the solvent evaporation rate just evolves with the variation of the drop radius[99], i.e. the ink composition and the ambient temperature and pressure are constant:

$$Q_E = A \cdot R \tag{6.2}$$

Then, Equation 6.1 can be expressed as:

$$\frac{dR}{dt} = \frac{Q_{Ink} - Q_{Jet}}{4\pi R^2} - \frac{A}{4\pi R} \tag{6.3}$$

Equation 6.3 can be solved numerically, and considering Q_{Ink} as 40 and 20 nL·min^{-1} and Q_{Jet} as the average value obtained experimentally for both infusion pump rates (4.8 and 2.4 nL·min^{-1}, respectively), the value obtained for the constant A is 0.0065 mm^{2}·min^{-1}.

Figures 6.4a displays the evolution of the drop size as a function of time and a fitting using the theoretical drop radius expressed in Equation 6.3. Despite the approximations, the evolution of the drop radius experimentally obtained properly follows the theoretical trend.

A more realistic analysis of the process should consider that, due to the solvent evaporation, the polymer concentration at the drop ($C_{P,drop}$) continuously increases. Assuming that the polymer concentration of the jet (at the ejection point) is the same as the average polymer concentration within the drop, the polymer concentration should change as:

$$\frac{dC_{P,drop}}{dt} = \frac{M_{P,ink} - M_{P,jet}}{V_T} = \frac{Q_{Ink}C_{P,ink} - Q_{Jet}C_{P,drop}}{V_T} \tag{6.4}$$

Where $M_{P,ink}$ is the polymer mass flow rate that enters the drop. Assuming that Q_{Jet} can be considered constant (Figure 6.4d), but taking into account that the volume of the drop also changes with time:

$$C_{P,drop} = C_{P,drop\,0} + \frac{C_{P,ink}\left(Q_{Ink} - Q_{Jet}\right)}{Q_{Jet}} e^{-Q_{Jet}\int \frac{1}{V_T} dt} \tag{6.5}$$

Thus, the polymer concentration increases at a rate that depends on the difference between the ink and jet volumetric flow and on the volume evolution. Only when considering a homogenous polymer concentration within the ink, a constant drop volume and no solvent evaporation, $Q_{Ink} - Q_{Jet} = 0$ and then $C_{P,drop}$ should be constant, not perturbing the printing process. However, since the ink supply takes place at the nozzle and the solvent evaporation occurs at the surface of the drop, a polymer concentration gradient exists within the drop and the real concentration of polymer at the drop surface is much larger than the average polymer concentration within the drop. This polymer enrichment at the drop surface causes an increase in the ink viscosity at the drop surface and therefore in the jet, which decreases the jet speed and increases its thickness. Overall, a more stable printing is obtained using a pump infusion rate that is significantly larger than the jet ejection rate, thus the drop size generally increases. Since the volume of solvent evaporated increases with the drop surface area, at some point the drop size is stabilized (Figure 6.4a).

When the drop size becomes stable, *i.e.* its volume remains constant, a significant portion of the ink injected is just evaporated (as solvent from the surface of the drop), and the average polymer concentration within the drop and particularly on its surface increases. For example, in the situation when infusion pump rate was fixed at 20 $nL·min^{-1}$, the estimated jet flow rate was 3 $nL·min^{-1}$ (Figure 6.4d). Therefore, when the drop size becomes stable, the solvent evaporation rate was 17 $nL·min^{-1}$ approximately. In this scenario, the drop (surface) and thus jet viscosity are also increased, resulting in a sustained reduction of the jet speed as the viscous forces work against the jet flow, up to the point that it can disappear. Consequently, solvent evaporation will cause polymer enrichment at the surface of the drop, which can be significant due to the slow diffusion of polymer along concentration gradients. Consequently, drop surface drying will affect the ink composition at the drop tip where the jet is born, and thus its speed during the printing process. We hypothesize that higher infusion pump rates better stabilize the printing process against the drop drying because the effect of the solvent evaporation was less noticeable at the higher infusion pump rate tested, 40 $nL·min^{-1}$ (Figure 6.4), as the continuous drop growth and the constant refreshment of ink at the surface of the drop slowed down the polymer surface enrichment. However, as noted above, at a fixed nozzle-to-substrate distance and applied potential, as the drop size increases, the jet speed may be affected by the strengthening of the electric field around the jet. Thus, excessive infusion pump rates should destabilize the EHD printing, and have to be avoided as well. Nevertheless, we observed some other instabilities regarding the jet ejection mode and the jet's trajectory when the infusion pump rate was decreased to achieve stable drop size. These instabilities and some hypothesis about how to avoid them are explained in the following sections.

6.4. Irregular jet ejection regime

First, as reducing the infusion pump rate causes having slower jets (Figure 6.4), the nozzle voltage was increased to get faster jet speed. However, an undesired jet ejection regime took place during the printing when higher nozzle voltage was applied. It has been previously shown in the literature that certain values of infusion pump rates and nozzle voltage result in a pulsation regime of the jet ejection[100–103]. However, here we identify some regularity on the changes on the jet dynamics, which ejected continuously fast and slow jets in a repetitive mode.

Figures 6.5 shows fibers printed at three nozzle voltages in the range 950 - 1150 V. Homogeneous fiber tracks were initially printed at 950 V, but after repeating this printing at a higher nozzle voltage (1050 V) to get a faster jet, an inhomogeneous fiber track with certain periodicity was collected initially. The CMOS camera allows confirming that the jet was being emitted through pulses, and the electrostatic jet deflection allows associating this pulsation regime with continuous changes in the jet speed. After raising the nozzle voltage (1150 V), this pulsation regime was magnified when a stronger electrical field was created.

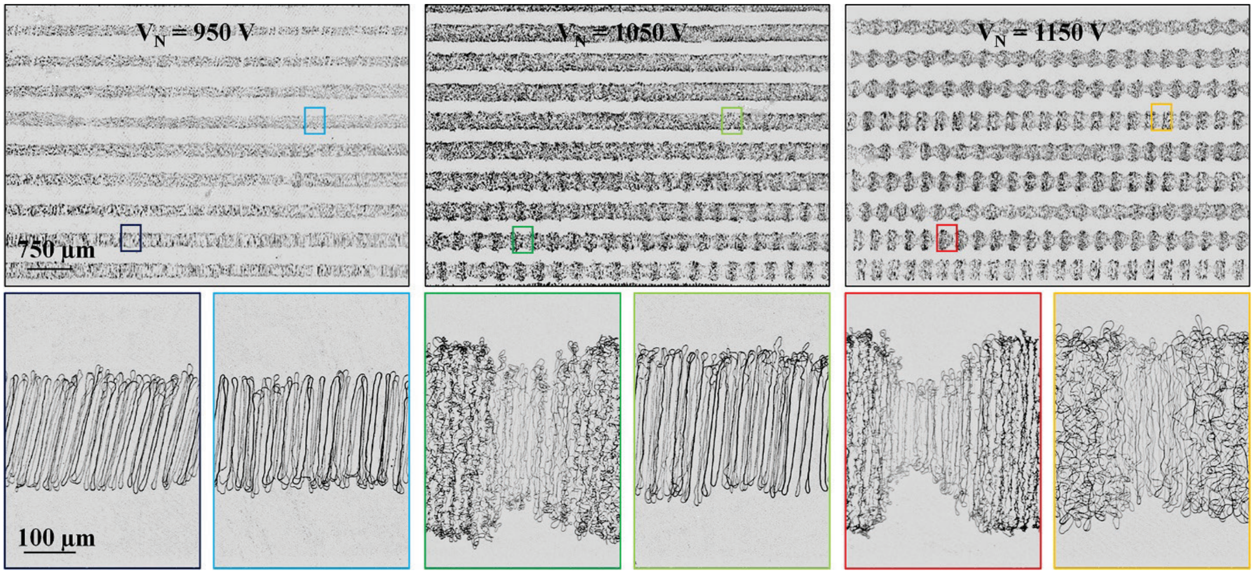

Figure 6.5. Effect of the nozzle voltage on the jet-ejection mode. Confocal microscopy images of the printed pattern at different nozzle voltages. The stage translates the substrate side-to-side along the X-axis for 10 mm and then the substrate is displaced along the Y-axis 0.5 mm at each extreme (see Chapter 2 for details). The top images show a general view of the printed pattern, and the bottom images display the magnified fiber track as marked by the color boxes. Ink is composed of PEO 1 MDa and the infusion pump rate was set at 20 nL·min^{-1}.

We hypothesize that this periodicity on the changes in the jet speed is due to a harmonic balance between the electrostatic and capillary forces on the drop surface[100,101]. To avoid this regime, the nozzle voltage and infusion pump rate have to be optimized to get stable regime[104]. For example, regarding our experimental conditions, nozzle voltage or infusion pump rate had to be reduced or increased, respectively, to get stable jetting.

6.5. Unstable default jet trajectory

Secondly, reducing the infusion flow rate to get constant drop size earlier lead to a stronger effect of the solvent evaporation, and consequently the droplet drying can affect the location of the jet ejection point on the drop, which governs the jet default trajectory between the drop and the substrate. To analyze the stability of the jet ejection position, the nozzle voltage and infusion pump rate were varied in the range of 850 – 1050 V and 30 – 70 nL·min^{-1}, respectively. These ranges of voltage and infusion pump rate were chosen because, within the experimental conditions used, they allowed the generation of long-living jets that were printed as fibers on the substrate. Lower nozzle voltages did not generate a jet, whereas higher voltages produced too fast jets that had not enough time to dry before reaching the substrate, resulting in ink puddles. Besides, lower infusion pump rates resulted in a fast drying of the drop, and higher infusion pump rates resulted in fast drop growth that eventually perturbed the electrical field. Figure 6.6a displays a jet being expelled from a drop when the nozzle voltage increases from 850 to 1050 V and the infusion pump rate is fixed at 70 nL·min^{-1}. Figure 6.6b shows the jet being expelled from the drop when the infusion pump rate decreases from 70 to 30 nL·min^{-1} and the nozzle voltage is fixed at 850 V.

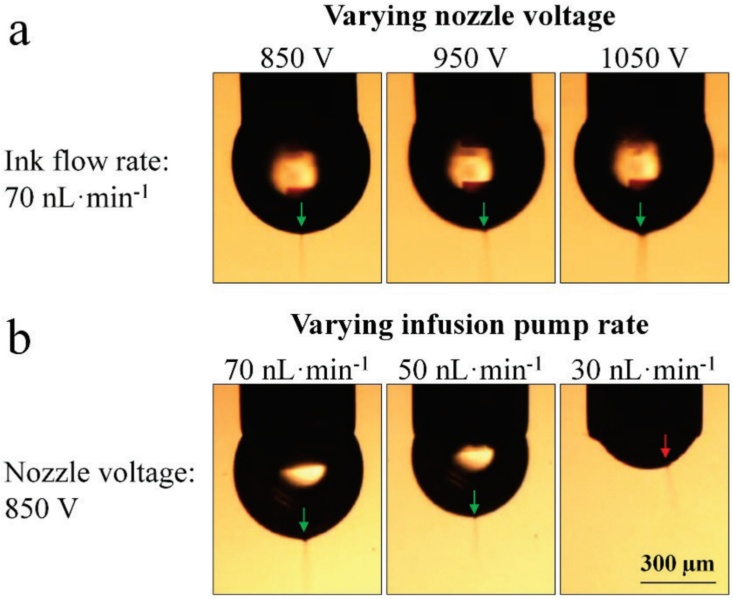

Figure 6.6. Influence of nozzle voltage and infusion pump rate on the jet ejection point. The jet ejection point maintained stable with increasing the nozzle voltage at a constant infusion pump rate (70 nL·min^{-1}), but it became unstable, shifting sideways, after decreasing the infusion pump rate at constant nozzle voltage (850 V). The ink was composed of PEO 1 MDa.

As observed in this figure, increasing the nozzle voltage did not significantly perturb the jet ejection point. Nevertheless, when the infusion pump rate was decreased, the drop size decreased and the jet ejection point was shifted sideways.

The use of jet deflection electrodes enables a facile in situ detection of instabilities in the jet ejection point or default trajectory, as they are reflected in a displacement of the track centerline (Figure 6.7a,b). Figure 6.7c displays confocal images of the produced tracks and the time evolution of their centerline. The default jet trajectory, or the track centerline, becomes unstable when reducing the infusion pump rate, which is consistent with the precession of the jet ejection point around the drop seen for this condition in Figure 6.6b.

The jet ejection point at the drop surface is determined not only by the electric field distribution at the drop surface, but also by the drop surface composition. We hypothesize that the unsteady precession of the point of ejection of the jet is related to compositional inhomogeneities generated at the surface of the drop when it is drying. This hypothesis explains the development of this instability when reducing the infusion pump rate, *i.e.* when the effect of the drying of the surface of the drop is more accentuated (Figure 6.4). Inhomogeneities on the surface composition of the drop, *e.g.* associated with an irregular drop drying, translate into disparities in the surface tension along the drop that shift the jet ejection point and thus the default jet trajectory, overall resulting in a translation of the center of the printed pattern (Figures 6.7c).

To evaluate whether these instabilities are related to the ink drying, we reduced the volatility of the ink by changing the solvent from EtOH to EG. With a solvent composition of H_2O:EG (4:1 wt.), the most significant changes in the ink properties were a higher ink viscosity and electrical conductivity (Table 6.1). To print dry fibers, the jet speed was reduced by decreasing the nozzle voltage. Figure 6.7d displays the deviation of the centerline of the printed fibers when the infusion pump rate was decreased from 70 to 30 $nL \cdot min^{-1}$ for an ink composed of 3 wt% PEO (1 MDa) dissolved in H_2O:EG (4:1 wt.), at constant nozzle voltage. As shown in Figure 6.7d, when using an EG-based ink, the default jet trajectory and the jet ejection point remain stable even if low infusion pump rates are used.

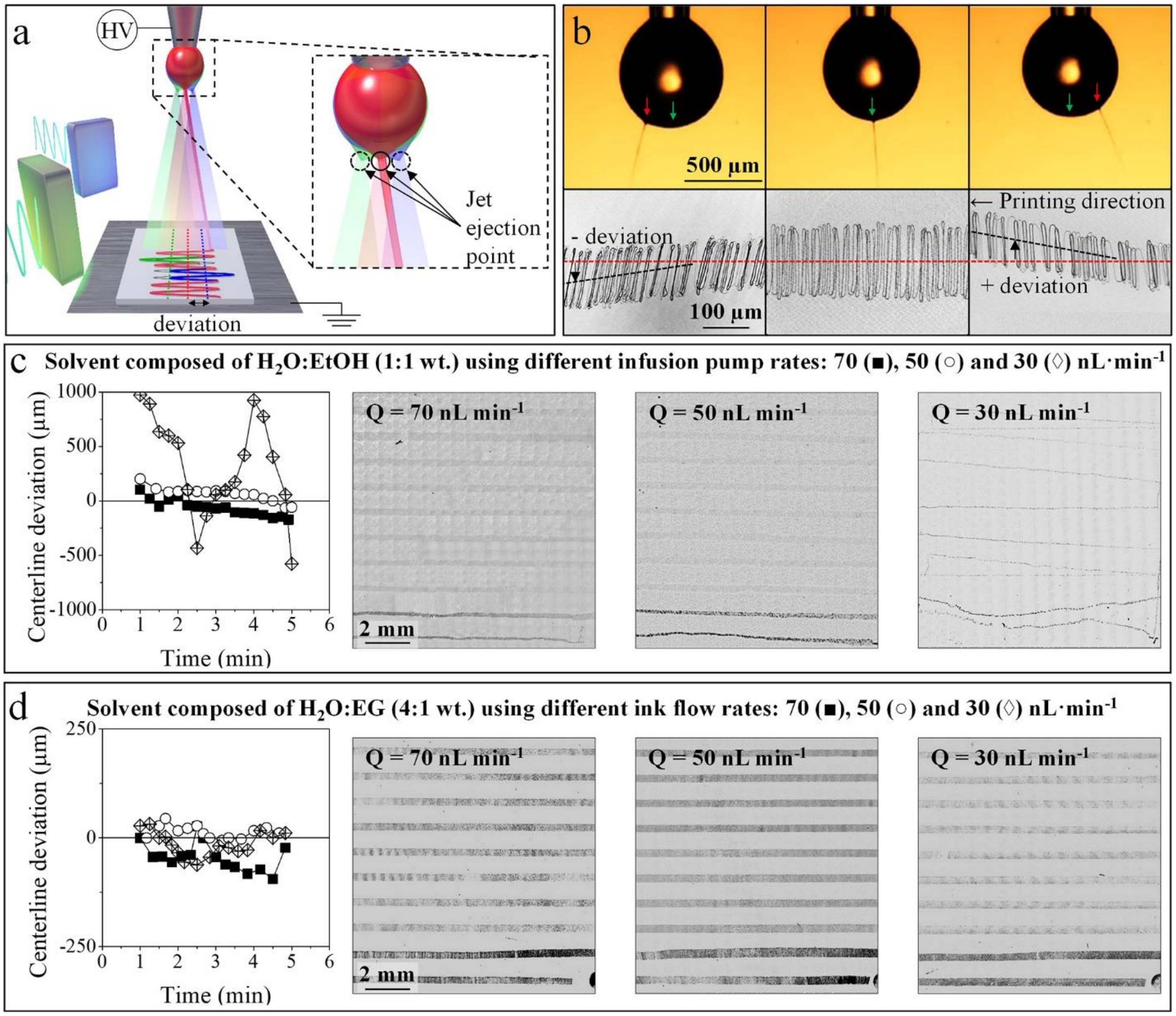

Figure 6.7. Analysis of the default jet trajectory using different solvent compositions and infusion pump rates. a) Schematic of how the jet-ejection mode affects the default jet trajectory. b) Optical images of the drop and confocal microscopy images of the printed fiber tracks with stable (middle) and unstable (left and right) default jet trajectory. Ink was composed of PEO 1 MDa dissolved in 1:1 wt. H_2O:EtOH solvent. Nozzle voltage was set at 850 V, and infusion pump rate was maintained at 70 nL·min^{-1}. c,d) Graph and confocal microscopy images showing the time evolution of the centerline deviation from a hypothetical stable track, obtained from an ink based on a solvent composed of 1:1 wt. H_2O:EtOH (c) and 4:1 wt. H_2O:EG (d). Solid squares, open circles and open diamonds refer to infusion pump rates fixed at 70, 50 and 30 nL·min^{-1}, respectively. Ink is composed of PEO 1 MDa, and nozzle voltage was fixed at 850 V in (c) and 700 V in (d).

To further study the effect of the solvent volatility on the printing process, Figure 6.8 displays the time evolution of the drop volume, jet speed and fiber diameter during the printing with EtOH-based and EG-based inks.

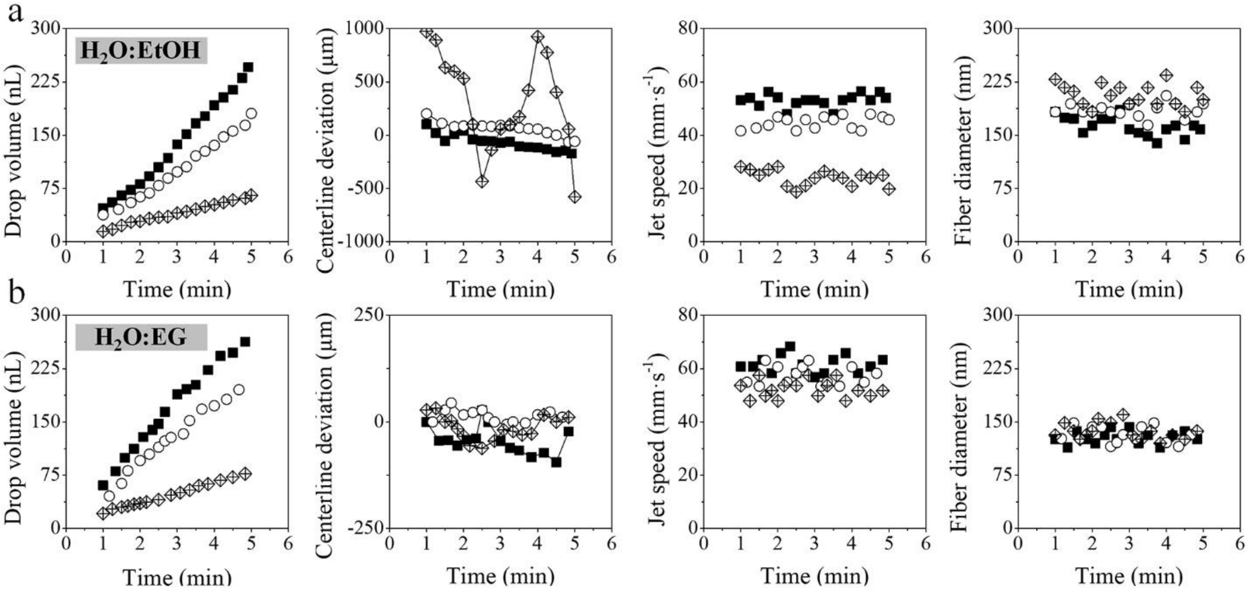

Figure 6.8. Effect of the jet deviation on the printing process: Drop volume, centerline deviation, jet speed and fiber diameter evolution over time, when ink batches composed of H_2O:EtOH at a ratio 1:1 wt. (a) and H_2O:EG at a ratio 4:1 wt. (b) were used. Nozzle voltage was set at 850 V in (a) and 700 V in (b). Solid squares, open circles and open diamonds refer to infusion pump rates fixed at 70, 50 and 30 nL·min^{-1}, respectively.

The lower solvent evaporation rate associated with the use of EG instead of EtOH as solvent leads to a more rapid drop growth, faster jets and thinner fibers associated with a lower drop viscosity. Thus, we conclude that minimizing the drying of the drop surface is key to stabilizing the jet for long times and printing reproducible patterns.

Chapter 7

Translation of jet deflection to melt electrowriting

This chapter presents additional results obtained during the research stay in Prof. Paul Dalton's group at the University of Oregon (EEUU), and its goal is to implement electrostatic jet deflection to a conventional MEW setup in order to enhance its printing capabilities.

7.1. Producing thin and fast jets

As EHD jet printing using molten polymers produces much thicker and slower jets than the ones produced by solvent-based inks, the first step consisted in optimizing the experimental conditions to produce thin and fast fibers. The most important parameters that affect the jet diameter were the pressure applied to push the molten polymer and the nozzle diameter. Low pressure (0.5 bar) was applied to the syringe to provide low polymer flow through the nozzle, and a nozzle tip with small ID (32G) was chosen to reduce the thickness of the ejected jet. On the other hand, the nozzle voltage was fixed at high enough values to allow ejecting fast jets, but also at low enough values (*i.e.*, 7 kV) to minimize arcing between the printhead, the collector and the jet-deflecting electrodes. PCL 12 was used since it enabled having high jet stability and fast jet speeds, as a result of the suitable viscosity of this polymer MW when it melts. The temperature was set to 80 ºC, only 15ºC above the PCL melting point to minimize its degradation. For further details, see Chapter 2.

Figure 7.1 illustrates the differences in the printed fibers obtained with conventional MEW approach, the MEW printer producing thin and fast jets and the upgraded MEW setup with the implementation of the jet-deflecting electrodes. Straight fibers were obtained using conventional MEW (panel "a"), since the jet was slower than the stage translation speed and the jet was pulled by the collector. The difference between the stage translation speed and the jet speed resulted in a jet lag (*i.e.*, the line segment between the nozzle position and the jet contact point on the collector[105]) that may degrade the quality of the printing. Larger differences between these two speeds lead to a larger jet lag. Despite this, some researchers have already analyzed this behavior and defined simple mathematical models to predict the jet lag and improve the deposition of the fibers[105]. The diameter of the printed fibers using this methodology is typically 5 – 20 µm, depending on the working conditions. Panel "b" illustrates the optimized MEW printer to produce thin and fast jets. In this case, as the jet was faster than the stage translation speed, the deposition of fibers could not be controlled, and the fibers buckled when they reached the collector.

Finally, the upgraded MEW setup via the implementation of the jet-deflecting electrodes is shown in panel "c", where fast fibers with diameters around 1 µm (Figure 7.2) were precisely deposited on the collector by controlling the electrical field around the jet.

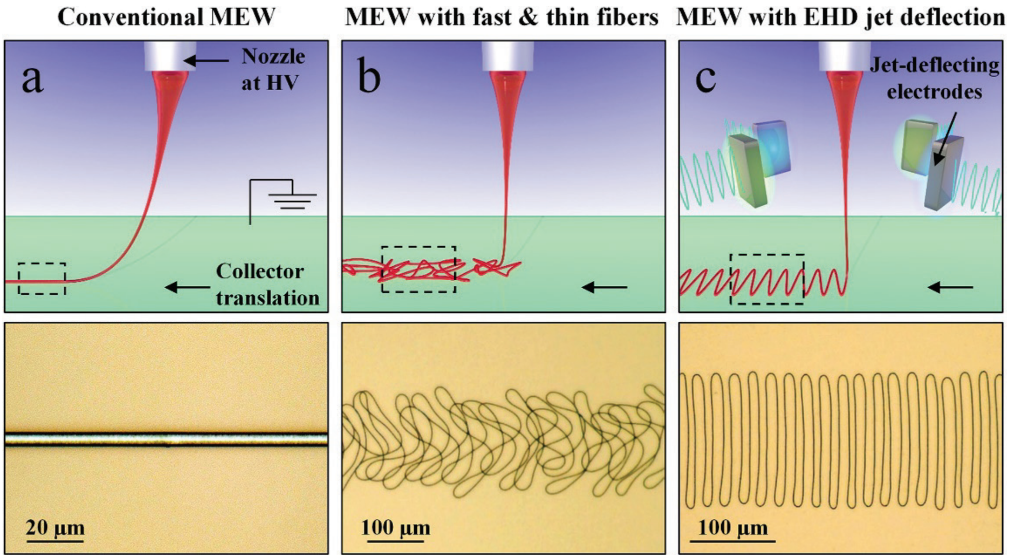
Conventional MEW
MEW with fast & thin fibers
MEW with EHD jet deflection
a
Nozzle at HV
Collector translation
b
c
Jet-deflecting electrodes
20 µm
100 µm
100 µm

Figure 7.1. From conventional MEW to upgraded MEW with the implementation of jet-deflecting electrodes. a) Conventional MEW, which is based of stretching the jet to precisely deposit fibers on the collector. b) Optimized MEW printer to produce thin and fast jets. As the jet speed is faster than the stage translation speed, the fiber buckles when it reaches the collector. Consequently, the deposition of the fiber track is not controlled. c) Upgraded MEW setup by implementing jet-deflecting electrodes around the nozzle to modify the electrical field near the jet and control the deposition of the fibers. Stage translation speed was set at 2 mm·s^{-1}, and black arrows indicate its translation direction. Top images illustrate the schematics of each printing method, and bottom images show the printed fiber tracks.

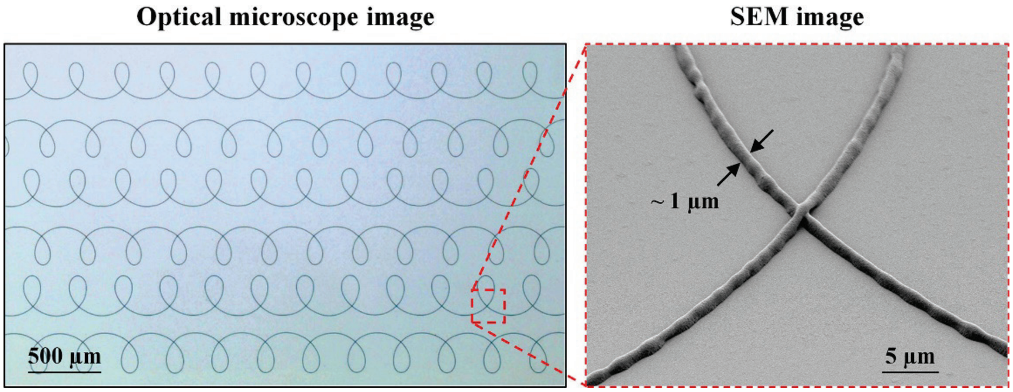
Optical microscope image
SEM image
500 µm
~ 1 µm
5 µm

Figure 7.2. Micron-scale fibers printed using molten polymers. The stage translation speed was set at 10 mm·s^{-1} while the jet was deflected at 4 kV and 50 Hz.

7.2. Jet deflection in melt electrowriting

Figures 7.3 illustrate the first results of EHD jet deflection using molten polymers. Fast fibers were precisely deposited on the collector by means of controlling the electrical field around the jet via the jet-deflecting electrodes. Any pattern geometry can be virtually printed using EHD jet deflection (Figure 7.3b) to obtain a desired fiber track while the stage is moving continuously, as the deflecting signal can be controlled easily through the LabVIEW software. Similarly, as shown in Chapter 4, the pattern geometry can be rotated to a desired deflection angle relative to the translation direction, as Figure 7.3c exemplifies. Additionally, 3D structures at micrometer sizes (Figure 7.3d) were printed layer-by-layer on a motionless collector using EHD jet deflection. Such small sizes of 3D structures (≈ 100 µm) cannot be printed using conventional MEW printer (limited to ≈ 1 mm) but were easily achieved by controlling the jet-deflecting approach.

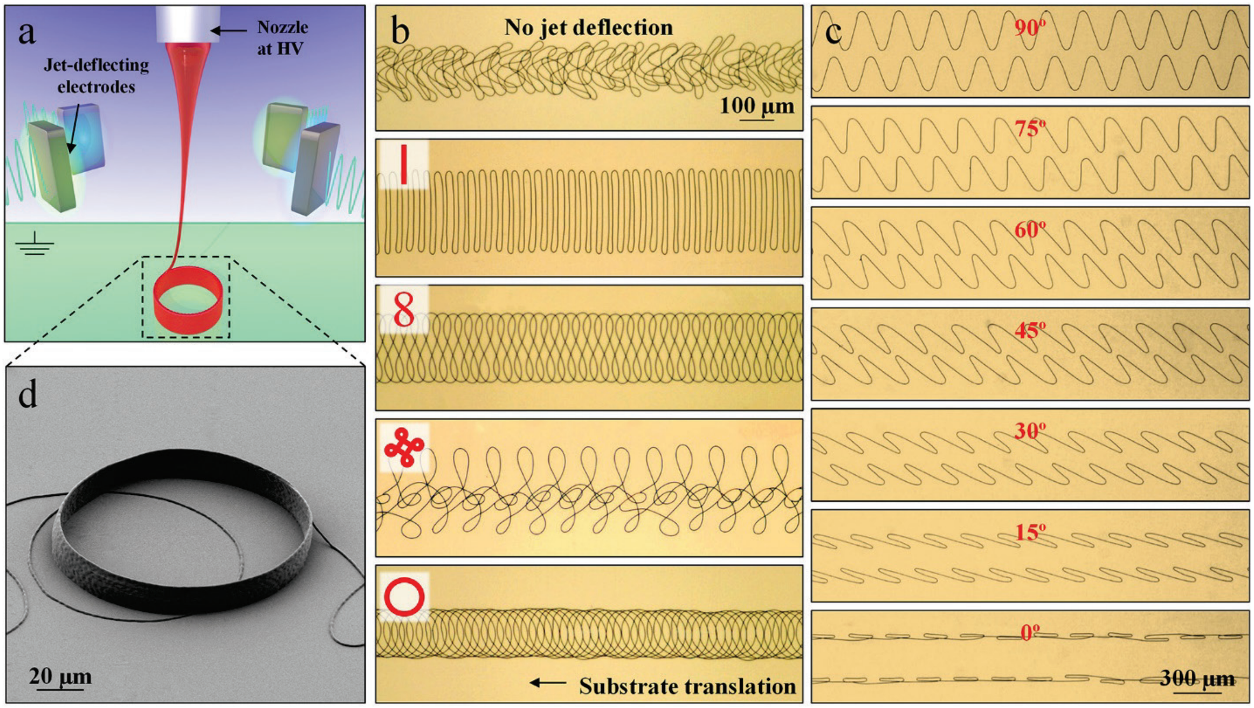

Figure 7.3. Proof of concept for deflecting the MEW jet. a) Schematics of MEW printer with jet-deflection electrodes placed around the nozzle. b) Different pattern geometries printed using jet deflection. Stage translation speed was set at 1 mm·s^{-1}. Red drawing shows the pattern geometry set in the LabView program defining the deflection trajectory. c) Straight fibers printed at different deflection angle (from 90º to 0º). d) 3D structure printed on a motionless collector. Signal amplitude and frequency were set at 4 kV and 25 Hz.

In terms of process stability, EHD jet printing using molten polymers allowed much more stable prints compared to EHD jet printing using solvent-based inks (as shown in Chapters 3 – 6) due to bypassing common instabilities associated with solvent drying. Figure 7.4 illustrates several large-scale prints of fiber tracks (panel "a") or different 3D structures printed on the collector (panel "b") that were stable over 30 minutes.

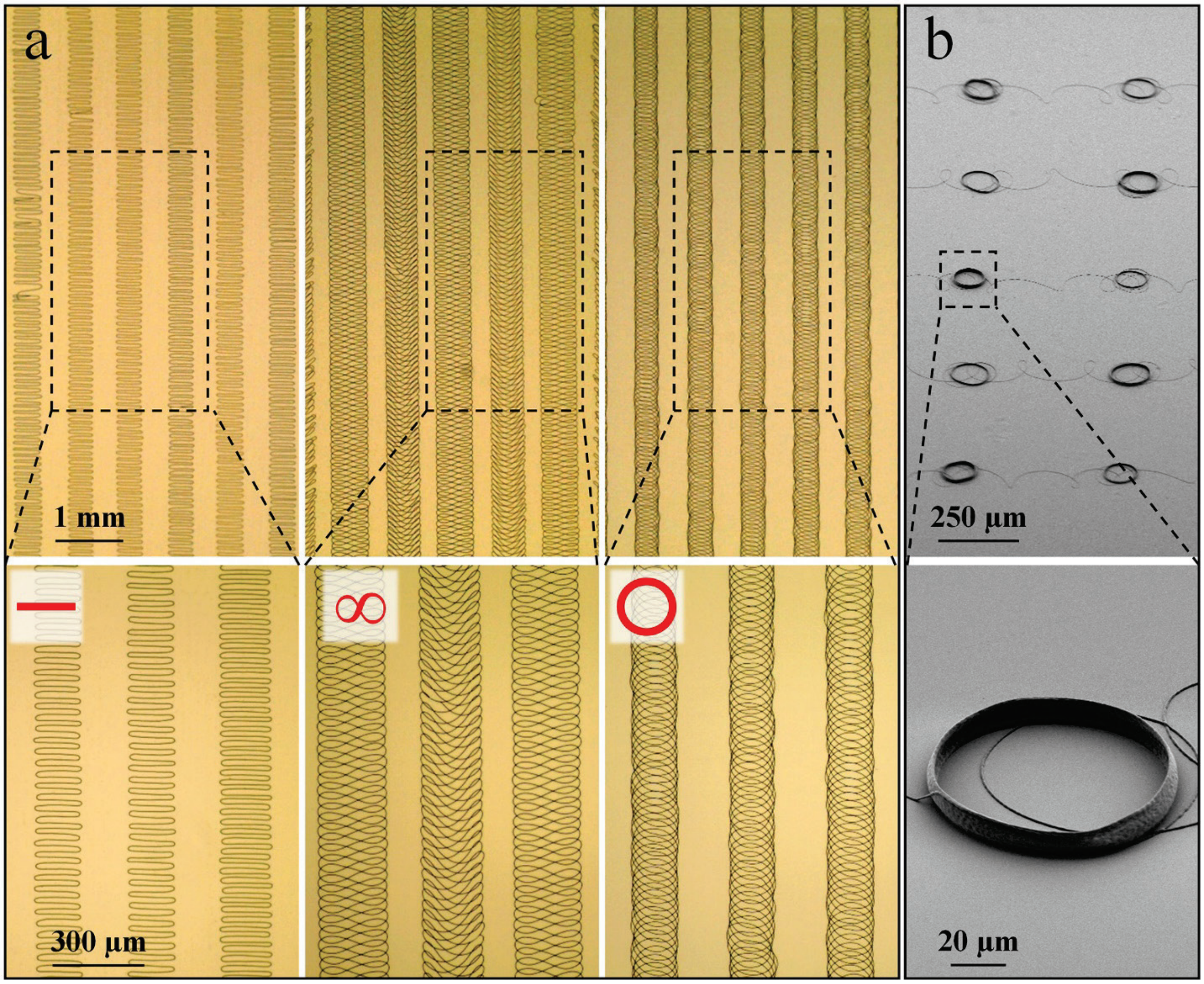

Figure 7.4. Excellent stability of the jet deflection in MEW. Several patterns were deposited on the collector through EHD jet deflection. a) Straight fibers, "infinite" symbol and circles were continuously deflected on the collector while the stage translated at 1 mm·s^{-1}. Jet-deflecting signal amplitude and frequency were set at 4 kV and 50 Hz, respectively. b) 3D structures of different number of layers printed on motionless collector while the jet was deflected at 4 kV and 25 Hz during 0.3 and 0.6 s.

As there were no changes on the jet properties due to solvent evaporation, the MEW jet could keep its speed constant over time, and reproducible fiber tracks were deposited on the collector. However, jet breaking occurred and was automatically initiating after a few seconds with a similar jet speed (Figure 7.5). We hypothesize that the jet breaks occurred due to the insufficient flow of polymer to sustain the jet indefinitely, so the jet was sporadically breaking. It is important to note that the jet initiation is very different for the case of melts and solvent-based inks. For solvent-based inks, the jet must be initiated by either increasing the nozzle voltage and later (after the jet ejection) decreasing it to sustain stable jetting, or by punching the drop surface with a thin rod to break the surface tension[106]. However, in both cases, the drop must be cleaned to get a new drop with fresh surface before the jet initiates. Therefore, in the case of jet interruption for solvent-based systems, the jet does not automatically reinitiate. This practical aspect makes MEW a more robust printing technique over solvent-based jets described in Chapters 3 – 6, as the MEW jet automatically initiates when a constant nozzle voltage is applied, either in the beginning of the print, or soon after the jet-breaking event.

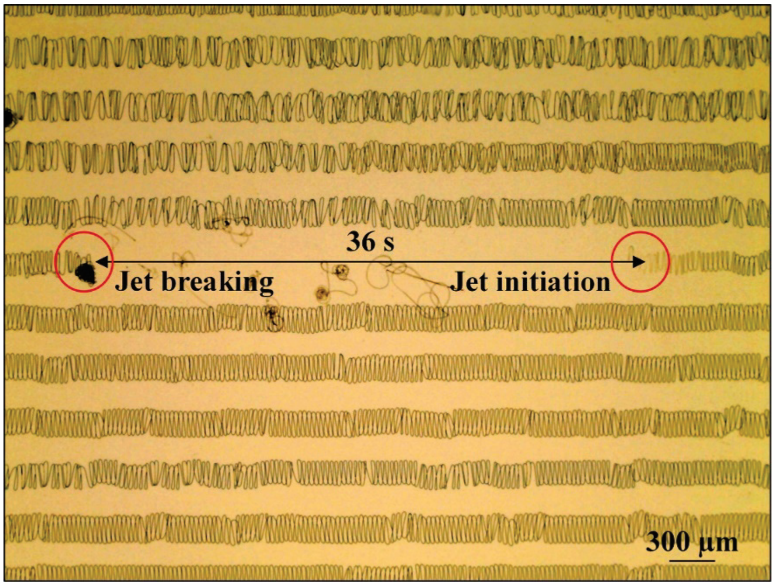

Figure 7.5. Rare interruptions of the jet. The jet was deflected with a sawtooth wave to deposit straight fibers continuously on the collector. Deflection amplitude and frequency were set at 4 KV and 50 Hz, respectively. Unexpected interruptions happened during the printing, but the jet initiated again after a few seconds with similar speed.

Jet deflection printing of micron-scale fibers produced with molten polymers allowed depositing fiber tracks with anisotropic properties on large areas. Figure 7.6a,b illustrates how the printed fibers illuminated in different colors when a spotlight was focused on a small area of the sample, ranging from yellow and green colors to red and blue. This transition on colors was also observed, but at lower intensity, when the entire sample was illuminated (Figure 7.6c). Additionally, rotating the same sample and keeping the light in a fixed position resulted in fibers glowing homogenously with different colors, as Figure 7.6d illustrates, where the printed area glowed from greenish-blue to orange depending on the illumination angle.

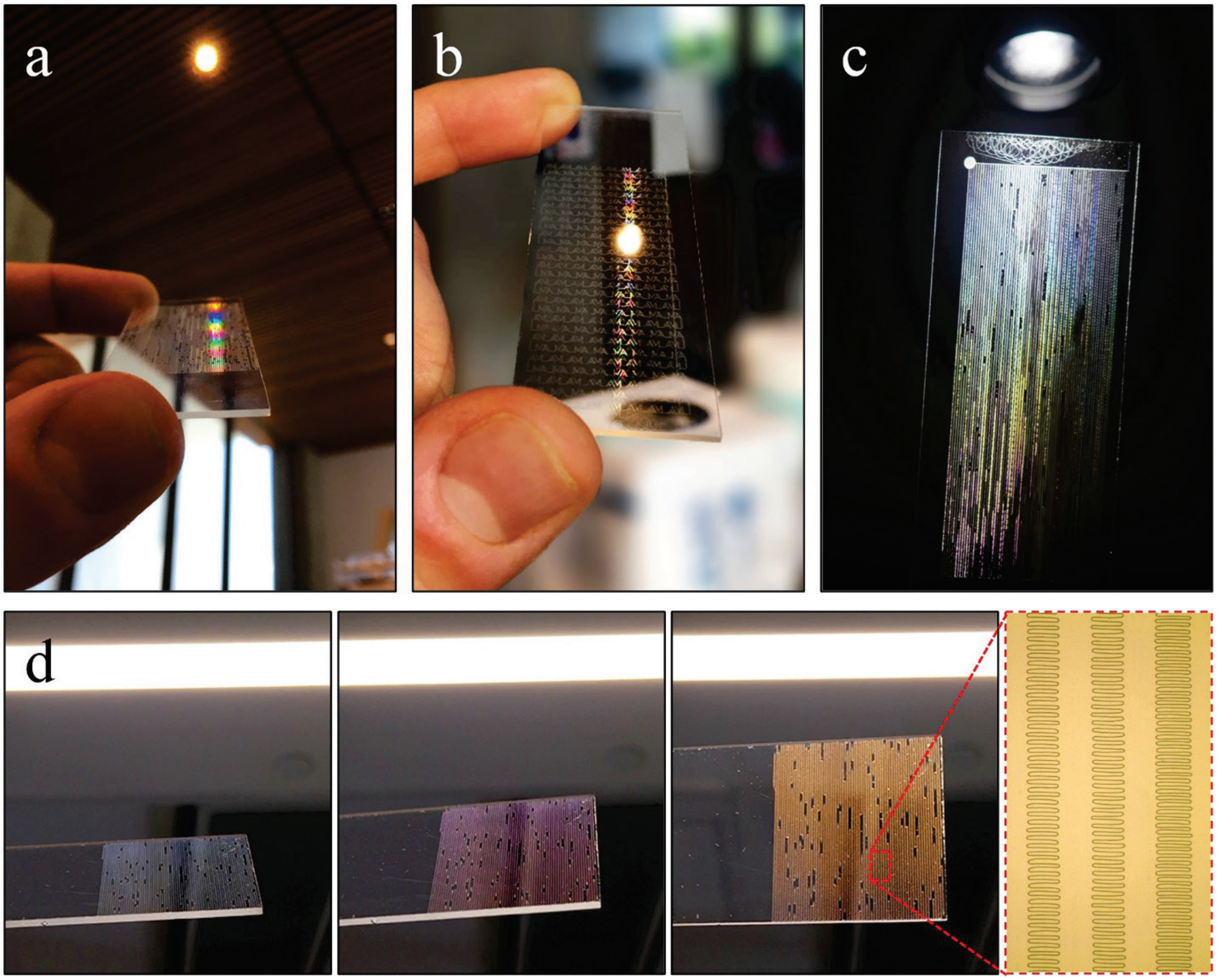

Figure 7.6. Anisotropic properties of the nanofibers result in optical effects. In panels (a,b,c) the fiber track covered 25 mm x 50 mm area on the glass slide, while it covered 25 mm x 25 mm in (d). A concentrated spotlight illuminated a small region of the sample in (a, b), while it illuminated the entire sample in (c). The sample was rotated in (d) to observe the changes in the pattern colors. Optical microscope image in (d) shows the printed fiber track.

7.3. Jet deflection paired with complex stage movements

Combining more complex stage movement with the EHD jet deflection opens exciting possibilities toward many applications. For example, Figure 7.7 illustrates different prints where the stage was moving to reproduce a specific logo path while the jet was deflected. In this figure, Additive Manufacturing Media's (AM) and Wu Tsai Human Performance Alliance's (HPA) logos were printed by two different approaches. For printing AM logo, the stage was moved along the centerline of the letters while the jet was deflected horizontally with a sawtooth wave. This methodology allowed depositing fibers inside the pattern. In another instance, the stage followed the outline of the HPA logo while the jet was deflected to print circles. Therefore, the fiber was deposited on the contour of the logo, leaving empty spaces inside. Additionally, EHD jet deflection printing together with the complex translation of the stage was used to reproduce a small area of the painting called "The Birth of Venus" by Sandro Botticelli. The G-code that defines the stage path was generated by using SquiggleDraw software, which created a rasterized path composed of sine waves with amplitude and frequency dependent on the brightness of the image (Scheme 7.1). As the code is made by sinus waves with different amplitude and frequency, the speed of the stage was not constant during the entire printing since the stage had to decelerate first and accelerate later every time it changed its moving direction, thus the translation speed was lower for the segments with high density of sinusoids. Considering this fact, the stage translation speed was set close to the fiber generation speed (*i.e.*, the jet speed) to get low fiber density when the stage followed straight paths at fast speed (amplitude of sinus waves nearly zero) and give more contrast to the printed sample. While the stage translation speed was much lower than the preset speed (due to frequent deceleration/acceleration events), EHD jet deflection controlled the fiber deposition perpendicular to moving direction.

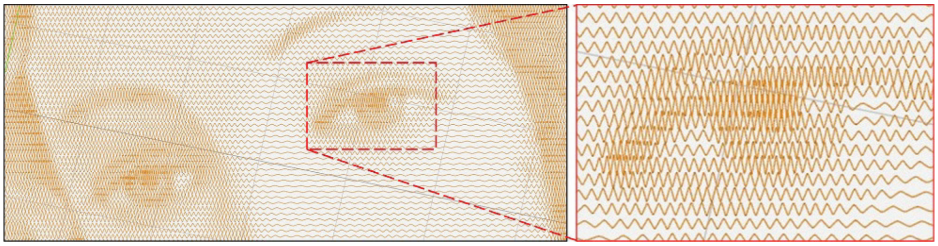

Scheme 7.1. Zoomed part of the designed code to highlight how the contrast is given. Straight and wavy paths are followed by the stage to achieve a desired contrast on the printed drawing.

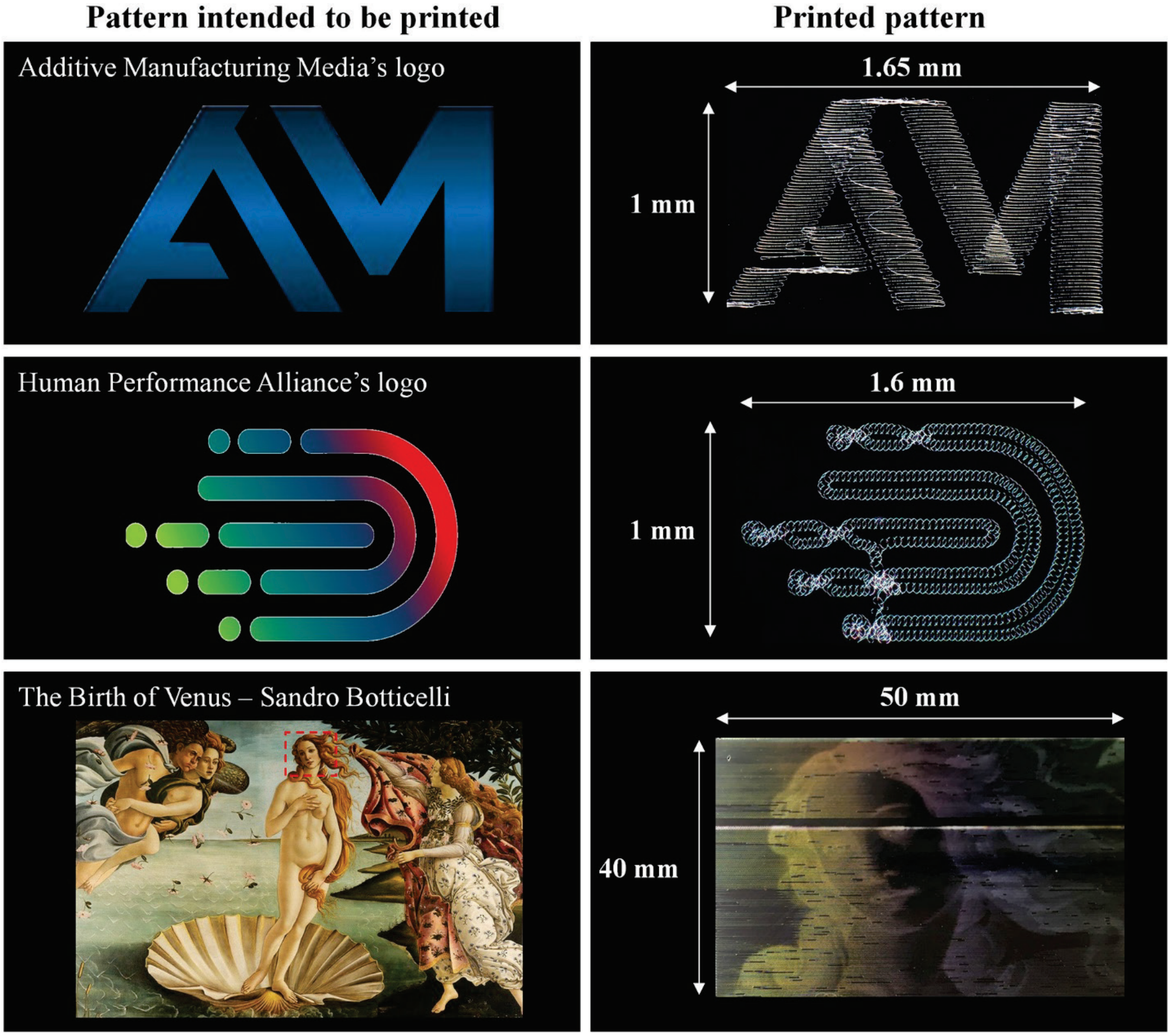
Pattern intended to be printed
Printed pattern
Additive Manufacturing Media's logo
AM
1.65 mm
1 mm
Human Performance Alliance's logo
1.6 mm
1 mm
The Birth of Venus – Sandro Botticelli
50 mm
40 mm

Figure 7.7. Complex patterning of fibers by jet deflection. a) The Additive Manufacturing Media's logo was printed by combining the stage translation, which was following at 1 mm·s^{-1} the letters centerline, while the jet was deflected with a sawtooth wave at signal amplitude 4 kV and 30 Hz. b) The Human Performance Alliance's logo was printed by stage translation following at 1 mm·s^{-1} the logo outline, while the jet was deflected to print circles with a signal amplitude and frequency fixed at 4 kV and 70 Hz respectively. c) Controlled patterning to reproduce the painting "The Birth of Venus" by Sandro Botticelli, combining complex stage translation path and EHD jet deflection. The stage translation speed was set at 10 mm·s^{-1}, but this speed was reached only when the stage moved in straight segments. Meanwhile, the jet was deflected with a signal amplitude and frequency set at 4 kV and 50 Hz, respectively.

General conclusions

Additive manufacturing (AM) by electrohydrodynamic (EHD) jet printing is based on printing thin filaments of polymer as continuous fibers. Owing to the small fiber diameters and high jet speeds achieved by this method using solvent-based inks, high-resolution prints are combined with fast printing speeds. Printing with high fidelity depends critically on controlling the jet arrival speed, and in this thesis, a novel strategy is proposed to determine jet arrival speed based on deflecting the jet electrostatically. Thanks to such deflection, the position of the contact point where the jet deposits onto the substrate is controlled independently from the motion of the substrate, allowing the deposition of complex predefined 2D patterns and 3D objects.

Therefore, EHD jet deflection is presented as a suitable approach to measure and control the jet speed and adjust the jet-deflecting parameters (*i.e.*, signal amplitude and frequency) to match the jet speed with the printing speed easily, avoiding the degradation of the printed geometry that occurs when the jet and printing speed do not match. This methodology opens exciting capabilities for innovative applications that require full control of the positioning of fast nanofibers. Deflecting electrostatically the jet enabled an effective decoupling of the printed track width from the jet speed, stage translation speed and fiber properties (Chapter 3). This fact allows improving colossally the control of the deposition of fiber tracks with precise widths or fiber densities, as those parameters can be adjusted by changing the jet-deflecting signal. In this regard, the same fiber length can be deposited into either wider or narrower tracks (or even submicrometer fiber walls) regardless of the speeds ratio of the jet and collector translation. Jet deflection printing allowed printing fast fibers as tracks with a controlled directionality, either aligned or forming complex motifs, and thus obtaining anisotropic properties of tracks not achievable otherwise. Moreover, jet deflection printing enabled quantifying easily the fiber density just from the optical image of the track, and controlling it as desired from millimeter to submicron scale, giving the possibility to print fiber tracks with heterogeneous fiber density across and along the track.

Regarding the accessibility and the ease of adaptation of the developed technique, it is important to keep in mind that jet deflection can be easily incorporated into existing EHD jet printing setups as an add-on/upgrade allowing extended control. For a successful implementation of this technique, the high voltage amplifier must have a high slew rate to swiftly modulate high voltage signals and ideally provide at least 1000 Hz capability. In terms of voltage, it should be high enough to deflect the jet substantially.

In practice, ± 2 kV is enough when the jet deflection electrodes are positioned at 10 mm from the jet and solvent-based inks are used, while higher voltages (0 – 10 kV) are required when molten polymers are used as ink. So far, the highest cost of entry to practicing jet deflection is the development of the software that generates the control signals. Software is indispensable for printing 2D motifs beyond circles/ellipsoids or 1D deflection. Nevertheless, many of the practical abilities demonstrated in this thesis can be implemented without the need for software development, and only with a single high voltage amplifier/generator for deflecting the jet using a single electrode. In this case, the amplifier/generator must have a basic sinusoidal or sawtooth/triangular wavefunction with controlled amplitude and frequency. The cost of a suitable amplifier/generator can be as low as $1500, making jet deflection very accessible without the need to develop custom-made software. Beyond this capability, more advanced features or the printing of complex motifs and 3D patterns still require more flexible control achievable through software.

However, matching the jet and printing speeds is fundamental to reproduce accurately a predefined design. Too fast and too slow jets result in poor quality patterns, as the collected fiber is too long or too short and thus buckles or cuts corners on its arrival at the collector. To determine the jet speed via EHD jet deflection, a periodic motif was printed either into a 2D pattern, by moving the substrate continuously under the nozzle, or a 3D structure, by keeping the substrate static (Chapter 4). Jet buckling was avoided by using a high enough amplitude and frequency of the jet deflecting signal, and consequently, jet speed could be readily computed from the product of the frequency of the deflection signal and the width of the periodically printed pattern (times a factor that depends on the printed geometry). A similar approach was used to determine jet speed by analyzing the size (width) of 3D structures, such as cylinders or walls, so long as the fiber printing was driven by the jet deflection signal and was not caused by its buckling over the substrate. This method can be practiced either when the jet speed is faster than the stage translation speed or when the jet speed matches with the stage translation speed (by using excess amplitude or frequency in the jet-deflecting signal). Additionally, this methodology was applied to a case study to show the occurrence of jet instabilities during printing, and the feasibility to determine the jet speed in situ using inexpensive optical equipment and automated image recognition software was demonstrated as well. In this regard, this method is far superior to previous methods, for which determining the jet speed involves laborious ex situ high-resolution imaging of individual nanofibers.

The new approach does not require a fast-moving translation stage to attain speeds comparable to the jet speed, as it works robustly with any desired stage speeds (even zero translation speed).

On the other hand, as it is crucial to match the jet speed with the printing speed, it is mandatory to understand how the jet speed depends on the experimental conditions. This thesis shows that the ambient conditions have an important effect on the jet speed, especially the relative humidity (Chapter 5). For this reason, ambient conditions have to be maintained as constant as possible to avoid uncontrolled changes in the jet speed. Then, an optimal ink composition must be found to allow not only depositing dry fibers on the collector, but also preventing the solvent evaporation on the pendant drop when solvent-based inks are used. After ambient conditions are fixed and the ink is selected, processing parameters and setup design have to be adapted to reach the desired jet speed. In Chapter 5 we detailed a few strategies to get faster jet speed using solvent-based inks, such as increasing the ink electrical conductivity, applying higher nozzle voltage, raising the ambient relative humidity and optimizing the ink flow rate. On the other hand, increasing the polymer MW and/or its concentration, moving away the nozzle from the collector, using a wider nozzle outer diameter or rising the ambient temperature produces slower jets. Furthermore, fiber diameters can be mainly varied by tuning the polymer composition or the ink viscosity, and fixing the ambient conditions to promote or minimize the solvent evaporation from the drop.

After having demonstrated different ways to adjust the jet speed to match it with a selected printing speed, we addressed the challenge of EHD jet printing using solvent-based inks of maintaining the jet speed constant over time (Chapter 6). A steady-state printing requires the control and stabilization of several parameters. For example, the drop size should be constant to avoid modifying the electric field that pulls the jet, and the solvent evaporation from the drop must be minimized to avoid the drying of its surface. In addition, the jet ejection point at the drop tip must be stable, and it is dependent not only on the electric field distribution at the drop surface but also on its composition. A highly volatile solvent, which promotes the drying of the drop surface, perturbs the ejection point of the jet, causing the printed pattern to drift. Therefore, the solvent used has to minimize the drop surface drying and avoid instabilities on the jet ejection point. Besides, the jet speed stability strongly depends on the ink viscoelasticity, preventing the interruption of the jet and assuring uniform jet speed when polymers of high MW are used.

Lastly, the research stay in Prof. Paul Dalton's group at the Phil and Penny Knight Campus for Accelerating Scientific Impact (University of Oregon, EEUU) allowed achieving the first results of EHD jet deflection using molten polymers. Different conditions were fixed to get thin and fast fibers using a conventional melt electrowriting setup: low pressures and thin nozzles were used to decrease the flow of molten polymer through the nozzle, and high enough voltages were applied to the nozzle to eject fast jets (while avoiding applying too high voltages that may produce sparks). After operational parameters were optimized to produce thin and fast jets, fibers with diameters around 1 μm were deposited on the collector at 15 – 30 $mm \cdot s^{-1}$. Then, to control the deposition of these fast jets, electrostatic jet deflection was implemented successfully to print not only fiber tracks with variable pattern geometries, but also 3D structures by stacking layer-by-layer on a motionless substrate. Additionally, it was possible to combine electrostatic jet deflection with complex movements of the stage to deposit laborious prints that could not be achieved using conventional MEW setups.

References

1. Zhou, T. Scalable Manufacture of Nanofibers via Near-Field Electrospinning. University of California, **2018**.

2. Zhu, S., Nie, L. Progress in fabrication of one-dimensional catalytic materials by electrospinning technology. *J. Ind. Eng. Chem.* **2021**; 93, 28–56.

3. Morata A., Pacios M., Gadea G., Flox C., Cadavid D., Cabot A., Tarancon A. Large-area and adaptable electrospun silicon-based thermoelectric nanomaterials with high energy conversion efficiencies. *Nat. Commun.* **2018**; 9, 1–8.

4. Zuo Y., Liu Y., Li J., Du R., Han X., Zhang T., Albiol J., Divins N. J., Llorca J., Guijarro N., Sivula K., Cabot A. In Situ Electrochemical Oxidation of Cu_2S into CuO Nanowires as a Durable and Efficient Electrocatalyst for Oxygen Evolution Reaction. *Chem. Mater.* **2019**; 31, 7732–7743.

5. Ahmadi M. H., Ghazvini M., Nazari M. A., Ahmadi M. A., Pourfayaz F., Lorenzini G., Ming T. Renewable energy harvesting with the application of nanotechnology: A review. *Int. J. Energy Res.* **2019**; 43, 1387–1410.

6. Rus, D., Tolley, M. T. Design, fabrication and control of soft robots. *Nature*. **2015**; 521, 467–475.

7. Sears, N. A., Seshadri, D., Dhavalikar, P. S., Cosgriff-Hernandez, E. A Review of 3D Printing in Tissue Engineering. *J. Neurophysiol.* **2007**; 97, 4120–4128.

8. Onses, M. S., Sutanto, E., Ferreira, P. M., Alleyne, A. G., Rogers, J. A. Mechanisms, Capabilities, and Applications of High-Resolution Electrohydrodynamic Jet Printing. *Small* **2015**; 11, 4237–4266.

9. Tan, L. J., Zhu, W., Zhou, K. Recent Progress on Polymer Materials for Additive Manufacturing. *Adv. Funct. Mater.* **2020**; 30, 2003062.

10. ISO/ASTM International. ISO/ASTM 52900: Additive manufacturing - General principles and Terminology. *Int. Stand.* **5**, 1–26 (2015).

11. Scott J., Gupta N., Weber C., Newsome S., Wohlers T., Caffrey T.. Additive Manufacturing: Status and Opportunities. *Addit. Manuf. Status Oppor.* **2012**.

12. Liashenko, I. Ultrafast electrohydrodynamic 3D printing with submicrometer resolution. Universitat Rovira i Virgili, **2020**.

13. Zhang, Z., He, H., Fu, W., Ji, D., Ramakrishna, S. Electro-Hydrodynamic Direct-Writing Technology toward Patterned Ultra-Thin Fibers: Advances, Materials and Applications. *Nano Today*. **2020**; 35, 100942.

14. Hirt, L., Reiser, A., Spolenak, R., Zambelli, T. Additive Manufacturing of Metal Structures at the Micrometer Scale. *Adv. Mater.* **2017**; 29, 1–30.

15. Jiang, Z., Diggle B., Tan Li M., Viktorova J., Bennet C. W., Connal L. Extrusion 3D Printing of Polymeric Materials with Advanced Properties. *Adv. Sci.* **2020**; 7, 1–32.

16. Duty C., Ajunjeru C., Kishore V., Compton B., Hmeidat N., Chen X., Liu P., Hassen A., Lindahl J., Kunc V. What makes a material printable? A viscoelastic model for extrusion-based 3D printing of polymers. *J. Manuf. Process.* **2018**; 35, 526–537.

17. Goh, G. D., Yap Y. L., Tan H. K. J., Sing S. L., Liang G. G., Yeong W. Y. Process–Structure–Properties in Polymer Additive Manufacturing via Material Extrusion: A Review. *Crit. Rev. Solid State Mater. Sci.* **2020**; 45, 113–133.

18. Nurhudan, A. I., Supriadi, S., Whulanza, Y. & Saragih, A. S. Additive manufacturing of metallic based on extrusion process: A review. *J. Manuf. Process.* **2021**; 66, 228–237.

19. Ramazani, H., Kami, A. Metal FDM, a new extrusion-based additive manufacturing technology for manufacturing of metallic parts: a review. *Prog. Addit. Manuf.* **2022**.

20. Nocheseda, C. J. C., Liza, F. P., Collera, A. K. M., Caldona, E. B., Advincula, R. C. 3D printing of metals using biodegradable cellulose hydrogel inks. *Addit. Manuf.* **2021**; 48, 102380.

21. Hergel, J., Hinz, K., Lefebvre, S., Thomaszewski, B. Extrusion-based ceramics printing with strictly-continuous deposition. *ACM Trans. Graph.* **2019**; 38.

22. Kim, H., Renteria A., Islam Md D., Chavez L, Garcia C., Ahsan A., Tseng B, Love N., Lin Y. Fabrication of bulk piezoelectric and dielectric BaTiO 3 ceramics using paste extrusion 3D printing technique. *J. Am. Ceram. Soc.* **2019**; 102, 3685–3694.

23. Renteria, A., Diaz J., He B., Renteria-Marquez I., Chavez L., Regis J., Liu Y., Espalin D., Tseng B., Lin Y. Particle size influence on material properties of BaTiO3 ceramics fabricated using freeze-form extrusion 3D printing. *Mater. Res. Express*. **2019**; 6.

24. Markstedt, K., Håkansson, K., Toriz, G., Gatenholm, P. Materials from trees assembled by 3D printing–Wood tissue beyond nature limits. *Appl. Mater. Today*. **2019**; 15, 280–285.

25. Kariz, M., Sernek, M., Kuzman, M. K. Use of wood powder and adhesive as a mixture for 3D printing. *Eur. J. Wood Wood Prod*. **2016**; 74, 123–126.

26. Xu, W., Wang, X., Sandler, N., Willför, S., Xu, C. Three-Dimensional Printing of Wood-Derived Biopolymers: A Review Focused on Biomedical Applications. *ACS Sustain. Chem. Eng.* **2018**; 6, 5663–5680.

27. Zhang, Y., Tse, C., Rouholamin, D., Smith, P. J. Scaffolds for tissue engineering produced by inkjet printing. *Cent. Eur. J. Eng.* **2012**; 2, 325–335.

28. Mandrycky, C., Wang, Z., Kim, K., Kim, D. H. 3D bioprinting for engineering complex tissues. *Biotechnol. Adv.* **2016**; 34, 422–434.

29. Murphy, S. V., Atala, A. 3D bioprinting of tissues and organs. *Nat. Biotechnol.* **2014**; 32, 773–785.

30. Yang, X. Lu Z., Wu H., Zeng L., Zhao J. Collagen-alginate as bioink for three-dimensional (3D) cell printing based cartilage tissue engineering. *Mater. Sci. Eng. C*. **2018**; 83, 195–201.

31. Mkhize, N. C. High resolution additive manufacturing using electrohydrodynamic jet printing. University of Oxford, **2019**.

32. Liashenko, I., Cabot Codina, A. & Rosell Llompart, J. Device and method for determining the speed of printing of a fiber and the length of a printed fiber. Patent EP3736103A1. **2020**.

33. Liashenko, I., Cabot Codina, A. & Rosell Llompart, J. Printing device and method. Patent EP3736105A1. **2020**.

34. Liashenko, I., Rosell-Llompart, J. & Cabot, A. Ultrafast 3D printing with submicrometer features using electrostatic jet deflection. *Nat. Commun.* **2020**; 11.

35. Zhao, K., Wang D., Li K., Jiang C., Wei Y., Qian J., Feng L., Du Z., Xu Z., Liang J. Drop-on-Demand Electrohydrodynamic Jet Printing of Graphene and Its Composite Microelectrode for High Performance Electrochemical Sensing. *J. Electrochem. Soc.* **2020**; 167, 107508.

36. Zhang, B., Lee Z., Kim M., Lee N., Lee H., Byun D. Direct patterning and spontaneous self-assembly of graphene oxide via electrohydrodynamic jet printing for energy storage and sensing. *Micromachines*. **2020**; 11.

37. Guo, W., Hu, J., Yan, X. Influence of process parameters on the characteristics of electrohydrodynamic-printed UV-curing conductive lines on the fabric. *J. Micromechanics Microengineering*. **2020**; 32.

38. Guo, W., Hu, J., Yan, X. Effect of the solvent evaporation rate of silver ink on the electrohydrodynamic-printing formability of textile-based printing electronics. *Text. Res. J.* **2022**; 92, 886–896.

39. Kim, H. S., Parl K. H., Kim J. H., Jung H. I. Optimization of electrohydrodynamic writing technique to print collagen. *Exp. Tech.* **2007**; 31, 15–19.

40. Oh, H., Kim, M. K., Lee, K. H. Preparation of sericin microparticles by electrohydrodynamic spraying and their application in drug delivery. *Macromol. Res.* **2011**; 19, 266–272.

41. Gasperini, L., Maniglio, D., Motta, A., Migliaresi, C. An Electrohydrodynamic Bioprinter for Alginate Hydrogels Containing Living Cells. *Tissue Eng. Part C Methods*. **2015**; 21, 123–132.

42. Wei, C., Dong, J. Direct fabrication of high-resolution three-dimensional polymeric scaffolds using electrohydrodynamic hot jet plotting. *J. Micromechanics Microengineering*. **2013**; 23.

43. Zhao, K., Wang D., Wang Z., Jiang C., Abbas Z., Zheng Y., Yand Q., Tang B., Liu T., Tao F., Xu W., Liang J. Fabrication of piezoelectric thick-film stator using electrohydrodynamic jet printing for micro rotary ultrasonic motors. *Ceram. Int.* **2020**; 46, 26129–26135.

44. Luo, J., Zhang, L., Wu, T., Song, H., Tang, C. Flexible piezoelectric pressure sensor with high sensitivity for electronic skin using near-field electrohydrodynamic direct-writing method. *Extrem. Mech. Lett.* **2021**; 48, 101279.

45. Baker, B. M., O Gee A., Metter R. B., Natahn A. S., Marklein R. A., Burdick J. A., Mauck R. L. The potential to improve cell infiltration in composite fiber-aligned electrospun scaffolds by the selective removal of sacrificial fibers. *Biomaterials*. **2008**; 29, 2348–2358.

46. Yin, Z., Chen X., Chen J. L., Shen W. L., Nguyen T. M. H., Gao L., Ouyang H. W. The regulation of tendon stem cell differentiation by the alignment of nanofibers. *Biomaterials*. **2020**; 31, 2163–2175.

47. George, D., Garcia A., Pham Q., Perez M. R., Deng J., Nguyen M. T., Zhou T., Martinez-Chapa S. O., Won Y., Liu C., Lo R. C., Ragan R., Madou M. Fabrication of patterned graphitized carbon wires using low voltage near-field electrospinning, pyrolysis, electrodeposition, and chemical vapor deposition. *Microsystems Nanoeng*. **2020**; 6, 7.

48. Middleton, R., Li X., Shepherd J. H., Li Z., Wang W., Best S. M., Cameron R. E., Huang Y. Y. S. Near-Field Electrospinning Patterning Polycaprolactone and Polycaprolactone/Collagen Interconnected Fiber Membrane. *Macromol. Mater. Eng.* **2018**; 303, 1–6.

49. Bružauskaitė, I., Bironaitė, D., Bagdonas, E., Bernotienė, E. Scaffolds and cells for tissue regeneration: different scaffold pore sizes—different cell effects. *Cytotechnology* **2016**; 68, 355–369.

50. Ray, S. S., Chen, S. S., Nguyen, N. C., Nguyen, H. T. Electrospinning: A Versatile Fabrication Technique for Nanofibrous Membranes for Use in Desalination. *Nanoscale Materials in Water Purification* (Elsevier Inc., **2018**).

51. Nazemi, M. M., Khodabandeh, A., Hadjizadeh, A. Near-Field Electrospinning: Crucial Parameters, Challenges, and Applications. *ACS Appl. Bio Mater.* **2022**; 5, 394–412.

52. Wasim, M., Sabir, A., Shafiq, M. & Jamil, T. Electrospinning: A Fiber Fabrication Technique for Water Purification. *Nanoscale Materials in Water Purification* (Elsevier Inc., **2018**).

53. Asmatulu, R., Khan, W. S. Historical background of the electrospinning process. *Synth. Appl. Electrospun Nanofibers*. **2019**; 17–39.

54. Murthe, S. S., Mohamed Saheed, M. S., Perumal, V., Mohamed Saheed, M. S., Mohamed, N. M. Electrospun nanofibers for biosensing applications. *Nanobiosensors for Biomolecular Targeting* (Elsevier Inc., **2018**).

55. Zheng, J., Ze L. Y., Bin S., Hua Z. Z., Feng S., Di Z. H., Ming Z. Z., Yin H. J. Polymer nanofibers prepared by low-voltage near-field electrospinning. *Chinese Phys. B*. **2012**; 21, 1–6.

56. He, L. Control and Predictability of Near-Field Electrospinning. (University of California, **2017**).

57. Pan, Y., Zeng, L. Simulation and validation of droplet generation process for revealing three design constraints in electrohydrodynamic jet printing. *Micromachines*. **2019**; 10.

58. Flores-Hernandez, D. R., Cardenas-Benitez, B., Martinez-Chapa, S. O., Bonilla-Rios, J. Tailoring the diameters of electro-mechanically spun fibers by controlling their Deborah numbers. *Polymers (Basel).* **2020**; 12.

59. Davis, Z. G., Hussain, A. F., Fisher, M. B. Processing variables of direct-write, near-field electrospinning impact size and morphology of gelatin fibers. *Biomed. Mater.* **2021**; 16.

60. Ghorani, B., Goswami, P., Russell, S. Parametric Study of Electrospun Cellulose Acetate in Relation to Fibre Diameter. *Res. J. Text. Appar.* **2015**; 19, 24–40.

61. Theron, S. A., Zussman, E., Yarin, A. L. Experimental investigation of the governing parameters in the electrospinning of polymer solutions. *Polymer.* **2004**; 45, 2017–2030.

62. Tan, S. H., Inai, R., Kotaki, M., Ramakrishna, S. Systematic parameter study for ultra-fine fiber fabrication via electrospinning process. *Polymer.* **2005**; 46, 6128–6134.

63. Herrera, A. B. Melt electrospinning of polymers: additives, nanocomposites and blendings. (Instituto Politecnico do Porto, **2020**).

64. Eleonore C. L. B., Deanna N., Dalton P. D., Dargaville T. R. Production of Scaffolds Using Melt Electrospinning Writing and Cell Seeding. *Methods Mol Biol*. **2021**; 147, 111–124.

65. Dalton, P. D., Woodfield, T. B. F., Mironov, V., Groll, J. Advances in Hybrid Fabrication toward Hierarchical Tissue Constructs. *Adv. Sci.* **2020**; 7.

66. Shabanizarinkafshrashti, E. Free Surface Melt Electrospinning: A Solvent Free Approach Toward Electrospinning. (North Carolina State University, **2020**).

67. Youssef, A., Hollister, S. J., Dalton, P. D. Additive manufacturing of polymer melts for implantable medical devices and scaffolds. *Biofabrication*. **2017**; 9.

68. Muerza-Cascante, M. L., Haylock, D., Hutmacher, D. W., Dalton, P. D. Melt electrospinning and its technologization in tissue engineering. *Tissue Eng. - Part B Rev.* **2015**; 21, 187–202.

69. Robinson, T. M., Hutmacher, D. W., Dalton, P. D. The Next Frontier in Melt Electrospinning: Taming the Jet. *Adv. Funct. Mater.* **2019**; 29.

70. Han, H., Ko, J. Hydrophobic surface fabricated by electrospinning for advanced piezoelectric sensor. *J. Adv. Mar. Eng. Technol.* **2020**; 44, 150–155.

71. Zhang, K., Zhao, W., Liu, Q., Yu, M. A new magnetic melt spinning device for patterned nanofiber. *Sci. Rep.* **2021**; 11, 8895.

72. Liashenko, I., Hrynevich, A., Dalton, P. D. Designing Outside the Box: Unlocking the Geometric Freedom of Melt Electrowriting using Microscale Layer Shifting. *Adv. Mater.* **2020**; 32.

73. Buivydiene, D., Krugly E., Ciuzas D., Tichonovas M., Kliucininkas L., Martuzevicius D. Formation and characterisation of air filter material printed by melt electrospinning. *J. Aerosol Sci.* **2019**; 131, 48–63.

74. Chen, Q., Liu Y., Deng H., Lyu T., Tan J., Yang W., Li H., Ramakrishna S. Melt differential electrospinning of polyphenylene sulfide nanofibers for flue gas filtration. *Polym. Eng. Sci.* **2020**; 60, 2887–2894.

75. Su, Y., Qiu T., Song W., Han X., Sun M., Wang Z., Xie H., Dong M., Chen M. Melt Electrospinning Writing of Magnetic Microrobots. *Adv. Sci.* **2021**; 8, 1–7.

76. Naveau, A., Smirani R., Remy M., Pomar P., Destruhaut F. Cybergology and bioprinting : The biotechnological future of maxillofacial rehabilitation. **2019**.

77. D Dong, Y., Sun, J. Melt-based Electrohydrodynamic Bioprinting: Heating Unit, Ambient Control, and Power Module Control. **2021**. In The Fifth International Conference on Biological Information and Biomedical Engineering (BIBE2021).

78. Eichholz, K. F., Hoey, D. A. Melt electrowritten scaffolds with bone-inspired fibrous and mineral architectures to enhance BMP2 delivery and human MSC osteogenesis. bioRxiv. **2019**; 1–28.

79. Formisano, N., Van der Putten C., Grant R., Sahin G., Truckenmuller R. K., Bouten C. V. C., Kurniawan N. A., Giselbrecht S. Mechanical Properties of Bioengineered Corneal Stroma. *Adv. Healthc. Mater.* **2021**; 10, 1–19.

80. Hammerl, A., Diaz Cano, C. E., De-Juan-Pardo, E. M., van Griensven, M., Poh, P. S. P. A Growth Factor-Free Co-Culture System of Osteoblasts and Peripheral Blood Mononuclear Cells for the Evaluation of the Osteogenesis Potential of Melt-Electrowritten Polycaprolactone Scaffolds. *Int. J. Mol. Sci.* **2019**; 20.

81. Dalton, P. D., Grafahrend, D., Klinkhammer, K., Klee, D., Möller, M. Electrospinning of polymer melts: Phenomenological observations. *Polymer.* **2007**; 48, 6823–6833.

82. Bastús, N. G., Merkoçi, F., Piella, J., Puntes, V. Synthesis of highly monodisperse citrate-stabilized silver nanoparticles of up to 200 nm: Kinetic control and catalytic properties. *Chem. Mater.* **2014**; 26, 2836–2846.

83. Bisht, G. S., Canton G., Mirsepassi A., Kulinsky L., Oh S., Rankin D. D., Madou M. J. Controlled continuous patterning of polymeric nanofibers on three-dimensional substrates using low-voltage near-field electrospinning. *Nano Lett.* **2011**; 11, 1831–1837.

84. Bodnár, E., Grifoll, J., Rosell-Llompart, J. Polymer solution electrospraying: A tool for engineering particles and films with controlled morphology. *J. Aerosol Sci.* **2018**; 125, 93–118.

85. Shenoy, S. L., Bates, W. D., Frisch, H. L., Wnek, G. E. Role of chain entanglements on fiber formation during electrospinning of polymer solutions: Good solvent, non-specific polymer-polymer interaction limit. *Polymer.* **2005**; 46, 3372–3384.

86. McKee, M. G., Wilkes, G. L., Colby, R. H., Long, T. E. Correlations of Solution Rheology with Electrospun Fiber Formation of Linear and Branched Polyesters. *Macromolecules* **2004**; 37, 1760–1767.

87. Palangetic, L., Reddy N. K., Srinivasan S., Cohen R. E., McKinley G. H., Clasen C. Dispersity and spinnability: Why highly polydisperse polymer solutions are desirable for electrospinning. *Polymer.* **2014**; 55, 4920–4931.

88. Galliker, P., Schneider J., Eghlidi H., Kress S., Sandoghdar V., Poulikakos D. Direct printing of nanostructures by electrostatic autofocussing of ink nanodroplets. *Nat. Commun.* **2012**; 3.

89. Moon, S., Jones M. S., Seu E., Lee J., Lahann L., Jordahl J. H., Lee J., Lahann J. 3D jet writing of mechanically actuated tandem scaffolds. *Sci. Adv.* **2021**; 7, 1–9.

90. Ebagninin, K. W., Benchabane, A., Bekkour, K. Rheological characterization of poly(ethylene oxide) solutions of different molecular weights. *J. Colloid Interface Sci.* **2009**; 336, 360–367.

91. JJackson, S., Dickens, T. Rheological and structural characterization of 3D-printable polymer electrolyte inks. *Polym. Test.* **2021**; 104, 107377.

92. Tam, K. C., Wu, X. Y., Pelton, R. H. Poly(N-isopropylacrylamide). II. Effect of polymer concentration, temperature, and surfactant on the viscosity of aqueous solutions. *J. Polym. Sci. Part A Polym. Chem.* **1993**; 31, 963–969.

93. Singh, S. K., Subramanian, A. Phase-field simulations of electrohydrodynamic jetting for printing nano-to-microscopic constructs. *RSC Adv.* **2020**; 10, 25022–25028.

94. Mkhize, N., Bhaskaran, H. Electrohydrodynamic Jet Printing: Introductory Concepts and Considerations. *Small Sci.* **2022**; 2, 2100073.

95. Li F., Yin X. Y., Yin X. Z. Axisymmetric and non-axisymmetric instability of an electrically charged viscoelastic liquid jet. *J. Nonnewton. Fluid Mech.* **2011**; 166, 1024–1032.

96. Li L. H., Lai W. H. Energy form of cone-jets in electrohydrodynamic atomization. *Int. J. Turbo Jet Engines* **2011**; 28, 199–207.

97. Yalcinkaya, F., Yalcinkaya, B., Jirsak, O. Influence of salts on electrospinning of aqueous and nonaqueous polymer solutions. *J. Nanomater.* **2015**; 2015.

98. Lauricella, M., Succi, S., Zussman, E., Pisignano, D., Yarin, A. L. Models of polymer solutions in electrified jets and solution blowing. *Rev. Mod. Phys.* **2020**; 92.

99. Bradley, R. S., Fuchs, N. A. *Evaporation and Droplet Growth in Gaseous Media*. (Pergamon, **1959**).

100. Shin, D., Choi, S., Kim, J., Regmi, A., Chang, J. Direct-Printing of Functional Nanofibers on 3D Surfaces Using Self-Aligning Nanojet in Near-Field Electrospinning. *Adv. Mater. Technol.* **2020**; 5, 1–8.

101. Choi, S., Shin, D., Chang, J. Nanoscale Fiber Deposition via Surface Charge Migration at Air-to-Polymer Liquid Interface in Near-Field Electrospinning. *ACS Appl. Polym. Mater.* **2020**; 2, 2761–2768.

102. Xu, L., Wang, X., Huang, Y., Zheng, G., Sun, D. Stresses dominate pulsated electrohydrodynamic spraying modes in near field. *Nano/Micro Eng. Mol. Syst.* **2021**; 732–735.

103. Rosell-Llompart, J., Grifoll, J., Loscertales, I. G. Electrosprays in the cone-jet mode: From Taylor cone formation to spray development. *J. Aerosol Sci.* **2018**.

104. Lee, A., Jin, H., Dang, H. W., Choi, K. H., Ahn, K. H. Optimization of experimental parameters to determine the jetting regimes in electrohydrodynamic printing. *Langmuir.* **2013**; 29, 13630–13639.

105. Hrynevich, A., Liashenko, I., Dalton, P. D. Accurate Prediction of Melt Electrowritten Laydown Patterns from Simple Geometrical Considerations. *Adv. Mater. Technol.* **2020**; 5.

106. Cisquella-Serra, A., Magnani M., Gual-Mosegui A., Holmberg S., Madou M., Gamero-Castaño M. Study of the electrostatic jet initiation in near-field electrospinning. *J. Colloid Interface Sci.* **2019**; 543, 106–113.

Future work and outlook

Electrohydrodynamic (EHD) jet printing with the implementation of electrostatic jet deflection has been proven as a suitable methodology to match the jet speed with the printing speed easily, allowing the deposition of fiber tracks and 3D objects with the best possible quality. However, EHD jet printing is still in the early stages on its way to become an established microfabrication technique, and much has to be done concerning the stability of the printing over time and the use of new materials. In this thesis, the effect of some parameters on the jet speed and its stability using solvent-based inks was analyzed to understand how it could be improved, but several challenges still have to be overcome. Additionally, we mainly based all of our studies in only one polymer, polyethylene oxide, as it is a well-known polymer used in EHD jet printing, so we do not have any feedback regarding the use of different polymers and its stability. Considering all the aforementioned, particular future goals can be defined as:

- **Improving the control of the stability during printing**

Ambient conditions strongly affect the ink properties and consequently the jet dynamics, and this is the reason why they have to be controlled to avoid undesired and unreproducible prints. Before starting the experiments, the drop is typically cleaned to get a fresh drop surface at the beginning of the printing. After that, the solvent evaporation has to be minimized, and several strategies can be performed to achieve this goal. For example, the incorporation of a coflow around the nozzle will help to prevent the drying of the drop surface, but its composition should be optimized to avoid printing wet fibers on the collector. Alternatively, using a frame with walls to enclose the printer and protect the jet from changes in the ambient conditions can be another approach. Furthermore, this chamber would open a possibility to control the relative humidity and temperature while printing.

- **Printing with different polymers**

Depending on the polymer type and ink composition (*i.e.*, if the ink contains added salts or NPs), the printed fiber would have specific properties that would be used for particular applications. However, it is challenging to define new inks that allow ejecting stable jets. The ink properties are critical to allow ejecting thin filaments of polymer towards the collector. The type of polymer and solvent defines the properties of the ink, and changing either the polymer, the solvent or their composition will strongly affect the printing process.

Generally, the ink has to be viscoelastic enough to allow stretching the jet without interruptions. If dissolving a particular polymer in a solvent does not allow ejecting a stable jet, the ink can be complemented with another polymer in small concentrations, such as polyethylene oxide, to provide the ink suitable properties for printing. Additionally, post-processing steps (such as polymer cross-linking or carbonation) can be carried out to improve the mechanical properties of the fibers in relation to the field of use.

- **Searching for applications**

This thesis is mainly focused in analyzing the jet speed to study the stability of the EHD jet printing, and some applications to show the performance and the advantages of this printing technology versus the other printing approaches are missing. Therefore, it would be interesting to demonstrate the use of electrostatic jet deflection for the production of electronic devices at small sizes, or the patterning of polymeric fibers with nanoparticles (NPs) on the surface of scaffolds for some functionalities, such as enhancing the cell attachment in tissue engineering.

- **Analyzing how the printed fibers can illuminate in different colors**

As a possible optical application, this thesis illustrates that printed fibers, with submicron diameters, illuminated in different colors when a fixed light shined the sample. These differences in the illumination colors may be due to differences on the fiber diameter or density, but more studies should be carried out to confirm that the fiber diameter and density affect the colors at which the fibers illuminate. If this is the reason, electrostatic jet deflection will allow reproducing a desired color easily. Additionally, it was possible to observe that sometimes colors were very bright and vivid, and this fact suggests that there must be an optimal set of experimental conditions that enhances the fiber brightness under a spotlight.

Alberto Ramón

Personal information

January 8, 1992
Spain
Spanish

Contact information

☎ +34 692818987
bertoramf@gmail.com
www.linkedin.com/in/aramonferrer

Education

Jul. 2018 – Present	**PhD in 3D printing at submicrometer scale, at Institut de Recerca en Energía de Catalunya**	**Barcelona, Spain**
Sep. 2014 – Feb. 2016	**Master's Degree in Chemical Engineering, at Universidad Complutense de Madrid**	**Madrid, Spain**
Sep.2010 – Jun. 2014	**Bachelor's Degree in Chemical Engineering, at Universitat Autònoma de Barcelona** (Top 10% of the class, with 3 excellents)	**Barcelona, Spain**

Professional experience

07/18–Present. **Institut de Recerca en Energía de Catalunya** — **Barcelona, Spain**

Researcher PhD Student

· Improving the efficiency and reproducibility of an additive manufacturing technique based on electrohydrodynamic phenomena.
· Study of the effect of its operational parameters.
· Improving the functionality of the existing inks with nanoparticles.

03/22–08/22 **University of Oregon** — **Oregon, United States**

Visitor PhD Student

· Assembly of a Fused Deposition Modeling (FDM) printer from scratch.
· Optimization of the working conditions in Melt Electrowriting (MEW) printers to get thin and fast fibers.
· Implementation of the know-how achieved during the PhD to expand the capabilities of conventional MEW printing.

07/16–12/17 **Universidad Complutense de Madrid** — **Madrid, Spain**

Contract Researcher

· Study and optimization of the succinic acid production from xylose, using biocatalysts.
· Determination of the experimental process for carrying out that production, dealing with different stages (pre-inoculum, inoculum and bio-reactor).
· Implementation of analytical methods for reactants, products and biomass measurements.
· Consideration of several strategies to accomplishing succinic acid production: using sealed bottles, bio-reactor or *resting cells* conditions.

03/14–06/14 **Lubrizol Advanced Materials** — **Barcelona, Spain**

Student Intern

· Filling out *Risk Assessment* files for new reactants.
· Verifying and updating of the Piping and Instrumentation Diagrams (P&ID).
· Modification of "Working Instructions" for manufacturing products.
· Collaboration in the development of screens for functional specifications in the Digital Control System.

Languages

Spanish ●●●●
Catalan ●●●●
English ●●●○

IT skills

Advanced knowledges in:
· **Simulators:** *Aspen Hysys, Simulink, FlexPDE.*
· **Programmers:** *Matlab, Polymath.*
· **Graphic design:** *AutoCAD, POV-Ray, Photoshop, Fusion 360.*
· **Others:** Origin, EndNote, OpenProject.

Additional information

2018-2021	· Participation in several workshops/congresses related to electrohydrodynamic phenomena and 3D printing.
10/2017	· 10th World Congress of Chemical Engineering attendance, in Barcelona.
11/2016	· Safety course on the use of cryogenic gas and liquid cylinders, given by **Praxair**.
07/2016	· Acquisition of English B2 certificate, provided by the School of Modern Languages at **Universitat Oberta de Catalunya**.
09/2015	· Finalization of my master thesis (UCM-910134 FQPIMA research group), regarding the isobutanol production using genetically modified organisms.
03/2015	· XII Introductory Course in the Matter Structure, given by Consejo Superior de Investigaciones Científicas (**CSIC**).
06/2011	· Driving license obtaining.